The Dissertation Committee for Shao-Chien Lee
certifies that this is the approved version of the following dissertation:

Applications of Photolithographic Techniques: Materials Modeling for Double-Exposure Lithography and Development of Shape-Encoded Biosensor Arrays

Committee:

C. Grant Willson, Supervisor

Roger T. Bonnecaze

Benny D. Freeman

Jennifer A. Maynard

Paul A. Zimmerman

Applications of Photolithographic Techniques: Materials Modeling for Double-Exposure Lithography and Development of Shape-Encoded Biosensor Arrays

by

Shao-Chien Lee, B.S.

DISSERTATION

Presented to the Faculty of the Graduate School of
The University of Texas at Austin
in Partial Fulfillment
of the Requirements
for the Degree of

DOCTOR OF PHILOSOPHY

THE UNIVERSITY OF TEXAS AT AUSTIN
August 2009

To my loving wife and family.

Acknowledgments

The dissertation presented herein would not have been possible without the help and opportunities afforded to me by many generous people. First and foremost I would like to thank my family to whom this work is dedicated. I would like to thank my loving and patient wife, Melody, who has been my constant encouragement in all of my life's pursuits. My dear wife, soon you can have "whatever you like" – well, within limits. I would also like to thank my parents, to whom words cannot express my gratefulness for the sacrifices they have made in the hopes of a better life for me. My surrogate American/Norwegian parents, Ralph and Marianne Gjerde, provided critical guidance during my teenage years and helped to shape my Faith. My brother, Hsiau-Wei Lee, who not only made my life entertaining in the way only a sibling can, but also watched over me in college. Thanks to my great in-laws, the Lius, who have offered support and understanding to the familial upstart.

This work also would not have been possible without the support of friends and colleagues. Special thanks to the members, both former and present, of the Willson Research Group. I especially want to thank Michael Lin, Kane Jen, and Elizabeth Costner; it was a true privilege to have started – the Willson Research Group Engineering Class '04 – and shared the adventure that is graduate school with you. Particular thanks also go to Frank Palmieri

and Siddharth Chauhan, from whom I have learned much about global diversity. A special thank you goes to Kathleen Sparks. She has always been willing to help poor, lost graduate students and has, on many occasions, watched out for me.

Many thanks go to those who have preceded me on the MUFFINS project. The non-exhaustive list includes Benjamen Rathsack, David Johnson, Matthew Schmid, Jason Meiring, Michael Dickey, Peter Carmichael, Scott Grayson, Jason Bates, Romy Kirby, and Kalpana Manthiram. Their hard work established the foundation upon which the MUFFINS work described herein is built. Special thanks also go to all of the collaborators on the double-exposure materials development project. To the team at UT – Adam Berro, Younjin Cho, Xinyu Gu, Tomoki Nishimura, and Toshiyuki Ogata – thank you very much for teaching "real world" chemistry to a number cruncher. The advances in this project also would not have been possible without Professor Turro's group at Columbia University, colleagues at SEMATECH, colleagues at Intel, and many others.

Thanks to Stephen Abboud, Obiora Ofoegbu, and Essence Yung who endured working alongside me as undergraduate assistants and made my life far easier. I would like to acknowledge the exceptional work of Jim Smitherman, Butch Cunningham, and Mike Ronalter, Randy Rife, Kevin Haynes, Alisha Hall, Eddie Ibarra, Kay Costales-Swift, and T Stockman. Thank you to Jennifer Pai and the Maynard Group for their help with mission-critical buffer solutions. Special thanks go to Mark Smith and Trey Graves of KLA-Tencor

who offered key technical insights that enabled the custom 2X simulator. I would like to thank Chris Mack for constructive discussions regarding the 2X work as well.

I am indebted to the generous donors of the Engineering Doctoral Fellowship for their financial support. The double-exposure simulation work was made possible by the generous donation of PROLITH and ProDATA software licenses from KLA-Tencor and workstations from the Intel Corporation and funding from SEMATECH. I would like to acknowledge the Center for Nano and Molecular Science and Technology at the University of Texas at Austin and the UT Microarray Core Facility for the use of their instruments.

I am very grateful to my committee members, Roger Bonnecaze, Benny Freeman, Jennifer Maynard, Jeff Byers, and Paul Zimmerman, for their guidance and careful consideration of my graduate repertoire. Finally, my highest gratitude goes to my advisor Professor Grant Willson, who five years ago took the time to reach out to a clueless kid – one who did not know how lucky he was. With Professor Willson, I had the opportunity to learn very much about science and lithography, but more importantly, about life and how to be a better person in this world. He truly cares for his students, and none of this work would have been possible without his guidance.

Applications of Photolithographic Techniques: Materials Modeling for Double-Exposure Lithography and Development of Shape-Encoded Biosensor Arrays

Publication No. __________________

Shao-Chien Lee, Ph.D.
The University of Texas at Austin, 2009

Supervisor: C. Grant Willson

Double-exposure lithography has shown promise as potential resolution enhancement technique that is attractive because it is much cheaper than double-patterning lithography and it can be deployed on existing imaging tools. However, this technology is not possible without the development of new materials with nonlinear response to exposure dose. Several materials have been proposed to implement a nonlinear response to exposure including reversible contrast enhancement layers (rCELs), two-photon materials, intermediate state two-photon (ISTP) materials, and optical threshold layers (OTLs). The performance of these materials in double-exposure applications was investigated through computer simulation using a custom simulator. The results from the feasibility studies revealed that the ISTP and OTL types of materials showed much more promise than the rCEL and two-photon types of materials. Calculations show that two-photon materials will not be feasible unless

achievable laser peak power in exposure tools can be significantly increased. Although rCEL materials demonstrated nonlinear behavior in double-exposure mode, only marginal image quality and process window improvements were observed. Using the results from the simulation work described herein, materials development work is currently ongoing to enable potential ISTP and OTL materials for manufacturing.

A new biochip platform named "Mesoscale Unaddressed Functionalized Features INdexed by Shape" (MUFFINS) was developed in the Willson Research Group at the University of Texas at Austin as a potential method to achieve a new low-cost biosensor system. The platform uses poly(ethylene glycol) hydrogels with bioprobes covalently cross-linked into the matrix for detection. Each sensor is shape-encoded with a unique pattern such that the information of the sensor is associated with the pattern and not its position. Large quantities of individual sensors can be produced separately and then self-assembled to form random arrays. Detection occurs through hybridization of the probes with fluorescently labeled targets. The key designs of the system include parallel batch fabrication using photolithography and self-assembly, increased information density using multiplexing, and enhanced shape-encoding with automated pattern recognition. The development of two aspects of the platform – self-assembly mechanics and pattern recognition algorithm, and a demonstration of all the key design elements using a single array are described herein.

Table of Contents

List of Tables

List of Figures

Chapter 1

Introduction to Microlithography

1.1 A Brief History of Microelectronics

The use of electronics has become prevalent in modern societies. Many of the devices synonymous with the progress, from pocket calculators to mobile phones, would have been inconceivable just a century prior. Although Thomas Edison's invention of the vacuum tube ushered in the electronic age [13, 50], the pervasion of electronic devices into everyday life did not begin until the invention of the transistor in 1947 [73]. A replica of the first transistor is shown in Figure 1.1. The success of the transistor was due to its reduced weight, smaller size, and improved reliability when compared to the vacuum tube. These improvements enabled new technologies such as the portable transistor radio. Replacing vacuum tubes with transistors also dramatically reduced the size and power consumption of mainframe computers. As a result, mainframe computers became more affordable and widely used in business applications.

The next major leap in bringing electronics to the masses arrived with the invention of the integrated circuit (IC) by Jack Kilby and also independently by Robert Noyce in 1958 [37, 57, 79]. Kilby's first IC is shown in Figure 1.2. ICs combined various components of an electric circuit such as transistors,

Figure 1.1: Replica of the first transistor.

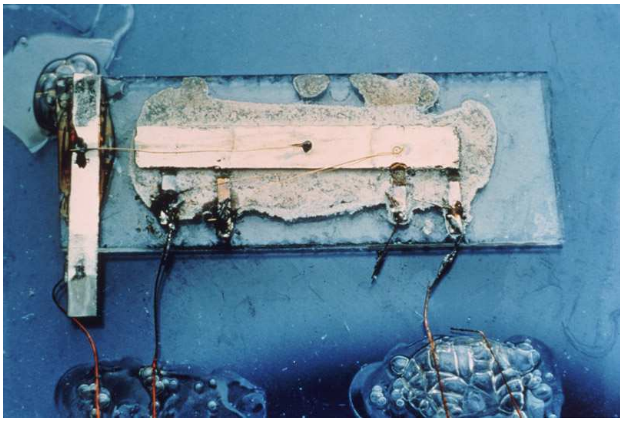

Figure 1.2: First integrated circuit invented by Jack Kilby at Texas Instruments. (*Courtesy of Texas Instruments*)

diodes, and rectifiers, etc. onto a single substrate. ICs retained the benefits and computing power of conventional transistors while eliminating the bulky and error-prone wires that connected the different components. Combining all the components on a single substrate also meant that the system size could be dramatically reduced. Immediate effects of the IC were seen with its use in the guidance systems of lunar bound rockets and the first pocket calculators. The first pocket calculator by Texas Instruments is shown in Figure 1.3. The latter brought previously unattainable computing power to the general public. From pocket calculators, ICs also enabled other technologies such as microprocessors and memory modules that launched the modern electronic age.

Figure 1.3: First handheld or pocket calculator by Texas Instruments. (*Courtesy of Texas Instruments*)

The common trends observed in each successive generation of technologies from the vacuum tube to the IC are increased reliability and reduced size. Within each generation, these trends are coupled with the continual need to reduce the cost of manufacturing while at the same time improving product performance. Heavy competition amongst manufacturers became a benefit to consumers as it drove down the price of the devices and also improved device performance – *i.e.* increased number of transistors. The demand to increase the number of transistors per device is illustrated with the commonly cited Moore's Law [56]. Gordon Moore, a co-founder and former CEO of Intel, postulated in 1965 that the number of transistors on a device would double once every year (Moore would later revise the prediction to double once every two years [55]). Over the years, the actual growth trend has stayed close to the prediction as shown in Figure 1.4. Since the actual die size has not grown at the same rate, this growth trend is possible due to the reduction in transistor size which is made possible by continual improvements in fabrication

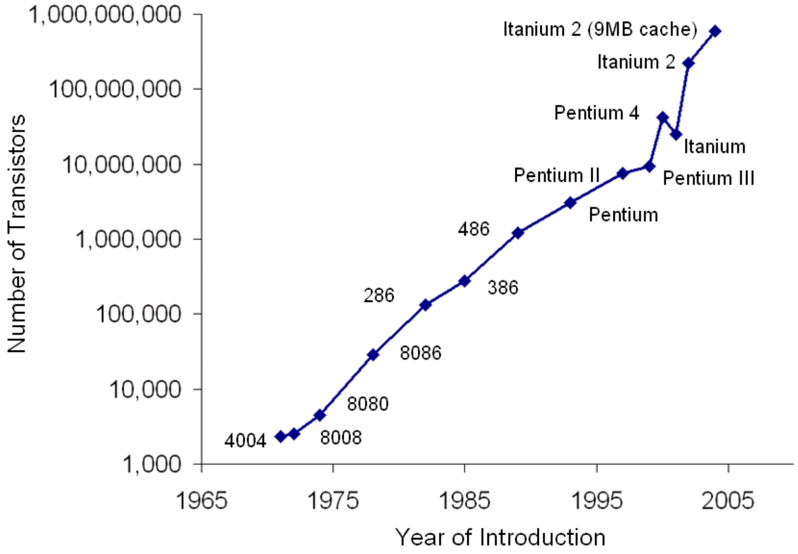

Figure 1.4: Exponential growth of the number of transistors on a microprocessor over time as predicted by Moore's Law. (Plot generated using transistor count data from Ref [32])

techniques. One of the main areas of improvement has been in the photolithographic process used to pattern the transistors and is briefly described below.

1.2 The Photolithographic Process

The main mode of patterning features on ICs is through the photolithographic process or photolithography. A schematic of a generalized photolithographic process is shown in Figure 1.5. In general, the process begins with

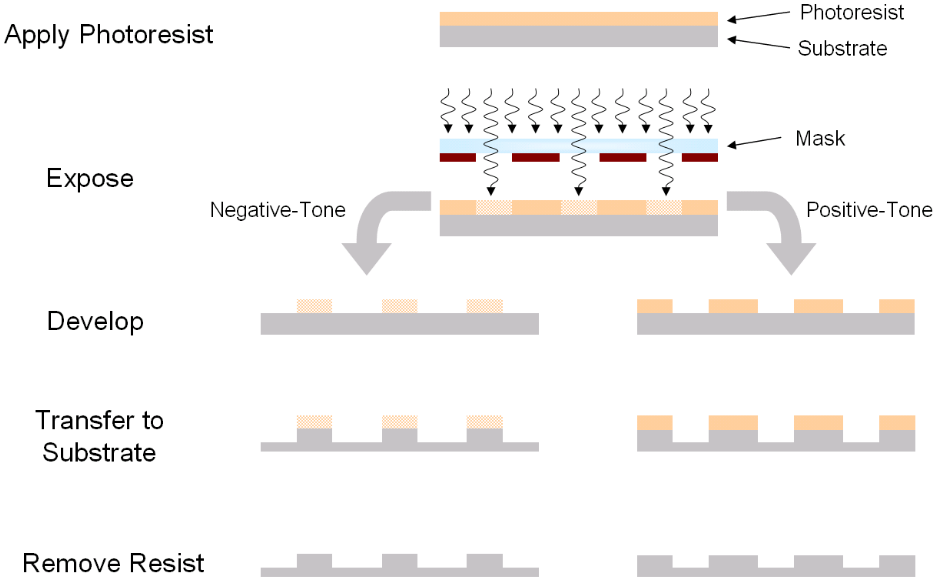

Figure 1.5: Schematic of the photolithographic process.

the application of a film of “photoresist” material (or simply “resist”) onto the desired substrate (wafer) to be patterned. Resists are polymeric materials that can undergo a solubility change upon exposure with light of a specific wavelength. Patterning is done by exposing light through a photomask (or simply mask) that contains the pattern to be transferred onto the resist film. The information is stored either as opaque or non-opaque regions on the mask thus modulating the pattern of light that is able to reach the resist. The light that is able to reach the resist induces a solubility change. Depending on the desired "tone" of the resist, the exposed regions can become either more soluble (positive-tone) or less soluble (negative-tone) compared to the unexposed regions. In a subsequent development step, the resist is then developed using a solvent (developer) that dissolves away the more soluble regions. The remaining resist on the substrate is used as an etch mask, i.e. it "resists" the etching of the underlying substrate, to transfer the pattern into the substrate. Finally, the resist is stripped to reveal the patterned substrate.

1.3 Development of the Photolithographic Process

The modern photolithograhic process has its roots in photography and the printing industry [7, 77, 81]. Since its inception and application to semiconductor manufacturing, the photolithographic process has undergone many technological iterations. Although many of the technological breakthroughs contributed to the miniaturization of semiconductor devices, two of the key aspects that have continually determined the minimum feature sizes are the ability of optical system used to generate smaller patterns and the availability of resist materials that respond to the transmitted patterns.

The first photolithographic systems were based on contact or proximity printing and appeared in the 1960s. They were based on shadow printing techniques from the printing industry. In contact printing, the patterned mask is brought into either physical contact with the resist-coated substrate whereas in proximity printing, the mask is brought into close proximity. The mask is subsequently flood exposed with 360 to 400 nm light to transfer the pattern to the resist. Initially, negative-tone resists with bis(arylazide)-cyclized rubber systems were used. Upon exposure, the bis(arylazide) forms a reactive intermediate that leads to cross-linking of the cyclized rubber molecules. Positive-tone resists were later developed based on diazonapthoquinone (DNQ) and novolac systems that improved resolution, thermostability, and etch resistance. The chemical structures of DNQ and novolac are shown in Figures 1.6 and 1.7.

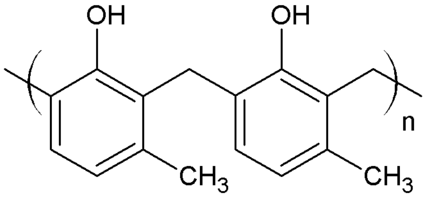

Figure 1.6: Structure of the novolac resin.

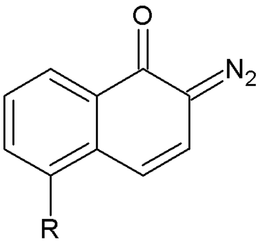

Figure 1.7: Structure of the DNQ moiety.

In this two-component system, DNQ is an additive to the novolac resin and acts as a dissolution inhibitor to decrease the rate at which novolac resin dissolves in aqueous alkaline developers. Upon exposure, the DNQ is converted to a photoproduct that is soluble in aqueous base and thereby increasing the solubility rate of the novolac resin.

The theoretical resolution of proximity printing, as defined by the minimum patternable feature size, of contact printing is given by the following expression

$$2b_{min} = 3\sqrt{\lambda\,(s + (1/2)z)} \qquad (1.1)$$

where b_{min} refers to the minimum width of a feature on a mask consisting of equal lines and spaces, λ is the wavelength of exposure, s is the gap between the mask and the resist, and z is the photoresist thickness [77]. With an exposure wavelength of 400 nm and 1 μm thick photoresist, contact printing ($s = 0$ when the mask and resist are in physical contact) has a theoretical limit of approximately 1 μm. However, practical commercial fabrication that was achievable was on the order of 5 μm. Since the mask and resist have to either be in contact or close proximity, the process is very sensitive to debris and wafer flatness. In addition, physical contact between the mask and the wafer often induces more defects.

Due to its limitations and the demand for sub-micron features, contact printing was eventually replaced by projection printing in the 1970s. Since then, projection printing has become the mainstay of microfabrication. In projection printing, a lens system is placed between the mask and the substrate, and used to focus the mask image onto the wafer. Defect densities decreased compared to contact printing because the mask no longer had to be in contact or close proximity to the substrate. However, projection printing required the use of complex and expensive lens systems.

The first projection printing systems used 1:1 imaging optics, meaning the dimensions on the mask and substrate are equal. These systems were able to lower defect densities and improve device yield. Overtime, the size of the of the wafers began to increase to accommodate the demand for higher throughput (more devices per wafer and exposure). With full-field 1:1 imaging, this also required an increase in the size of the mask. Eventually, the rate of increase in mask size could not keep up with the increase in wafer size as large masks were difficult to fabricate. It was also difficult to construct an imaging system to project the entire mask image.

The projection challenges were resolved by implementing new printing techniques that did not require simultaneous full-field imaging in a single exposure. A "scanning" method was introduced where by only a small section of the mask image is imaged at a time through a narrow slit. The slit usually spanned one full-width direction of the mask. During exposure, both the mask and wafer were moved by mechanical stages to "scan" the entire mask. It was a simpler task to construct an imaging system to project the slit, however, the the mask size was not reduced.

Another method called 'step-and-repeat' was also introduced in the 1970s. In step-and-repeat, the full-field mask size is reduced to only the essential areas necessary to pattern a single or few devices. Small portions of the wafer are patterned at a time. The mask is then "stepped" to a new position on the wafer to "repeat" the exposure until the whole wafer is patterned. Although this method had reduced throughput compared to full-field exposure, the mask fabrication specifications and the imaging optics were more manageable. Soon after, the merits of both scanning and step-and-repeat systems were combined into the "step-scan" method. In step-scan, an additional "scanning" element is incorporated into the step-and-repeat such that during each exposure, both the mask and wafer are moved in opposite directions and the image is transferred through a small slit.

Reduction printing also emerged to supplement the step-and-repeat method. In reduction printing, the dimensions on the mask is intentionally fabricated to be larger than the eventual target dimension on the wafer by a designated reduction factor. The mask image is reduced by the imaging optics before reaching the wafer. This is advantageous because the critical dimensions on the mask are larger and easier to fabricate. Furthermore, any defects on the mask are also reduced in size before reaching the wafer. Several reduction ratios (mask dimension to wafer dimension) such as 10:1, 5:1, and 4:1 were introduced by equipment manufacturers. An appropriate reduction ratio needs to balance throughput and mask size. Larger reduction ratios enhances the benefits of defect reduction but result in a smaller field-size. To maintain throughput, the field-size on the wafer needs to be sufficiently large to minimize the number of steps per wafer. Currently, a reduction ratio of 4:1

is used by most manufacturers because it has the optimal trade-off between throughput and mask size.

The theoretical limit of projection printing for a given system is described by the Raleigh criteria

$$Resolution = \frac{k_1 \cdot \lambda}{NA} \tag{1.2}$$

where k_1 is the process aggressiveness factor, λ is the wavelength of the imaging tool, and NA is the numerical aperture of the imaging lens. Examination of Equation 1.2 reveals that the minimum achievable feature sizes can be reduced by either decreasing k_1 or λ, or increasing NA. Indeed, much effort has been put forth toward each of those areas and will be described briefly below.

The NA of a particular imaging system is a function of all of the lenses in the imaging stack and can be described by the following

$$NA = n \sin \theta \tag{1.3}$$

where n is the index of refraction of the imaging medium and θ is the angle of the incident light. As can be seen in Equation 1.3, increasing the NA can be achieved by increasing the index of refraction of the imaging medium or the angle of incidence. Increasing n requires using new materials in the lens stack but is usually limited to 1.0 by the air gap that exist between the lens and wafer. Increasing θ often required constructing larger lenses to capture light with a larger incident angle. As the size of the lens increases, the manufacturing difficulties also increase, particularly in the growth of the lens materials and correction of aberrations. Early exposure systems had NAs on the range of 0.3 in the 1980s and the NA gradually progressed to 0.93 over the next 20 years. As noted, the maximum n that was achievable was limited by the air gap between the lens and the wafer. However, with the recent introduction of "immersion lithography", whereby the air gap is replaced by an immersion fluid, the NA of the system was raised above 1.0. First generation immersion tools used water, which has a refractive index of 1.44 at 193 nm, and is able to achieve NA of 1.35.

The reduction in the minimum achievable feature size can also be accomplished by reducing the wavelength of exposure. The selection of an exposure wavelength is dictated by the availability of a light source, optics, and the suite of chemistries that will respond to that wavelength of light. Early systems used exposure wavelengths between 360 nm to 450 nm and resist chemistries that were inherited from the printing industry. Mercury arc lamps were used as the primary light sources. The discharge arc of these sources emits high intensity light at very specific wavelengths corresponding to Hg emission lines such as G-line (436 nm), H-line (404 nm), and I-line (365 nm). The intensity and wavelength output of the sources were very compatible with the DNQ-Novolac resist chemistries. However, the compatibility trend would not continue into the Deep-UV (DUV) regime (240 nm - 260 nm) due to photosensitivity issues. Both the DNQ and novolac compounds have strong absorbances in the DUV. Furthermore, the spectral output of the mercury arc lamp in the DUV is much lower compared to previous exposure wavelengths. Fortunately, these issues were resolved by Willson and co-workers at IBM with the invention of resists with built-in chemical amplification [18, 34, 35].

Chemically-amplified resists contain two essential components, a photoacid generator (PAG) and a functionalized polymer resin. As the name implies, PAGs are compounds which can generate acid molecules upon irradiation with light. The generated acid molecule is then used to catalyze reactions with functional groups on the resin. The reactions alters the solubility or reactivity in different areas of the resist and facilitates pattern transfer. Since the acid molecule is not consumed, a single photon absorption event that generates acid can result in many more reaction events, and, in this way, the photosensitivity is amplified. A sample chemically-amplified resist system is shown in Figure 1.8. This system is based on poly(*p*-hydroxystyrene) or PHOST

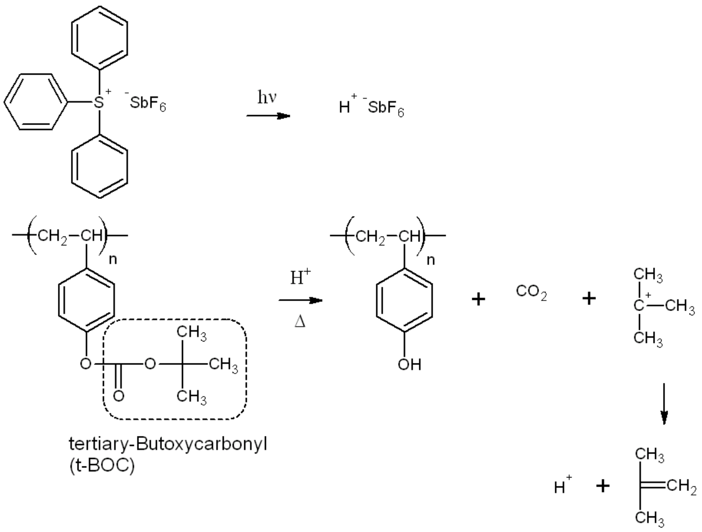

Figure 1.8: Sample Deep-UV chemically-amplified resist. *Adapted from Ref. [77]*

polymer that is more transparent in DUV compared to novolac. The polymer is functionalized with a tertiary-butoxycarbonyl (*t*-BOC) group to form poly(*p*-*t*-butyloxycarbonyloxystyrene) or PBOCST. The functionalization of the PHOST changes the solubility of the polymer; PHOST is soluble in polar solvents whereas PBOCST is soluble in organic solvents. After exposure, the acid molecules generated from the triphenylsulfonium hexafluoroantimonate PAG catalyze (with appropriate post-exposure bake) "deprotection" of the *t*-BOC group from the polymer resin to form PHOST. Depending on the application, the exposed film can be developed in a polar solvent to generate a positive-tone image or a nonpolar organic solvent to generate a negative-tone image.

Shortly after the transition to the DUV regime, the power output of the light source increased with the introduction of the KrF excimer laser. These lasers are tuned to provide high output at 248 nm. The current generation of exposure tools uses 193 nm as the exposure wavelength. As with the switch from I-line to 248 nm exposure wavelengths, a new set of resist chemistries was required when switching from 248 nm to 193 nm. This is mainly due to the high absorbance of most organic compounds in the 193 nm regime, including the phenolic compounds contained in PHOST [33].

New classes of materials based on polymethacrylates or norbornene-maleic anhydride copolymers were developed for the 193 nm application. These materials replaced the highly absorbing aromatic groups with more transparent alicyclic adamantyl or norbornyl groups. The alicyclic group serves as a dissolution inhibitor and also provides the necessary dry etch resistance for pattern transfer. The chemical amplification behavior is preserved as the dissolution inhibitors remain acid-cleavable using the typical PAG acid generation scheme. Sample resist systems are shown in Figures 1.9 and 1.10.

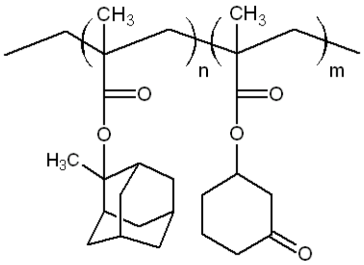

Figure 1.9: Sample 193 nm polymethacrylate-based resist polymer. *Adapted from Ref. [33]*

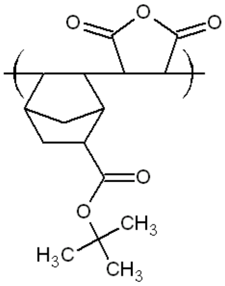

Figure 1.10: Sample 193 nm norbornene-based resist polymer. *Adapted from Ref. [33]*

The k_1 process aggressiveness factor is an overall measure of the effectiveness of a patterning process excluding the effects of λ and NA. This includes factors such as the illumination setup, mask characteristics, development characteristics, level of anisotropy during etching, volatility of the casting solvent, etc. Thus, reduction of k_1 can be achieved by improvement of many processing steps. Specifically, many of these improvements are collectively referred to as resolution enhancement techniques (RETs).

Some of the more prominent RETs relevant to the imaging process include the use of partially coherent illumination, phase-shift mask, optical proximity correction, and multiple exposure lithography. For example, the theoretical limit of k_1 when imaging with coherent illumination is 0.5, but is reduced to 0.25 using partially coherent illumination [82]. The RET of particular interest to this document is the use of multiple exposures. In this approach, lithographic designs that are beyond the capabilities of current state-of-the-art techniques in a single exposure can be split into multiple exposures. The original design is split into less complex designs each patternable by current techniques. In theory, the combination of the multiple exposures would yield the original design. Although this would incur additional processing steps, the advantage is the possibility of achieving sub k_1 (< 0.25) patterning. The use of double exposure lithography, a specific type of multiple exposure lithography, is explore in subsequent chapters of this work.

1.4 Future Lithography Options

The demand for smaller and cheaper semiconductor devices will serve as a constant driving force to improve the resolution as described by the Raleigh criteria. The use of double patterning lithography and double exposure lithography as a pathway to extending the resolution capability of current exposure tools by reducing k_1 is rapidly gaining pace and will be discussed in the chapters to follow. A large effort is ongoing to develop the next generation light source using extreme ultra violet (EUV) at 13.4 nm. Outside of optical lithography, other promising future lithography options include nanoimprint lithography and ebeam lithography.

1.5 Dissertation Outline

The research contained in this dissertation details work performed in two topic areas – materials modeling for double exposure applications and development of a biosensor platform. These two distinct topics are related by their common use of advanced photolithographic patterning techniques with organic materials.

The first set of chapters describes materials modeling work in the search of next generation double exposure materials. Chapter 2 provides an introduction to various double-exposure and double-patterning strategies and presents the case for the potential benefits of the double-exposure technique. Several potential double exposure materials are also described. Chapters 3 and 4 presents the results from the feasibility studies performed for each potential materials using simulation. The details of the simulator used to perform the studies are described in Chapter 5. The results aided in guiding synthetic material development efforts. This section concludes with a summary of current materials development efforts and outlook in Chapter 6.

The latter portion of the dissertation describes the work related to the development of the MUFFINS biosensor platform. The MUFFINS platform was developed as an alternative low-cost method of building biosensor microarrays. Chapter 7 provides an introduction to the different aspects of the platform including parallel fabrication, multiplexing, and shape-encoding. Chapters 8 and 9 describes work done in the areas of self-assembly modeling and automated pattern recognition to complete the platform development. The different design aspects of the platform are integrated in a final demonstration as described in Chapter 10.

Chapter 2

Introduction to Double-Exposure Lithography

2.1 Introduction

The current technological progression of the photolithography industry has reached a limit in the maximum achievable resolution. Resolution as determined by the half pitch critical dimension (CD) is limited by the Rayleigh equation

$$CD = \frac{k_1 \cdot \lambda}{NA} \tag{2.1}$$

where k_1 is the process aggressiveness factor, λ is the wavelength of the imaging tool, and NA is the numerical aperture of the imaging lens. To reduce the half pitch CD, the industry must reduce k_1 or λ , or increase NA. The theoretical minimum value for k_1 with single exposure is 0.25 [82], but the generally accepted manufacturability limit is 0.27. The current industry standard imaging tool has a wavelength of 193 nm. Future imaging tools are proposed to operate in the Extreme Ultra Violet (EUV) range with a λ of 13.4 nm, however, the EUV technology will most likely not be viable until after 2013. With water immersion lithography, the maximum achievable NA is approximately 1.35. Increasing the NA beyond 1.35 requires simultaneous development of a high index lens material, high index fluids and, high index resists. Without major breakthroughs in optical materials, NA will plateau near 1.35. Given these parameters, the current CD limit is approximately 38 nm half pitch.

To enable lithography at sub 38nm half pitch, the industry will need to consider alternative resolution enhancement technologies. Two exposure passes have been proposed as a possible resolution enhancement technique for existing photolithography imaging systems. A single mask with high feature density that is difficult to resolve can be split into two exposures each with lower feature density that can be easily resolved. When combined, the two exposures replicate the mask that was difficult or impossible to resolve.

2.2 Double-Exposure Lithography versus Double-Patterning Lithography

Double-exposure lithography (DEL) and double-patterning lithography (DPL) are proposed approaches to performing the two exposure passes. DEL is defined as a two exposure pass lithographic process that does not require the removal of the wafer from the exposure tool chuck between passes. DPL is defined as a two exposure pass lithographic process that requires a chemical development of the photoresist layers and possibly an intermediate etch step. The DPL processing approaches will require the removal of the wafer from the exposure tool chuck and loss of overlay registration. DEL and DPL processes are illustrated in Figure 2.1. The benefit of DEL and DPL is the ability to use existing exposure tools to print technology nodes below the NA limit for single exposure processes. This could mean a lower cost of ownership as these

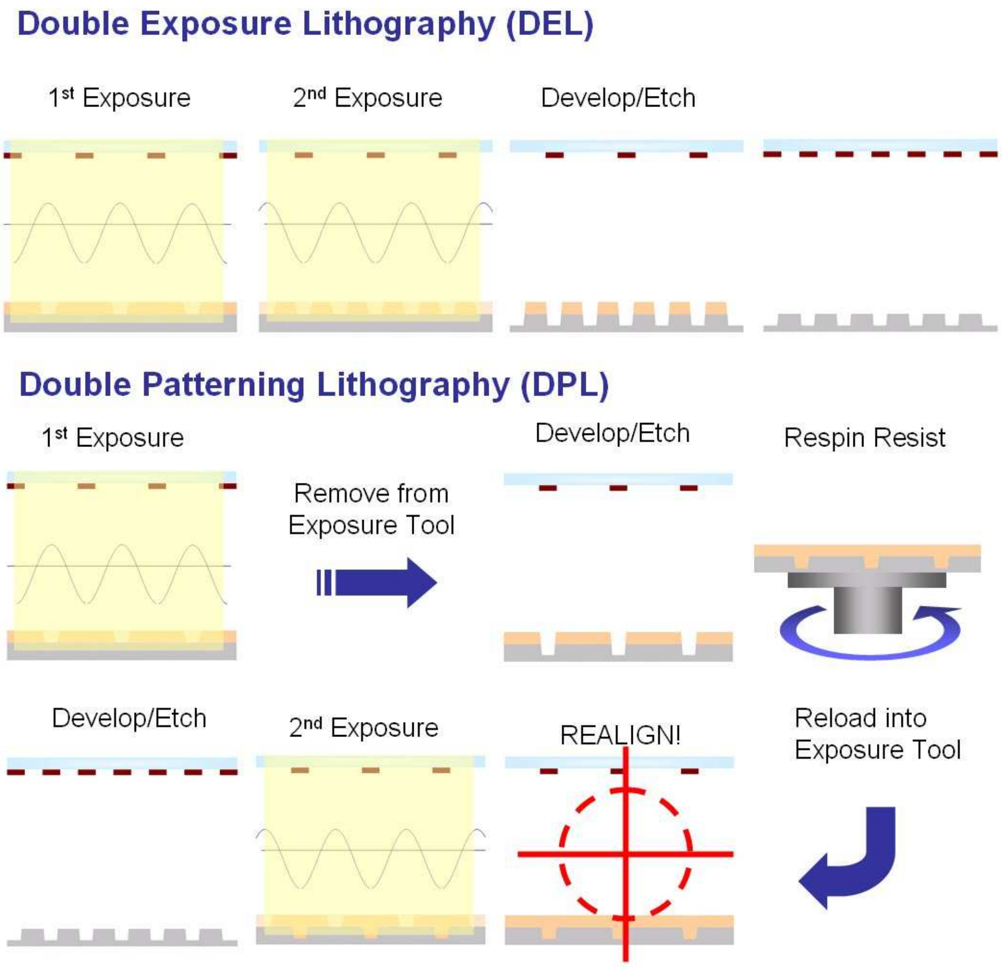

Figure 2.1: Comparison of the double-exposure lithography (DEL) and double-patterning lithography (DPL) (development/etch scheming shown) processes.

techniques can in principle be deployed without costly capital investment. However, the two exposure passes require doubling the number of masks and reduced throughput due to increased processing time. The process time is dramatically increased in the DPL process because of the additional process steps compared to the DEL process. In addition, the removal of the wafer from the wafer chuck between exposures poses severe overlay issues that may be difficult to overcome, especially at the CDs where this technology will be implemented. The DEL process only introduces an additional exposure pass, and since the wafer is not removed from the imaging tool between exposures, the overlay issues are minimized. The reduced cost of ownership of DEL suggests that it would be the preferred technique.

2.3 Impact on Mask Design

The preliminary theoretical imaging studies show that DEL with positive tone resists is a trench-based process. For a single exposure pass, positive tone resists should lead to line-based lithography where opaque regions on the mask produce lines in the resists plane after development while negative tone resists should lead to trench-based lithography where opaque regions on the mask produces trenches or spaces on the resist plane after development. The lines and spaces are transferred into the wafer with subsequent etch steps. The two processes are illustrated in Figure 2.2.

DEL complicates the concept of mask tone because the lower intensity regions under the opaque regions in the first exposure pass become the high

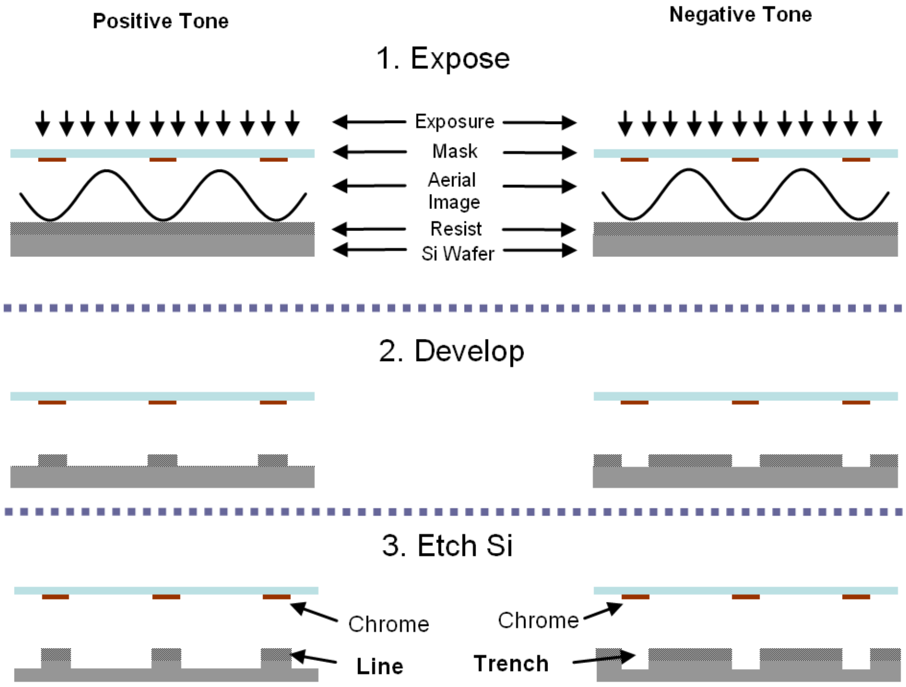

Figure 2.2: Line versus trench based lithography.

intensity regions in the second exposure pass. The summation of the two exposure passes leads to an image in resist that develops away all regions under bright areas in either mask in positive tone resists. The resist features remain only in regions where both exposure masks have opaque regions. While in negative tone resists, the regions under the bright regions in either mask would remain after development and form lines. This is illustrated in Figure 2.3 for positive tone resists.

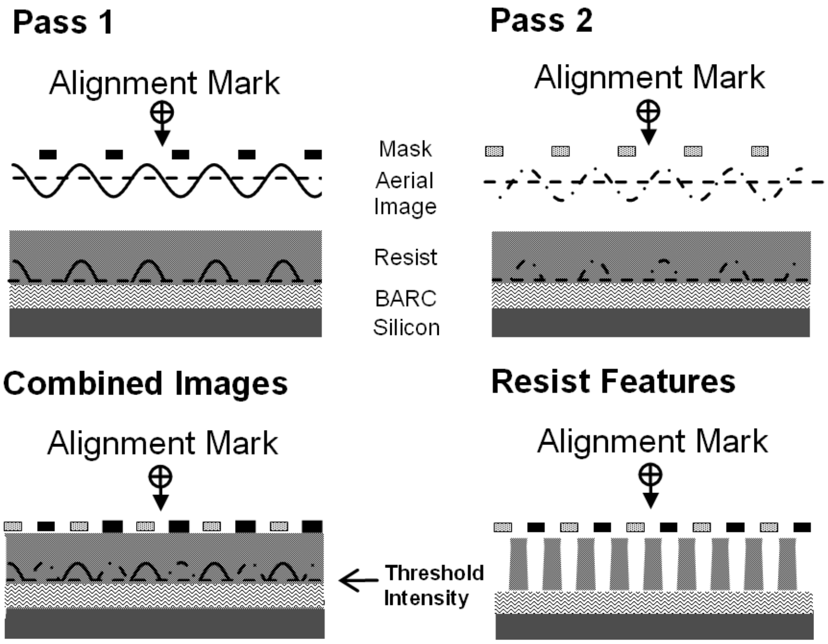

Figure 2.3: Double-exposure lithography effects on trench and line based lithography.

Figure 2.3 shows two exposure passes and the combined energy distribution in the resist for an optical threshold system. Notice that in the "Combined Images", the peaks of high intensities correspond to the opaque region of the exposure mask from the other exposure. The valleys of the combined image correspond to regions where both masks have opaque regions either directly above or in close proximity. The final resist features are located at the valleys of the combined image.

The characteristic of trench based imaging has important implications for the design of masks for DEL lithography and positive tone resists. The issues are different depending upon the class of the desired feature types. Dark field features should perform as expected with no consequences, however, care should be taken when patterning bright field features. The trench-based nature requires that mask design fracturing must be based on “trenches” or “spaces” surrounding gates. In other words, the size of a gate is no longer defined by the size of the corresponding opaque region on the mask and exposure dose, but rather the trenches around the gate and the mask registration errors between the two masks. The bright field design issues may be resolved by switching to negative tone double-exposure resists.

To demonstrate the trench-based implications on mask fracturing, consider the mask fracturing required for the printing of contact holes (dark field features) and “5-bar” patterns (bright field features). The mask fracturings are shown in Figure 2.4 and Figure 2.5. Figure 2.4 shows a target image of two columns of contact holes. The mask is fractured for DEL such that the mask for the first exposure pass contains contact holes in alternating diagonals and the mask for the second exposure pass contains the complementary contact holes not included in the first exposure pass. It should be noted that

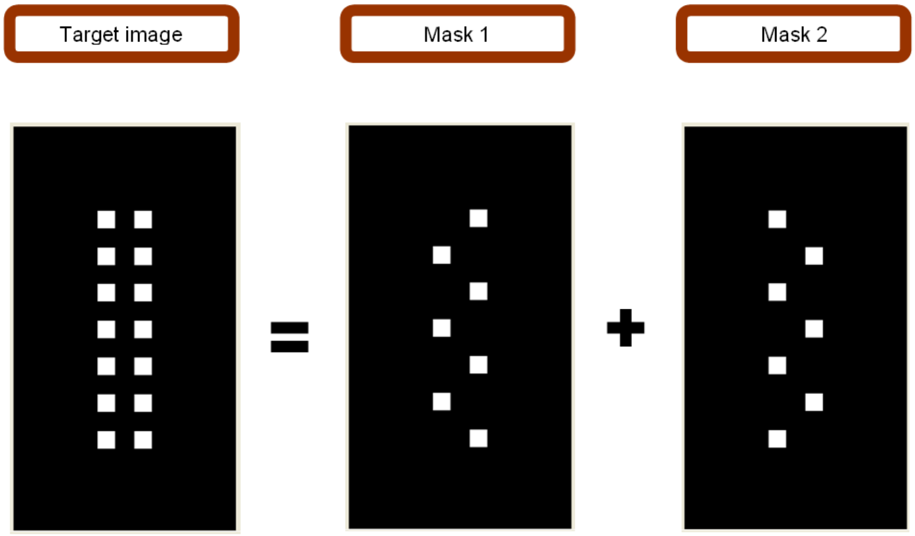

Figure 2.4: Mask fracturing scheme for contact holes.

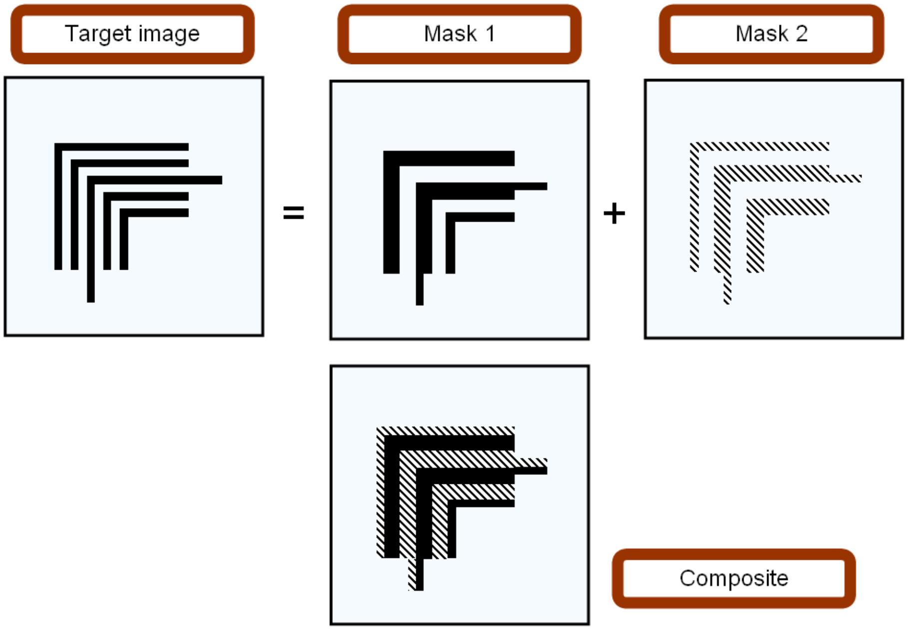

Figure 2.5: Mask fracturing scheme for a 5-Bar pattern.

although the half pitch spacing between neighboring contact holes in each column and row can be theoretically reduced by a factor of two, the reduction is actually limited by the diagonal spacing between neighboring contact holes in each mask which is constrained by the single exposure resolution limit. For the printing of contact holes, the pitch can be reduced by approximately 29% using DEL.

Figure 2.5 shows the mask fracturing scheme for the 5-bar pattern. Since the lines are bright-field features, the trench-based lithography requires the mask be fractured such that the opaque areas are shifted where lines in resist correspond to spaces in the masks. The center of the non-opaque regions in each exposure pass combine to form the trenches on each side of a line. The edges of the non-opaque regions would receive lower doses in the resist and form the lines. The examples shown in Figure 2.4 and Figure 2.5 demonstrate that both the DEL and DPL process increase the complexity in mask design.

2.4 Resist "Memory" Effect

The DEL infrastructure is currently available on existing state of the art exposure tools. However, imaging below a k_1 value of 0.25 with double-exposure is impossible without the development of new materials. Conventional resists have a "memory" effect that prevents proper replication of the mask image. That is, sub-threshold exposure in the first exposure pass reduces the dose required to render the resist soluble in the second exposure pass. For example, the normalized aerial image intensities for the first exposure pass reaching the resist of equal lines and spaces can be described by the following

$$I_{Pass\,1} = A\cos^2\left(\frac{\pi \cdot x}{pitch}\right) + B, \tag{2.2}$$

where A is a constant describing the amplitude and B is the minimum image intensity. For the second exposure pass, the mask and, consequently, the aerial image are translated by half pitch and lead to the following intensity function

$$\begin{aligned} I_{Pass\,2} &= A\cos^2\left(\frac{\pi \cdot x}{pitch} + \frac{\pi}{2}\right) + B \\ &= A\sin^2\left(\frac{\pi \cdot x}{pitch}\right) + B. \end{aligned} \tag{2.3}$$

The photochemical response of the resist results in a linear summation of the absorbed intensities from the two exposure pass. This leads to the following intensity function within the resist

$$\begin{aligned} I_{Sum} &= I_{Pass\,1} + I_{Pass\,2} \\ &= A\cos^2\left(\frac{\pi \cdot x}{pitch}\right) + A\sin^2\left(\frac{\pi \cdot x}{pitch}\right) + 2B \\ &= A + 2B = \text{a Constant!} \end{aligned} \tag{2.4}$$

Consequently, the two individual mask images are not resolved when double exposed. This concept is illustrated in Figure 2.6.

The resist system converts the separate light images, intensity versus position, into chemical images, chemical composition versus position. Mathematically, this conversion of the light image into a chemical image can be represented by a translation function $f(I)$. In the case of standard resist systems, this translation function has the linear addition property

$$f\left(I_{Pass\,1} + I_{Pass\,2}\right) = f\left(I_{Pass\,1}\right) + f\left(I_{Pass\,2}\right). \tag{2.5}$$

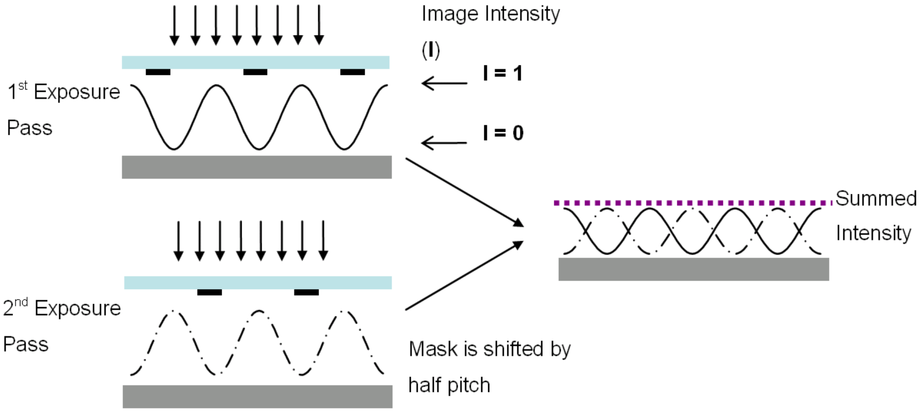

Figure 2.6: Summation of the intensity of two exposure passes and the effect of dose reciprocity.

Resolving the mask features, *i.e.* generation of image contrast, requires a material with a nonlinear response to exposure such that

$$f\left(I_{Pass\,1} + I_{Pass\,2}\right) \neq f\left(I_{Pass\,1}\right) + f\left(I_{Pass\,2}\right) \tag{2.6}$$

and the "resist memory" behavior is minimized.

2.5 Potential Double-Exposure Lithography Materials

Several materials have been proposed to implement a nonlinear response to exposure and theoretically permit double-exposure pitch doubling including contrast enhancement layers (CELs), two-photon materials, intermediate state two-photon (ISTP) materials, and optical threshold layers (OTLs). These materials and their theory of operation are described in the following sections.

2.5.1 Contrast Enhancement Layer

Contrast enhancement layers (CELs) are strongly absorbing materials that increase transparency, or photobleach [23], when exposed to light. A CEL is normally applied directly on top of the resist layer. During exposure, energy is first devoted to photobleaching the CEL. As the CEL becomes transparent, the energy is then able to reach the resist and initiate the solubility switch. Light can only penetrate through the CEL in regions where aerial image intensities are high (non-opaque regions on the mask) and cannot reach the resist in regions where aerial image intensities are lower (opaque regions on the mask). This introduces a nonlinear transfer of the applied aerial image into the photoresist and improves the resolution. CELs can be divided into two different subtypes, namely, reversible (rCEL) and irreversible (irCEL). The main difference between the two subtypes is that, in rCELs, the photobleached regions can return to the initial opaque state between exposure passes whereas in irCELs, the photobleaching is irreversible. Details on the existing chemistries and transmission characteristics for CELs have been described in previously published work [3, 8, 15, 21, 41, 80].

We have investigated the use of rCELs with 50 nm line/space patterns in single exposure mode through simulation with PROLITH 9.3. The film stack from top to bottom consisted of rCEL, 100 nm of typical 193 nm resist, and 28 nm of a single layer of bottom anti-reflective coating (BARC) (n = 1.82, k = 0.46). The substrate was silicon with a 2 nm layer of SiO_2. Briefly, the simulation conditions are listed in Table 2.1. The results are shown in

Table 2.1: Simulation parameters used for the 50 nm L/S with rCEL in single exposure mode.

Property	Value
NA	1.2
Illumination	Cross-quasar
Blade Angle (°)	35
σ_{outer}	0.9
σ_{inner}	0.7
Resist Refractive Index	1.70
Resist Dill A ($\mu\mathrm{m}^{-1}$)	0
Resist Dill B ($\mu\mathrm{m}^{-1}$)	1.47
Resist Dill C ($\mathrm{cm}^2/\mathrm{mJ}$)	0.0478
Resist [Q]/[PAG]	0.2
Resist M_{th}	0.75
Resist $\mathrm{D_H}$ (nm^2/s)	0.223
Resist $\mathrm{D_Q}$ (nm^2/s)	0.0
Resist $\mathrm{k_a}$ (1/s)	0.100
Resist $\mathrm{k_b}$ (1/s)	4.85×10^8
rCEL Thickness (nm)	$0 - 500$
rCEL Refractive Index	1.69
rCEL Dill A ($\mu\mathrm{m}^{-1}$)	$0 - 5$
rCEL Dill B ($\mu\mathrm{m}^{-1}$)	0
rCEL Dill C ($\mathrm{cm}^2/\mathrm{mJ}$)	0.11
Development Model	Enhanced Mack Model
Development Rmax (nm/s)	400
Development Rmin (nm/s)	0.01
Development Rresin (nm/s)	400
Development n	3
Development l	3.98
Development Time (s)	60

Figures 2.7 and 2.8.

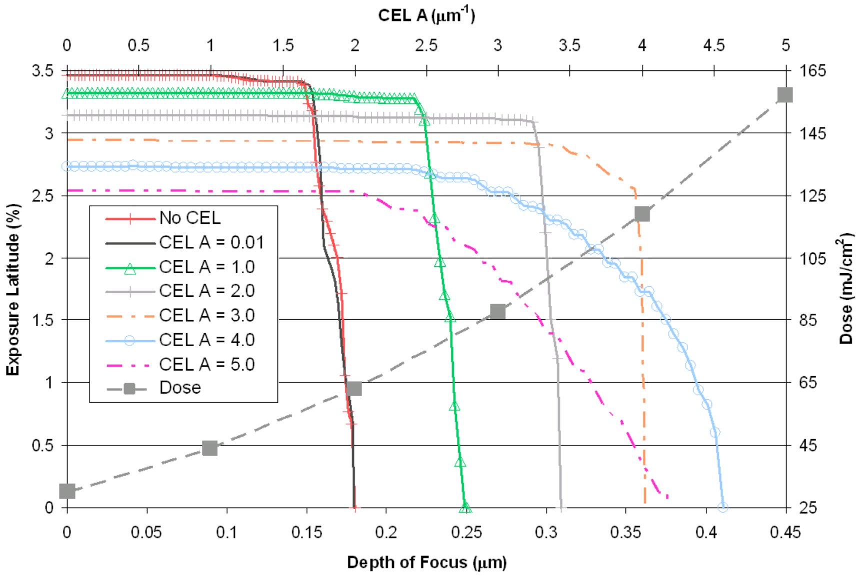

Figure 2.7: Process window of 50nm L/S with 400 nm of rCEL varying the Dill A parameter

Figures 2.7 and 2.8 show that the use of the rCEL moderately increased the depth of focus for the process, but the increase comes at the cost of increases in exposure doses, almost by a factor of 10 in the case of A $= 5.0\ \mu\text{m}^{-1}$ when compared to the No CEL case, and in most cases decreases in EL.

2.5.2 Two-Photon Materials

Two-photon photoresist systems involve the incorporation of photoacid generators (PAGs) that require the simultaneous absorption of two photons to induce the photochemical acid generation. The chemical reaction for a

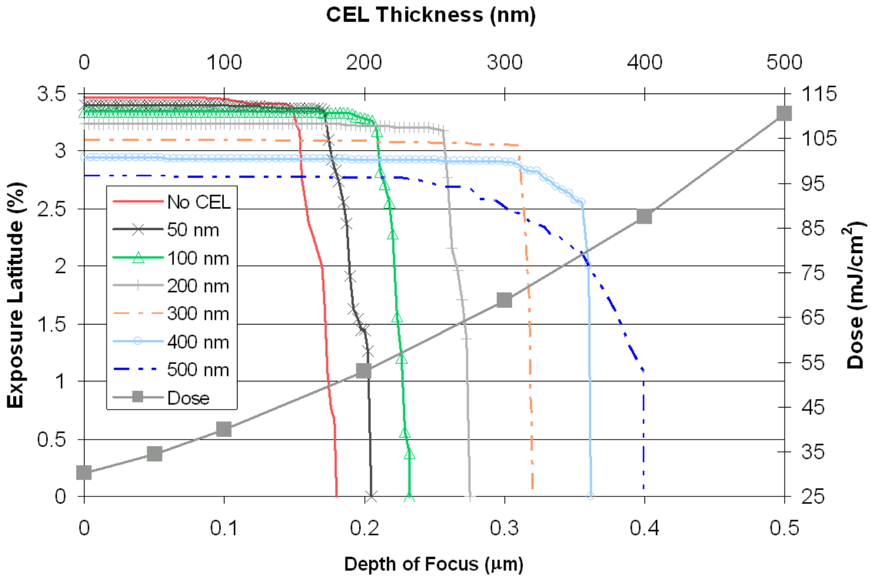

Figure 2.8: Process window of 50nm L/S with rCEL having Dill A parameter of 3.0 μm^{-1} varying rCEL layer thickness

two-photon photoacid generator can be described by the following reaction

$$\mathrm{PAG} + I\left(h\nu\right) + I\left(h\nu\right) \xrightarrow{\phi} \mathrm{Acid}, \tag{2.7}$$

where ϕ is the quantum efficiency of the two-photon photochemical reaction. Since the simultaneous absorption of two photons is required for the reaction, the probability of conversion is proportional to the light intensity squared, which provides a nonlinear response to exposure energy

$$f\left(I\right) \approx I \cdot I \tag{2.8}$$

and the DEL conversion is

$$\begin{aligned} & f\left(I_{Pass\,1}\right) + f\left(I_{Pass\,2}\right) \\ \approx & I_{Pass\,1} \cdot I_{Pass\,1} + I_{Pass\,2} \cdot I_{Pass\,2} \\ \neq & f\left(I_{Pass\,1} + I_{Pass\,2}\right). \end{aligned} \tag{2.9}$$

Unlike the CEL, two-photon materials are not enhancement layers that are applied on top of existing resists, but rather the nonlinear response is incorporated directly into the resist formulation. This eliminates complexities introduced by the addition of an extra film layer such as depth of focus and material compatibility.

Two-photon resist systems for microfabrication using laser writing systems have been reported previously [42]. These systems employ specially designed PAGs with high two-photon absorbance cross-sections. High efficiency two-photon PAGs have not yet been developed to work with 193 nm. Analysis of the two-photon reaction kinetics suggests that a very large increase in exposure source output would be required to produce a viable level of process throughput.

For example, the two-photon absorbance transition probability of a two-photon PAG can be more specifically described by the following expression

$$P_{2h\nu} \approx \sigma_2 \cdot \int I^2 dt \tag{2.10}$$

where σ_2 is the two-photon absorbance cross section, with a typical value of approximately $5 \times 10^{-47} s - cm^4/photon$ [84] for current two-photon PAGs. Using characteristics typical of current exposure tools (193 nm, 10 mW/cm^2, 4000 Hz, 20 ns FWHM) and assuming a Gaussian intensity profile, the absorbance transition probability per laser pulse is

$$\begin{aligned} P_{2h\nu} &= \frac{\sigma_2}{2} \cdot \left(\frac{A0 \cdot \lambda}{h \cdot c}\right)^2 \frac{0.664}{\text{FWHM}} \\ &= \sigma_2 \cdot 9.77 \times 10^{31} \frac{photon^2}{pulse \cdot s \cdot cm^4}, \qquad (2.11) \end{aligned}$$

where $A0$ is the energy per unit area delivered by each pulse, λ is the exposure wavelength, h is Planck's constant, c is the speed of light, and FWHM is the full width at half maximum of the laser pulse [44]. Finally, the number of laser pulses necessary to produce 20% conversion of PAG into acid, assuming a quantum efficiency of 1.0 for the PAG, is

$$\begin{aligned} \#pulses &= \frac{0.20}{9.77 \times 10^{31} \frac{photon^2}{pulse \cdot s \cdot cm^4} \cdot 5 \times 10^{-47} \frac{s \cdot cm^4}{photon}} \\ &\approx 4 \times 10^{13} pulses. \qquad (2.12) \end{aligned}$$

Alternatively stated, the fraction of converted PAG for a 10 s exposure would be on the order of

$$\begin{aligned} P_{2h\nu} &= 4.9 \times 10^{-15} pulse^{-1} \cdot 10s \cdot 4000 \frac{pulses}{s} \\ &\approx 2 \times 10^{-10}. \end{aligned} \tag{2.13}$$

Given the reaction kinetics of two-photon reactions and the typical exposure source intensity of the projection photolithographic processes, the analysis described in Equations 2.10–2.13 indicates that a two-photon photoresist system would require very long exposure time to achieve sufficient amount of photochemical reaction for imaging. The probability in Equation 2.11 can be increased by reducing the FWHM of the laser, i.e. using a femtosecond laser, increasing $A0$ to similar that of a direct laser write focused beam, or increasing σ_2 by nine orders of magnitude to $5 \times 10^{-38} s - cm^4/photon$. Therefore, without a very large increase in exposure source intensity, the existing two-photon PAG materials could not maintain the throughput level typical of current lithographic process. As such, the two-photon material type was not included in the simulation studies.

2.5.3 Intermediate State Two-Photon Materials

Intermediate state two-photon (ISTP) layers are materials that generate acid molecules in a two step process. Similar to two-photon materials, ISTP materials alter the acid generation behavior of the resist medium. Although each step requires the absorption of a photon, ISTP materials are not true two-photon processes in that the acid production does not have a quadratic dependence on dose. An example reaction sequence is illustrated graphically in Figure 2.9. Figure 2.9 shows a reaction sequence initially involving an inactive latent PAG that is brought to an activated PAG state after the absorption of a single photon. The subsequent absorption of a second photon by the intermediate activate PAG causes acid generation. An important feature, further explained below, to notice is that the intermediate species must be able to revert to the original or decay to another species. Although Figure 2.9 shows a 'latent PAG' approach, the reaction can be generalized in the following manner

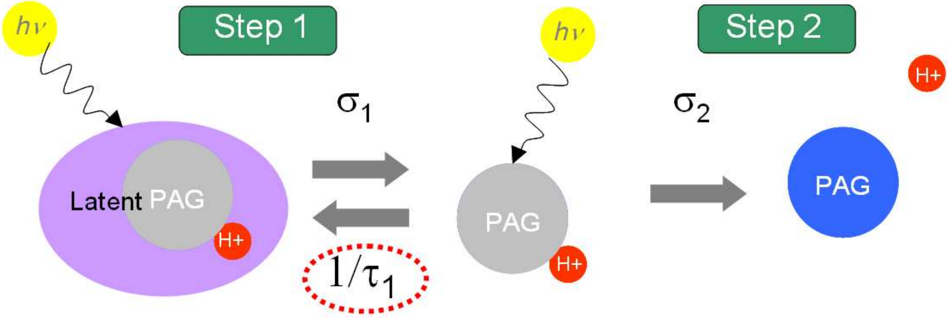

Figure 2.9: Example reaction sequence for a potential ISTP material.

$$\begin{aligned} A + I\,(h\nu) \; &\underset{1/\tau_1}{\overset{\sigma_1}{\rightleftharpoons}} \; B \\ B + I\,(h\nu) \; &\underset{1/\tau_2}{\overset{\sigma_2}{\rightleftharpoons}} \; [Acid], \end{aligned} \qquad (2.14)$$

where σ_1 and σ_2 represent the cross-sections with respective quantum efficiencies included and τ_1 and τ_2 represent the lifetimes of the species. The system of rate equations governing the production of acid is as follows

$$\begin{aligned}
\frac{d[A]}{dt} &= -\sigma_1 I\,(h\nu)\,[A] + 1/\tau_1[B] \\
\frac{d[B]}{dt} &= \sigma_1 I\,(h\nu)\,[A] - \left(1/\tau_1 + \sigma_2 I\,(h\nu)\right)[B] + 1/\tau_2[Acid] \\
\frac{d[Acid]}{dt} &= \sigma_2 I\,(h\nu)\,[B] - 1/\tau_2[Acid]. \qquad (2.15)
\end{aligned}$$

For cases where

$$1/\tau_1 \gg \sigma_1 I\,(h\nu) \;\text{ and } 1/\tau_2 \approx 0, \qquad (2.16)$$

the steady-state approximation may be applied such that

$$\frac{d[B]}{dt} = 0. \qquad (2.17)$$

After integration and rearrangement, the $[Acid]$ has the following dependence on dose during exposure

$$\frac{[Acid]}{[A]} = \frac{\sigma_1 \cdot \sigma_2 \cdot \left(\int_{pulse} I \cdot dt\right)^2}{\frac{t_f}{\tau_1} + \sigma_2 \cdot \int_{pulse} I \cdot dt}, \qquad (2.18)$$

where t_f is the pulse cycle time (inverse of the laser repetition rate) and the integral represents the dose delivered. An examination of Equation 2.18 reveals that higher reaction orders between 1.0 and 2.0 can be achieved if the parameters in the denominator are tuned such that the t_f/τ_1 term dominates over the dose dependent term. Although ISTP materials do not exhibit true two-photon behavior, they may require significantly lower doses to generate acid compared to two-photon resists. The trade off between lower reaction orders may be offset by the lower doses.

The behavior of ISTP materials depends on the ability of the intermediate species to revert to the initial state or possibly decay to another species. A build up of the intermediate species will effectively render the sequence to become a first ordered reaction that is controlled by a rate limiting step. Therefore, the characteristics of the exposing laser such as the energy per unit area delivered by each pulse ($A0$), pulse cycle time (t_f), and full width half max (FWHM) also have to be considered.

2.5.4 Optical Threshold Materials

Optical threshold layers (OTLs) are materials that require the absorption of a threshold exposure dose to induce a photochemical event. The exposure threshold gives the material a region of nonlinear response to exposure dose and allows OTLs to be used as double-exposure resists. Nonlinearity derives from the fact that any dose absorbed below the threshold does not cause reactions to occur. Upon reaching the threshold dose, the threshold photochemical response occurs. To prevent a quencher-like response which does not provide the necessary nonlinearity behavior for DEL (only provides a dose offset), the threshold response is not further impacted by additional dose above the threshold dose. The ideal binary step change behavior is more clearly described by the following simple piecewise function

$$f(I) = \begin{cases} \text{Threshold Response} & , \quad E_{Actual} \geq E_{th} \\ \text{No Response} & , \quad E_{Actual} < E_{th} \end{cases} \tag{2.19}$$

$$\text{where } E_{Actual} = \int_{pulses} I \cdot dt,$$

E_{Actual} and E_{th} represent the actual dose received by the material and the threshold dose, respectively.

Analogous thermal resist systems are already in use in the printing industry [20]. Thermal resists rely upon a thermal image instead of an optical image. The thermal image is derived from the absorbance of high intensity light images. Thermal resists use the absorbed thermal energy to induce a phase change in the system and cause the solubility switch as opposed to traditional chemical resists which use the energy to carry out a chemical reaction. Phase changes are ideal as the dose dependent mechanisms in OTL materials because the threshold response is inherently built into the thermodynamics of the system. For example, in the solid to liquid transition of water, the thermal dose required to melt the ice is the sum of the energy required to bring the water from the initial temperature to the melting temperature and the latent heat of fusion. Below the threshold dose, the transition does not occur. The system also does not have any memory effects to the thermal dose as the thermal dose required for melting per unit mass at a given initial temperature remains constant even after multiple heating and cooling cycles.

Chapman et al. have investigated inorganic thermal resist systems [10] that use Bi/In bilayers as an etch masking layer for silicon. However, the use of Bi and In metals are not compatible with the photolithography process as the target semiconductor devices are very susceptible to metal contamination. Chemical systems with similar properties for optical images have to be developed to use this technology with lithographic imaging systems.

Analogous chemical systems will most likely also need to use the optical image to induce a phase change in the material which will then allow a solubility switch. The phase change will replicate the behavior of thermal resists in that the absorption of a threshold dose is required to induce phase change. Below the threshold, no solubility switch should occur and the material should not have resist memory.

2.6 Conclusions

According to the Raleigh criteria, the minimum achievable feature size with current state-of-the-art technologies is approximately 38 nm. Doubling the number of exposure passes has the possibility of extending the current technology below the threshold and, specifically for the DEL case, is very attractive because of the potential low cost of ownership. However, the proposed DEL process is not possible with conventional resists due to “resist memory”. This chapter presented several potential materials with nonlinear response to exposure dose. The feasibility of using these materials is discussed in the next chapter.

Chapter 3

Feasibility Studies of the Potential Materials through Simulation

3.1 Introduction

Several material types were presented in the previous chapter that in theory would have the necessary nonlinear response to exposure dose required for the DEL process. These materials are not the only possibilities, but they do provide a reasonable range of resist designs to explore the feasibility of DEL as a technology choice. Of the proposed materials, only CELs and two-photon materials have been extensively studied and have established chemical systems. ISTP and OTL materials do not currently exist for use in semiconductor applications. However, their theoretical mechanisms are considered to test their viability as a possible DEL candidates. Feasibility studies were performed through simulation to evaluate which DEL materials had the most promise. The results of the studies are presented in this chapter and were used to guide our materials development effort.

3.2 Simulation Setup

3.2.1 Software

The performance of the different material types in double-exposure mode and the dependence on their material properties were evaluated by computer simulation using a combination of the commercially available PROLITH V9.3 lithography simulator from KLA-Tencor and custom code. For simplicity, this chapter is mainly devoted to the discussion of the feasibility studies. The details of the simulator including the discussion of the custom code and its integration with PROLITH is presented in Chapter 5.

3.2.2 Imaging Setup

In all cases, the optical imaging portion was performed with PROLITH. A half pitch CD of 25 nm was targeted using a 1.2 NA water immersion exposure system in double-exposure mode. This is an effective k_1 of 0.155. An azimuthally polarized cross-quadrupole with $\sigma_{center} = 0.8$ and $\sigma_{radius} = 0.15$ was used as the illuminator. Different masks were used for each of the two exposure passes. The masks were 50 nm line/space phase shift masks with 6 % transmission. The two masks were offset by 50 nm between exposure passes. As described previously [8], DEL with positive tone resists is a trench-based process as opposed to the line-based process expected with a single exposure pass. Consequently, the target line is expected to form at the interface of the opaque and bright regions as opposed to the center of the bright regions. A focus-exposure matrix was run for each material system.

3.2.3 Film Stack and Base Resist System

The film stack consisted of 50 nm of resist on 31 nm of a single layer of bottom anti-reflective coating (BARC) (n = 1.82, k = 0.46). The substrate was silicon with a 2 nm layer of SiO_2. The filmstack is represented in Figure 3.1.

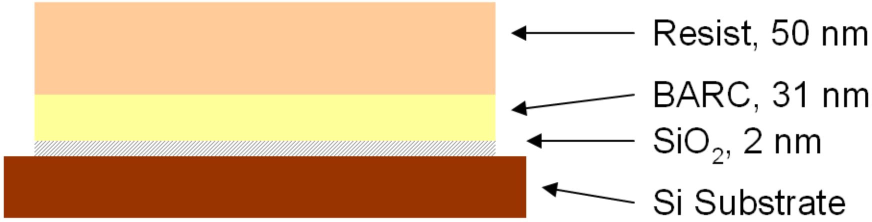

Figure 3.1: Schematic of the filmstack used in the simulation.

The resist simulations were based upon a typical 193 nm resist system. The base resist parameters are shown in Table 3.1. In the case of the OTL and ISTP materials, the acid generation behavior differs from the base resist and was described with custom models.

3.2.4 Reversible CEL Simulation Parameters

To study the CEL behavior, a 50 nm CEL was applied on top of the film stack. The material response of the reversible CEL was studied using the PROLITH simulator. The Dill A parameter was varied from 10 μm^{-1} to 50 μm^{-1}. The CEL parameters are shown in Table 3.2. Since a reversible CEL system provides better performance than an irreversible system, the rCEL was selected for the study.

Table 3.1: Parameters used for the base resist system.

Property	Value
Resist Refractive Index, n	1.70
Resist Dill A (μm^{-1})	0
Resist Dill B (μm^{-1})	1.47
Resist Dill C (cm^2/mJ)	0.0478
Relative Quencher Concentration, [Q]/[PAG]	0.2
Development Model	Original Mack Model
Development Rmax (nm/s)	100
Development Rmin (nm/s)	0.1
Threshold Inhibitor Concentration, M_{th}	0.75
Dissolution Selectivity Parameter n	25.0
Acid Diffusivity, $\mathrm{D_H}$ (nm^2/s)	0.223
Quencher Diffusivity, $\mathrm{D_Q}$ (nm^2/s)	0.0
Amplification Reaction Rate Constant, $\mathrm{k_a}$ (1/s)	0.100
Acid Base Quenching Rate Constant, $\mathrm{k_b}$ (1/s)	4.85×10^8
Development Time (s)	20

Table 3.2: Simulation parameters used for the reversible CEL material.

Parameter	Value
rCEL Refractive Index, n	1.69
rCEL Dill A (μm^{-1})	$0 - 50$
rCEL Dill B (μm^{-1})	0
rCEL Dill C (cm^2/mJ)	0.11

3.2.5 ISTP Simulation Parameters

To study the performance of the ISTP material, the acid generation behavior described in the previous section was solved using a 4th order Runge-Kutta method [11]. Please refer to Section 5.3 for more details. The parameters and values used in the simulation are listed in Table 3.3. To simplify the calculations, τ_2 was assumed to be very large such that the conversion of the intermediate species to acid is assumed to be irreversible.

Table 3.3: Simulation parameters used for the ISTP material.

Parameter	Value
σ_1 (cm^2/mJ)	0.235
σ_2 (cm^2/mJ)	0.235
τ_1 (s)	0.006
t_f (s)	0.00025
$A0$ (mJ/cm^2)	0.05
ϕ	1
FWHM (ns)	20

3.2.6 OTL Simulation Parameters

The behavior of an ideal OTL material is shown in Equation 2.19. The parameters and values used in the simulation are listed in Table 3.4. As mentioned, OTL materials were simulated with custom models which are described in more detail in Section 5.4.

Table 3.4: Simulation parameters used for the OTL material.

Parameter	Value
E_{th} (mJ/cm^2)	10
$[PAC]_{th}$	0.75

3.3 Results and Discussion

All three materials yielded nonlinear resist response when used in double-exposure mode. The resist profiles are shown in Figure 3.2 to Figure 3.4 and summarized in Table 3.5.

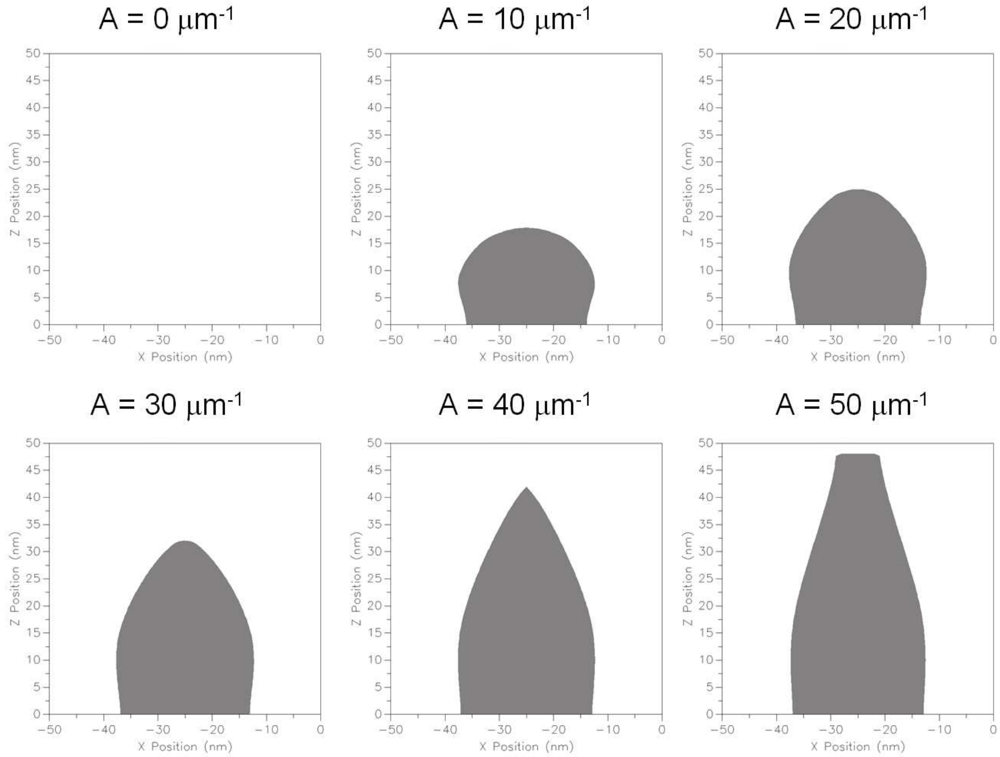

Figure 3.2: Resist profile of rCEL with varying Dill A parameter.

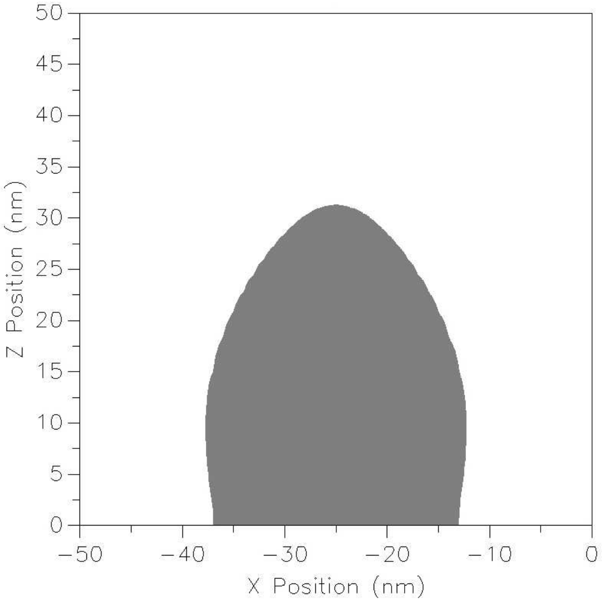

Figure 3.3: Resist Profile for ISTP material.

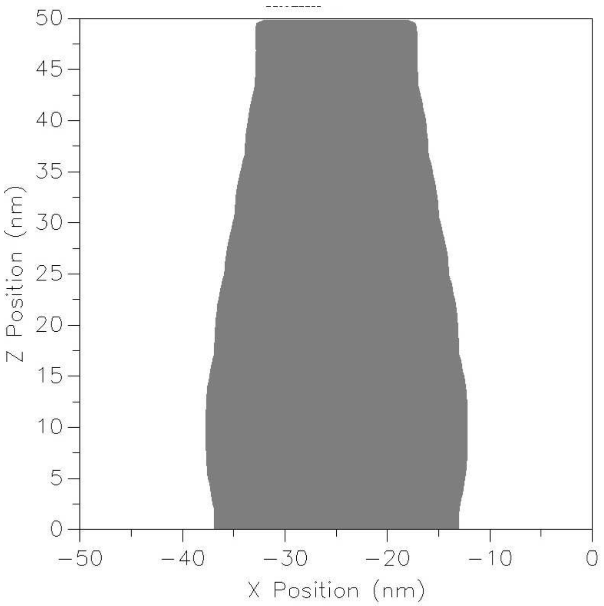

Figure 3.4: Resist Profile for OTL material.

Table 3.5: Summary of resist profile metrology.

Material	Dose (mJ/cm^2)	Sidewall Angle (°)	Resist Loss (nm)
rCEL A = 10 μm^{-1}	25	75	32
rCEL A = 20 μm^{-1}	38	74	25
rCEL A = 30 μm^{-1}	56	71	18
rCEL A = 40 μm^{-1}	80	70	8.1
rCEL A = 50 μm^{-1}	110	75	2.0
ISTP	37	72	19
OTL	39	82	0.18

The simulation results from the focus-exposure experiments were analyzed using commercially available ProDATA V1.4.3 from KLA-Tencor to generate simulated Bossung plots and exposure latitude (EL) versus depth of focus (DOF) plots. The results are shown in Figure 3.5 to Figure 3.7 and are summarized in Table 3.6. Simulated EL versus DOF plots with respect to the different Dill A parameters are shown in Figure 3.8.

Table 3.6: Summary of the process windows for the rCEL, ISTP and OTL materials.

Material	Depth of Focus (μm)	Exposure Latitude (%)
rCEL	0.11	0.58
ISTP	0.12	3.2
OTL	0.14	5.1

It is important to note that CD was the only output metric considered in the process window calculations. In most manufacturing environments, other parameters such as sidewall angle and resist loss would also need to be optimized to produce functional devices. However, the main goal of this work is

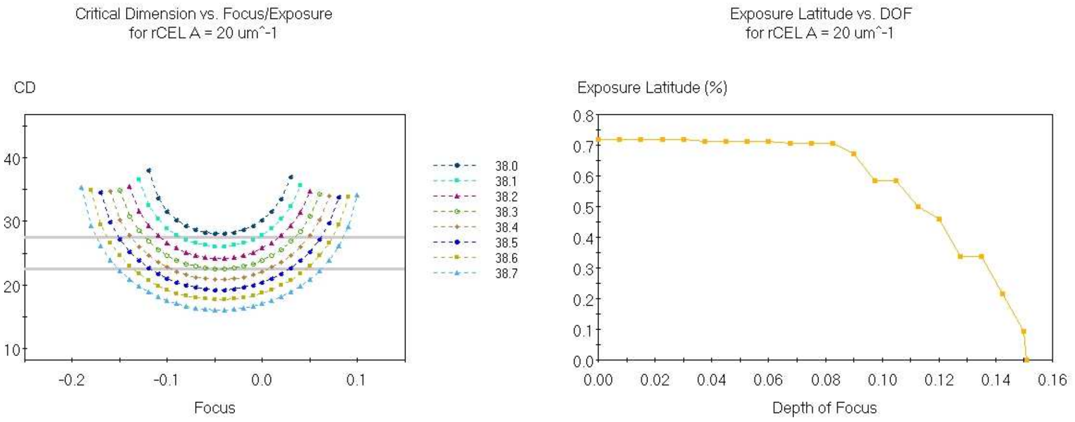

Figure 3.5: Simulated Bossung plot with varying exposure dose (Units: CD (nm), Focus (μm), Exposure Dose (mJ/cm^2)) and EL versus DOF (μm) for rCEL material.

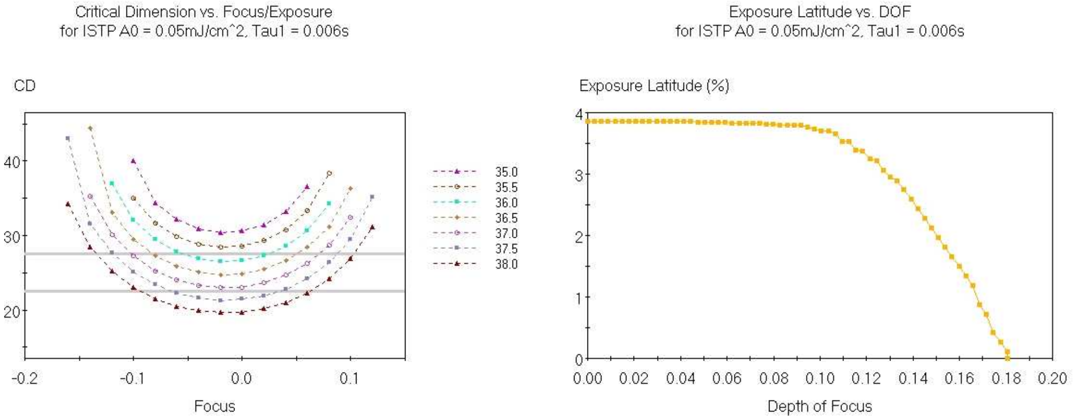

Figure 3.6: Simulated Bossung plot with varying exposure dose (Units: CD (nm), Focus (μm), Exposure Dose (mJ/cm^2)) and EL versus DOF (μm) for ISTP material.

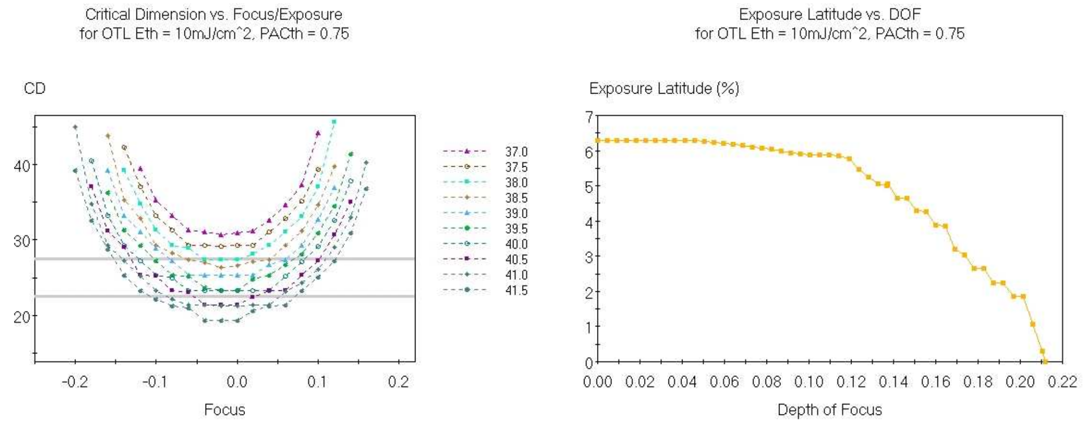

Figure 3.7: Simulated Bossung plot with varying exposure dose (Units: CD (nm), Focus (μm), Exposure Dose (mJ/cm^2)) and EL versus DOF (μm) for OTL material.

to demonstrate the proof of concept of the theoretical materials. Optimization of such parameters is beyond the scope of this study.

Figure 3.2 shows the effects of the Dill A parameter on the resist profile. For the test case of a Dill A parameter of 0 μm^{-1}, no resist profile was observed. This finding is consistent with the behavior of conventional resists since with a Dill A parameter of 0 μm^{-1} the effect of the CEL disappears.

In all cases, increasing the Dill A parameter decreased resist loss and improved the shape of the resulting image. Figure 3.8 shows that the process window was also widened with the increase. Increasing the Dill A parameter showed improvement for EL. However, only marginal improvement was observed for the DOF. Increasing the Dill A parameter also led to increases in the dose requirement. An increase in the Dill A parameter from 10 μm^{-1} to

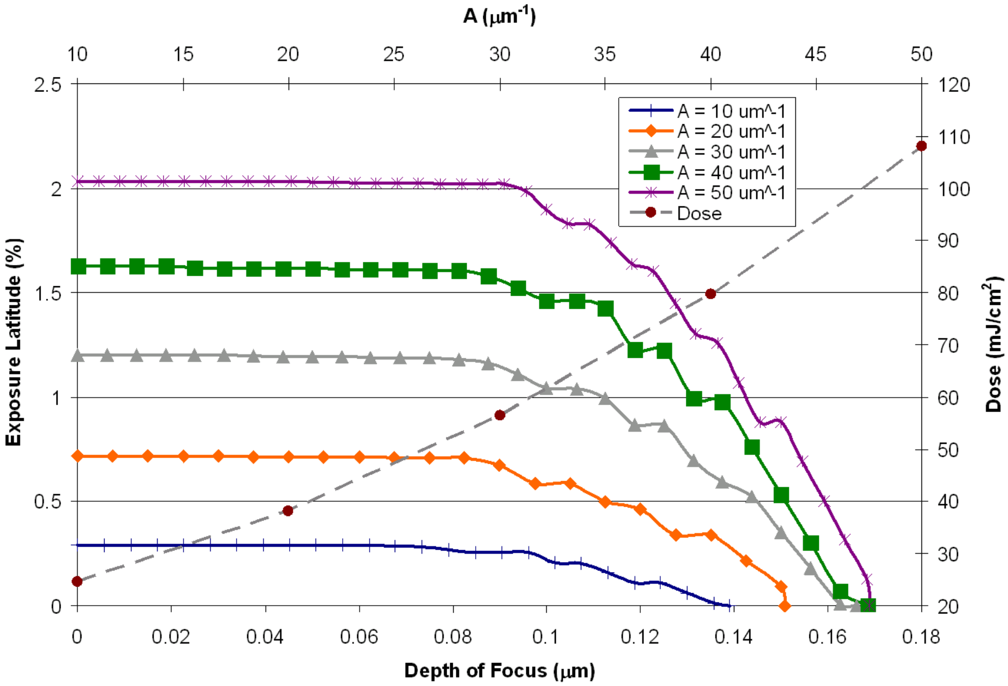

Figure 3.8: Process windows of rCEL materials varying the Dill A parameter.

50 μm^{-1} required approximately 4.4 fold increase in dose. Another factor to consider is the feasibility of obtaining rCEL materials with high Dill A values. Without increasing the Dill A parameter, it is theoretically possible to increase the absorbance of the rCEL layer by increasing the layer thickness. However, the oblique incident angles resulting from operating at NA values greater than 1 may lead to loss in depth of focus if the layer becomes too thick. rCEL materials showed nonlinear behavior in DEL mode, however, image quality and process window improvement was only observed for rCELs with very high Dill A parameters (> 30 μm^{-1}). Even if physical analogs with such high Dill A parameters are obtainable, the improvements are marginal and come at the cost of large dose increases.

Table 3.5 shows that an rCEL with Dill A parameter of 20 μm^{-1} has a comparable dose requirement to that of ISTP and OTL materials. Results from this run were used for subsequent comparisons with ISTP and OTL materials.

Figure 3.3 shows the resist profile of the ISTP material. The profile is comparable to rCEL having slightly lower sidewall angle, 72 $^{\circ}$, and reduced resist loss, 19 nm. Table 3.6 shows that ISTP has a larger process window than rCEL. The parameters of interest affecting the nonlinear acid generation behavior of the material are the energy per unit area delivered by each pulse, A0, and the reversible rate constant of the intermediate state, $1/\tau_1$. For a given set of laser parameters, large values of A0 or τ_1 lead to faster conversion of PAC thus reducing the required exposure dose. However, the dose reduction also leads to a decrease in nonlinearity. Since the laser can only deliver integer numbers of pulses, the magnitude of A0 has to be within a manageable increment such that small deviations in the pulse delivery will not drastically affect the CD. The parameters had to be optimized so that the system will retain nonlinear behavior but at the same time yield features within reasonable exposure dose ranges.

Figure 3.9 shows the effects of varying A0 and τ_1 on the PAC conversion after a target dose of 30 mJ/cm^2 at a relative intensity of 0.3 was delivered. As expected, increases in A0 or τ_1 both resulted in faster conversion of [PAC]. For the simulation setup, a [PAC] of 0.8 is desired. Figure 3.9 shows that this is achievable with all of the A0 values from 0.01 to 0.05 mJ/cm^2−pulse. However, A0 values greater than 0.1 mJ/cm^2−pulse lead to difficulties in dose deviation management and τ_1 values for reasonable chemical systems has an upper limit in the millisecond range. Consequently, A0 and τ_1 values of 0.05 mJ/cm^2 and 0.006 s were selected, respectively. ISTP materials showed a larger process window and improved resist profile than rCEL, and could be a potential DEL material provided that materials with the specified kinetics and time constants can be identified.

Figure 3.4 shows the resist profile of the OTL material. The profile shows a significant reduction in resist loss compared to both rCEL and ISTP resist profiles and slight improvement in the sidewall angle. The OTL material also has the largest process window of the three materials investigated. The threshold dose requirement behavior of the OTL material served effectively

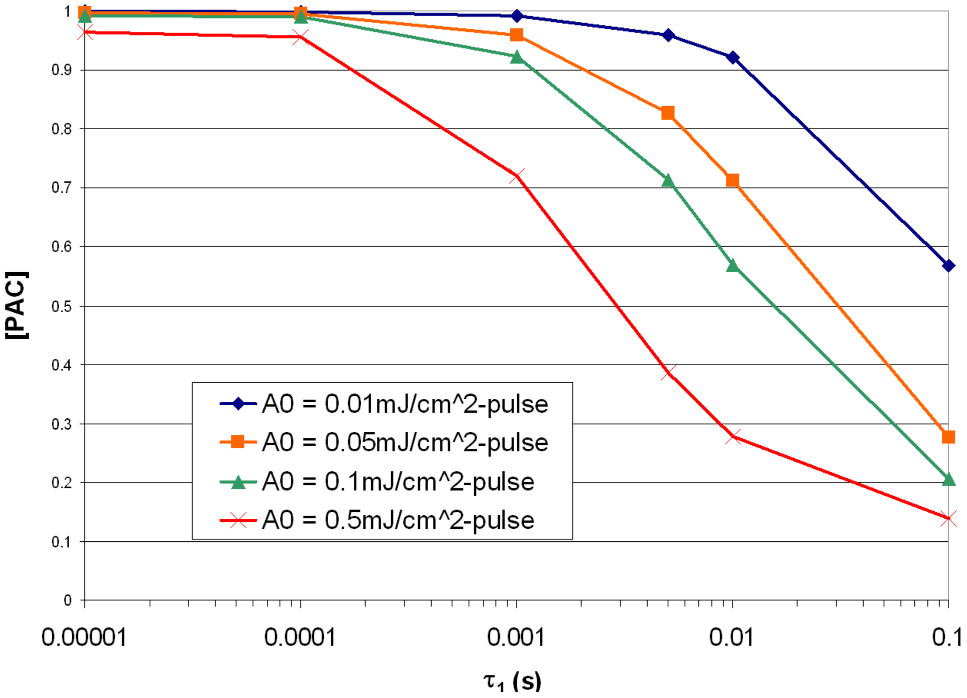

Figure 3.9: Effect of A0 and τ_1 on the PAC conversion after a target dose of 30 mJ/cm^2 assuming pulse delivery rate at 30% relative intensity of A0.

to filter out regions of low intensity. In addition, the threshold conversion response of the PAC resulted in improved image contrast. Because no such physical systems exist, the threshold dose, E_{th}, and PAC conversion, $[PAC]_{th}$, were chosen such that they would provide a defined solubility switch within comparable dose ranges. Hypothetical OTL materials showed the best performance (i.e. largest process window and best resist profile) compared to rCEL and ISTP materials and could enable DEL. This conclusion serves as motivation for research directed toward development of such materials.

3.4 Conclusions

DEL offers several advantages over DPL, but it requires new materials with nonlinear dose response. We have employed simulations to explore several potential DEL material options. The modeling results show that two-photon materials will not be feasible unless achievable laser peak power in exposure tools can be significantly increased. rCEL materials demonstrated nonlinear behavior in DEL mode, however, image quality and process window improvement was only observed for rCELs with very high Dill A parameters ($> 30\ \mu\text{m}^{-1}$). Even if physical analogs with such high Dill A parameters are obtainable, the improvements are marginal. ISTP materials showed a larger process window than rCEL. The challenges with this approach are identifying materials with the specified kinetics and the ability to tune the time constants. OTL materials showed the best performance with the largest process window and best resist profile. There are no physically functional optical analogs with the required thresholding behavior. Potential mechanisms, either chemical or physical, need to be explored. From our feasibility studies, we believe that the hypothetical ISTP and OTL materials have the greatest potential for use in DEL applications and warrant our investment in materials development.

Chapter 4

Feasibility Studies II: Evaluation with Enhanced Imaging Conditions

4.1 Introduction

The feasibility studies discussed in Chapter 3 provided the first insight into how the different proposed DEL materials would perform when used in DEL mode. The simulation conditions used for the study were selected based on perceived industry manufacturable standards. As it was difficult to ascertain the actual operating conditions due to the proprietary nature most industrial processes, the goal was to select a set of attainable conditions that have the widest range of applicability. The results from the study were essential in guiding the materials development efforts. As a follow up study, several of the key simulation conditions were further optimized to evaluate the extent of improvement on material performance, if any, and the validity of previous conclusions.

4.2 Optimization of Imaging Conditions

The results from the study described in Chapter 3 served as a base case for evaluating the materials. Several approaches are available to further optimize the simulation conditions such as improving the imaging conditions, reducing the acid diffusion length, or finding better development conditions. But above all else, the optimization of imaging conditions has the most relevance for DEL materials because the goal of these materials is to enhance the imaging capabilities of existing processes. The effects of several improvements are described below.

4.2.1 Illuminator Shape

The shape and placement of the illuminator are important factors in generating the correct diffraction pattern for the aerial image. The illuminator shape used in the base case was an azimuthally polarized cross-quadrupole with $\sigma_{center} = 0.8$ and $\sigma_{radius} = 0.15$. Although a dipole illuminator aligned perpendicularly to the direction of the lines and spaces produces a better image, a cross-quadrupole illuminator was selected to be a more practical illuminator that can be used to image features other than alternating lines and spaces. To test the improvements in performance that result from using a dipole illuminator, the illuminator was changed to a dipole shape with $\sigma_{center} = 0.8$ and $\sigma_{radius} = 0.15$. A graphical representation of the illuminators are shown in Figure 4.1.

4.2.2 Matched Substrate

An important task in constructing a resist filmstack is the minimization of reflections from the underlying substrate. Spurious reflections can cause

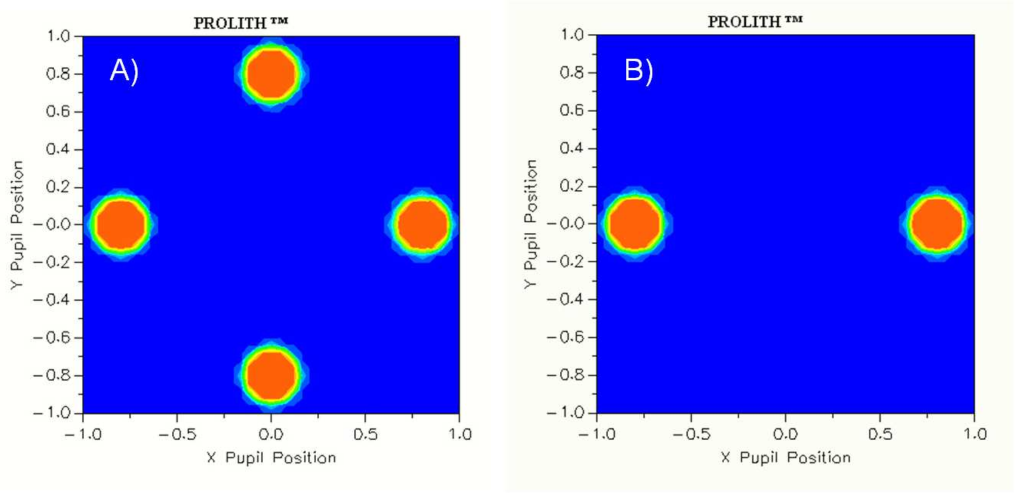

Figure 4.1: Schematic of the illuminators. A) Cross-quadrupole illuminator used in the base case study. B) Dipole illuminator used in the imaging optimization study.

problems such as standing waves and flare that degrade the image quality in the resist. These reflections can be minimized by the use of bottom anti-reflective coatings (BARCs) between the resist and substrate. Although, the resist stack used in the base case study was optimized with a BARC to minimize substrate reflections, the reflections were not completely eliminated. The ideal condition would be the use of an infinite 'matched substrate' where the optical properties of the substrate (n and k) are exactly matched to the resist such that substrate reflections are completely eliminated. The use of a matched substrate was investigated.

4.2.3 Mask Feature Resize

The masks used in the base case study were 50 nm line/space attenuated phase shift masks with 6 % transmission. These masks were offest by half-pitch between exposure passes. Pictorial representations of the masks and corresponding aerial images are shown in Figure 4.2. It was suggested that in some cases the imaging could be improved by slightly adjusting the dimen-

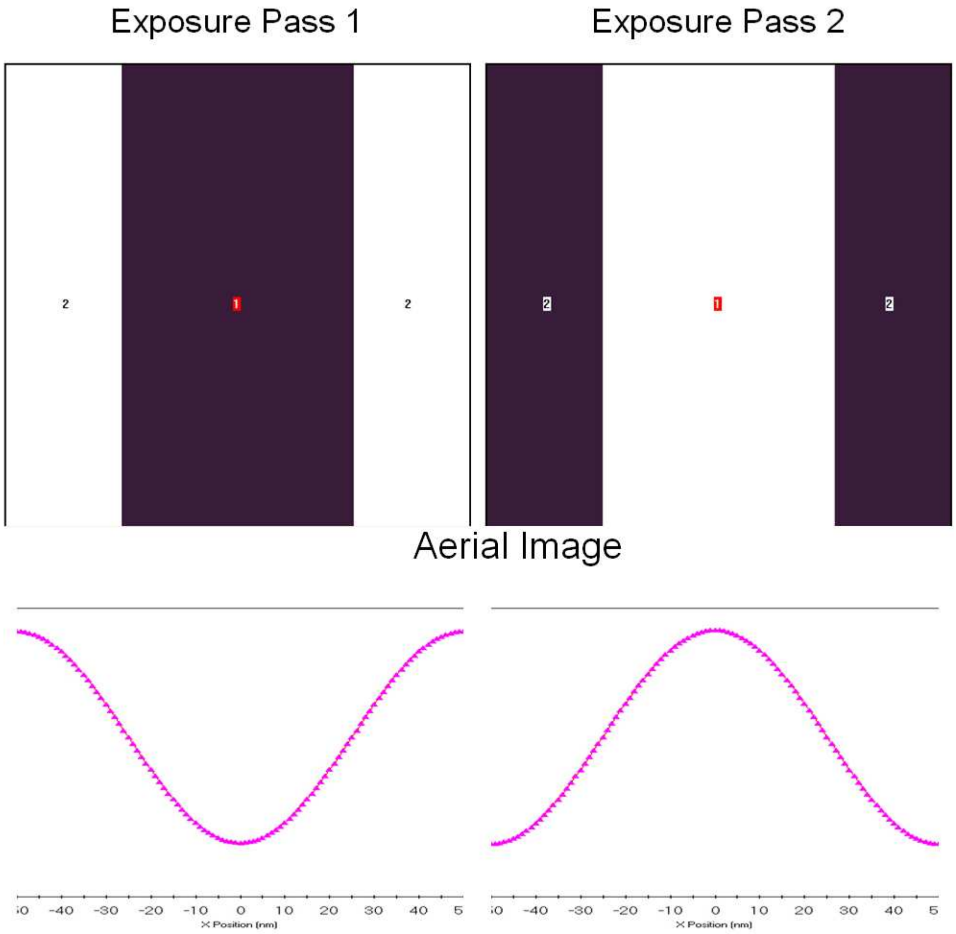

Figure 4.2: Schematic of the masks and corresponding aerial images.

sions of the lines and spaces. The line to space resizing was investigated by increasing the line width to 55 nm and space width to 45 nm.

4.3 Case Study with the rCEL

The feasibility study showed that the rCEL had the poorest performance of the materials. This material was selected to test the imaging optimizations described above. An additional improvement was studied with the rCEL. The rCEL thickness was increased from 50 nm to 125 nm. The results from A = 20 μm^{-1} was used as the base case for comparison. The optimizations were first implemented individually and then in combination. All other experimental conditions were as described in Section 3.2.

4.3.1 Results and Discussion

All of the imaging optimizations yielded nonlinear resist response when used in double-exposure mode. The resist profiles for the individual improvements are shown in Figure 4.3 and the combined improvements are shown in Figure 4.4. The results are summarized in Table 4.1. Figure 4.3 shows the effects of the various imaging improvements on the resist profile. In all cases, the imaging optimizations also lead to improvements in the exposure latitude. However, almost no improvement in the DOF was observed.

When the optimizations were only applied individually, the largest improvement in the shape of the resist profile was observed in the optimization where the rCEL thickness was increased to 125 nm. The resist loss decreased

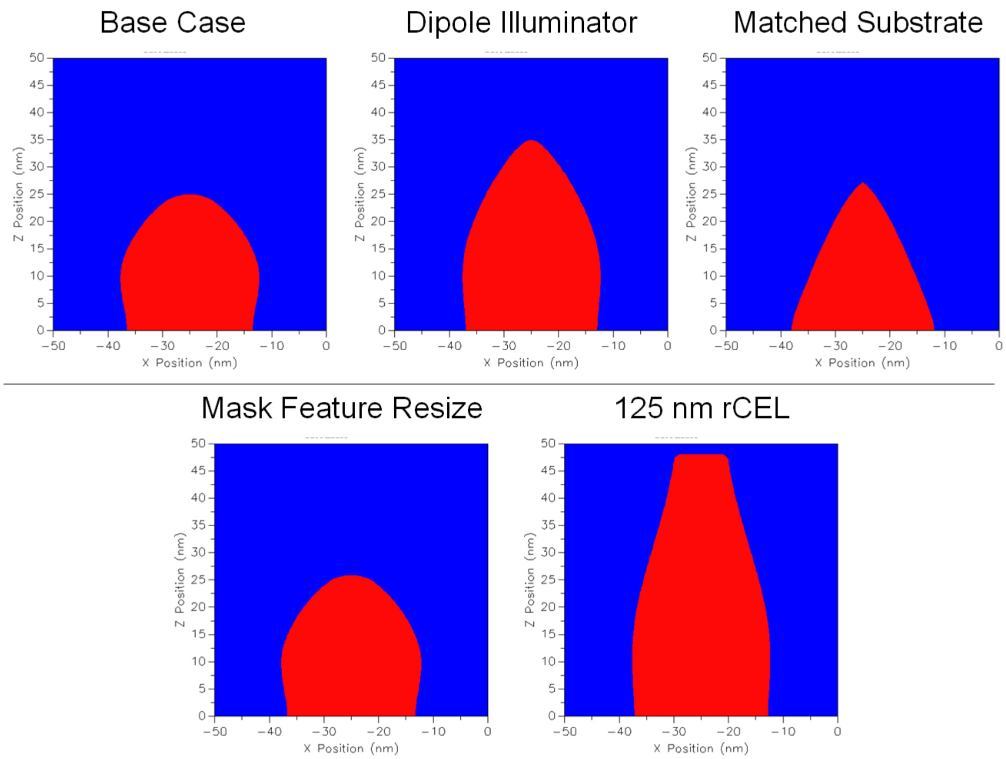

Figure 4.3: Resist profile of rCEL material with varying imaging improvements.

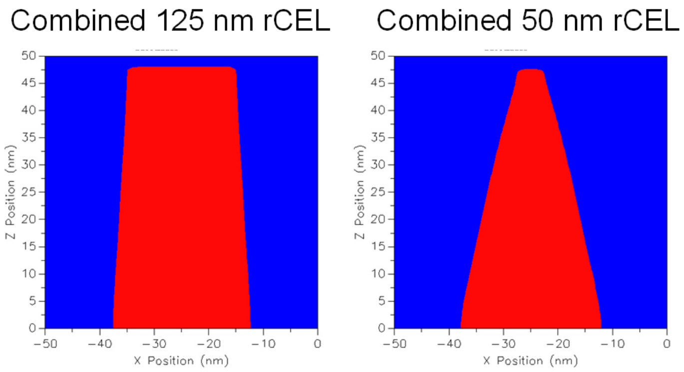

Figure 4.4: Resist profile for rCEL material with combined imaging improvements.

Table 4.1: Summary of resist profile metrology and process window with different applications of imaging improvements.

Imaging Improvement	Dose (mJ/cm^2)	SA (°)	RL (nm)	DOF (μm)	EL (%)
Base Case (A = 20 μm^{-1})	38	74	25	0.11	0.58
Dipole Illuminator	27	71	15	0.11	1.3
Matched Substrate	38	66	23	0.11	0.71
Mask Feature Resize	48	73	24	0.11	0.64
125 nm rCEL	120	77	2	0.12	1.8
Combined 125 nm rCEL	95	86	2	0.12	2.7
Combined 50 nm rCEL	32	77	2	0.11	1.4

from 25 nm to 2 nm compared to the base case. The resist profile was also more rectangular. However, this improvement was accompanied by a four fold increase in exposure dose. This increase in dose was not surprising as increasing the rCEL thickness increased the amount of absorbing material. The observed dose and metrology results are very similar to the case where Dill A = 50 μm^{-1} from the feasibility studies shown in Table 3.5. It is postulated that the similarity is due to the same increase in effective absorbance of the rCEL layer. In the previous case, the Dill A parameter was increased by a factor of 2.5 from 20 μm^{-1} to 50 μm^{-1}, and in the latter, the thickness was increased by a factor of 2.5 from 50 nm to 125 nm.

The next best performing imaging optimization was observed when the illuminator was changed from cross-quadrupole to dipole. The resist loss reduced from 25 nm to 15 nm. Although the resist loss was less than the use of a thicker rCEL, the use of the dipole illuminator produced images at much lower doses. The exposure latitude increased from 0.58 % to 1.3 %.

Finally, Figure 4.3 showed that the use of a matched substrate and mask feature resize resulted in marginal improvements. Using a matched substrate slightly reduced the resist loss (23 nm) and improved the exposure latitude (0.71 %), but also reduced the sidewall angle (66 °). The resist profile actually resembles a triangle in shape. A more rectangular shape would be more desirable for etching. The resist profile for the mask feature resize case was essentially identical to the base case, but the exposure dose increased from 38 mJ/cm^2 to 48 mJ/cm^2.

Figure 4.4A shows the resist profiles when the imaging optimizations were combined. A separate trial, where the rCEL thickness was kept at 50 nm, was also performed and shown in Figure 4.4B. In both cases, significant reductions in resist loss was observed compared to the base case. The resist loss was decreased to 2 nm for both cases. The resist profile for the total combined case was much more rectangular than the case where 50 nm rCEL was used. This is expected as the use of the thicker rCEL had the most impact in the individual trials. Similar to the individual case, the exposure dose also increased, but only approximately by a factor of 2. Using only a 50 nm rCEL saw a reduction in the exposure dose but resulted in a much more triangular resist profile. However, the concerns regarding the availability of organic materials with high Dill A values still remain and the increase in exposure time is very significant.

4.3.2 Summary for the Case Study with rCEL

The results from the rCEL case study show that the base case study could be improved with various imaging optimizations. Specifically, increasing the rCEL thickness had the most effect. But similar to the increasing the Dill A in the base case study, this improvement was achieved at the expense of sacrificing exposure dose which translates to loss in throughput. Switching from a cross-quadrupole illuminator to dipole was a more acceptable improvement. However, additional patterning steps may be required to image other features that are not suitable to be patterned by a dipole illuminator. The results presented in this section demonstrated the improvements in the rCEL material. The next section completes the imaging enhancement study by applying the optimizations to the ISTP and OTL materials.

4.4 Imaging Optimization Study with ISTP and OTL Materials

The imaging optimizations applied to the rCEL material was also applied to the ISTP and OTL materials. The rCEL case study demonstrated the effects of each optimization when applied individually. It is expected that the trend would be similar for the ISTP and OTL materials. Since the combined case showed the most improvement, only the combined case was applied. Of course, increasing the rCEL thickness did not apply to these materials and were not included. The results from the study are shown in Figures 4.5 and 4.6, and summarized in Table 4.2. Results from the previous feasibility study were used as the base cases for comparison.

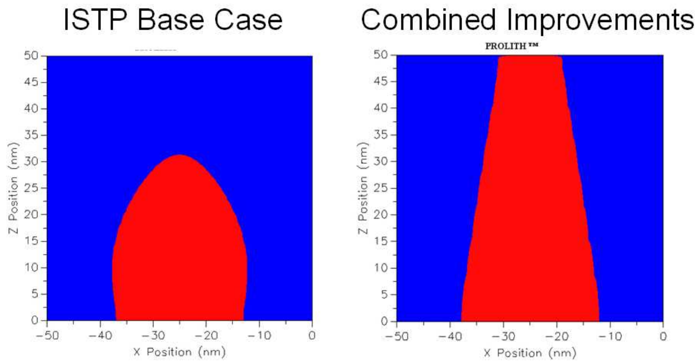

Figure 4.5: Resist Profile for ISTP material.

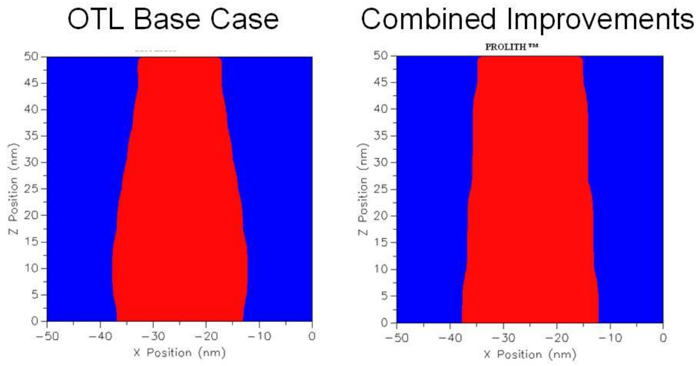

Figure 4.6: Resist Profile for OTL material.

Similar to the rCEL case study, Figures 4.5 and 4.6 show that improvements to the resist profile were observed with the use of the imaging optimizations. The improvement in the resist profile was more pronounced for the ISTP material as opposed to the OTL. The resist loss reduced from 19 nm to 0.20 nm compared to the base case. The sidewall angle improved from 72 °

Table 4.2: Summary of resist profile metrology and process window with imaging optimizations for ISTP and OTL materials.

Imaging Improvement	Dose (mJ/cm^2)	SA (^{o})	RL (nm)	DOF (μm)	EL (%)
ISTP Base Case	37	72	19	0.12	3.2
Combined ISTP	22	81	0.20	0.13	5.0
OTL Base Case	39	82	0.18	0.14	5.1
Combined OTL	30	87	0.19	0.15	6.2
Combined 125 nm rCEL	95	86	2	0.12	2.7
Combined 50 nm rCEL	32	77	2	0.11	1.4

to 81 ^{o} and the exposure dose was reduced from 37 to 22 mJ/cm^2. The resist profile was more trapezoidal in shape.

The improvements in the OTL material were not as evident, but this may be due to the fact that the resist profile for the OTL material was already much improved compared to the other materials. For example, the resist loss actually increased from 0.18 nm to 0.19 nm, both of which are negligible ($<$ 0.5 % loss). The sidewall angle improved from 82 ^{o} to 87 ^{o} and the exposure dose was reduced from 39 to 30 mJ/cm^2.

As with the rCEL case study, the EL also increased for both materials, but no significant improvement was observed in the DOF. The ISTP material had an 1.8 % increase in EL while the OTL material had an 1.1 & increase. These results suggest that, as in the case of the rCEL, optimizing the imaging conditions also improved the results for the ISTP and OTL materials. When comparing the results amongst all three materials, however, it is clear that the best performing rCEL run (combined, rCEL = 125 nm) was at best only marginally better than the base cases of the ISTP and OTL materials (improved resist loss over the ISTP base case), but requires at least double the dose of the ISTP and OTL materials. When the combined optimizations are applied, ISTP and OTL materials outperform the rCEL. This final comparison reaffirms the previous conclusion from Chapter 3 that the ISTP and OTL materials show more promise as possible DEL materials.

4.5 Conclusions

The feasibility study performed in Chapter 3 provided useful results that guided the material development efforts. To complete the feasibility study, several of the imaging conditions were further optimized to evaluate how the materials would perform under more ideal conditions. As expected, optimizing the imaging conditions improved the resulting material performance in all cases. In a rCEL case study, it was determined that changing the illuminator from cross-quadrupole to dipole and increasing the rCEL thickness resulted in the largest improvements for line and space patterns. The improvements with respect to the base cases were significantly more pronounced for the rCEL and ISTP materials compared to the OTL material. However, the improvements in the rCEL material were only marginally better than the base cases for the ISTP and OTL material. This result further confirmed the conclusion from the the previous feasibility studies and the decision to pursue development of the ISTP and OTL materials.

Chapter 5

Custom Double-Exposure Lithography Simulator

5.1 Introduction

The results from the feasibility studies were useful in determining the direction for materials development. As most of the proposed material types are only conceptual, no existing software package was readily available to evaluate the performance of the materials. Thus, a custom DEL simulator was implemented using a combination of commercially available software packages and custom algorithms. This chapter details the development of the simulator including the custom algorithms and integration process.

5.2 Existing Software as a Launching Pad

The main goal of the project was to identify materials that will enable DEL for the semiconductor industry. In order to ensure its maximum impact, this goal should be achieved before the switch to the next production node (targeted half-pitch CD for flash memory is 32 nm by 2011 [17]). With the time frame in mind, the approach to the feasibility studies was to first explore available software packages such as the PROLITH simulator.

PROLITH is an industry recognized software for simulating the unit operations of the semiconductor fabrication process from the initial lithographic imaging step to the final etch. It has sophisticated physical and empirical models to describe the exposure optics, resist response during exposure, and resist development. These capabilities suggest that PROLITH was a good starting platform. But as of version 9.3, the software has limited capabilities in simulating the DEL process. It is only capable of simulating double exposure of reversible CELs. Furthermore, it is not able to simulate the behaviors of ISTP and OTL materials, but this is mainly due to the fact that these materials do not yet exist. Although PROLITH provides a good starting point, further modeling was required to complete the DEL simulator. To fully study the ISTP and OTL materials, custom modules were developed (using C++ and MATLAB) to model the material behaviors.

5.3 Modeling the ISTP Material Response

The acid generation behavior of the ISTP material was described in a Section 2.5.3. Contrary to most resist materials where only the resulting sum dose per exposure pass is important in determining acid generation, the acid generation of the ISTP system is dynamically dependent on the characteristics of the exposure light intensity profile as a function of time. Solving for the acid generation requires simultaneous solution of the kinetic equations in Equation 2.15 and a description of the light intensity profile.

For most modern exposure tools, an excimer pulsed laser is used as the exposure light source. The pulsed light output can be approximated as a Gaussian beam. The intensity of the beam has the following dependence with respect to time

$$I = A0 \cdot \frac{2 \cdot \sqrt{\ln 2}}{FWHM \cdot \sqrt{\pi}} \cdot \exp\left[-4 \cdot \ln 2 \cdot \left(\frac{t - t_0}{FWHM}\right)\right], \tag{5.1}$$

where $A0$ is the energy per unit area delivered by each pulse, $FWHM$ is the full width half max of the beam, and t_0 is the time offset for the peak output. The t_0 parameter was introduced to provided some padding around the Gaussian pulse profile such that the profile is included within a single laser pulse as opposed to having the peak centered at $t = 0$. The specifications for a typical laser is shown in Table 5.1. The parameter t_f represents the cycle time per laser pulse and is the inverse of the repetition rate. Using the parameters listed in Table 5.1 and $t_0 = 3 \times FWHM$, a graphical representation of the beam profile was generated and is shown in Figure 5.1. Figure 5.1A shows a snapshot of a single laser pulse and shows, as expected, the peak intensity occurs where $t = t_0$ (60 ns). All of the laser energy is delivered in a region around the peak intensity. This region is small compared to the cycle time

Table 5.1: Specifications for a typical laser used in an exposure tool.

Parameter	Value
λ (nm)	193
Repetition Rate (Hz)	4000
t_f (s)	0.00025
$A0$ (mJ/cm^2)	0.05
FWHM (ns)	20

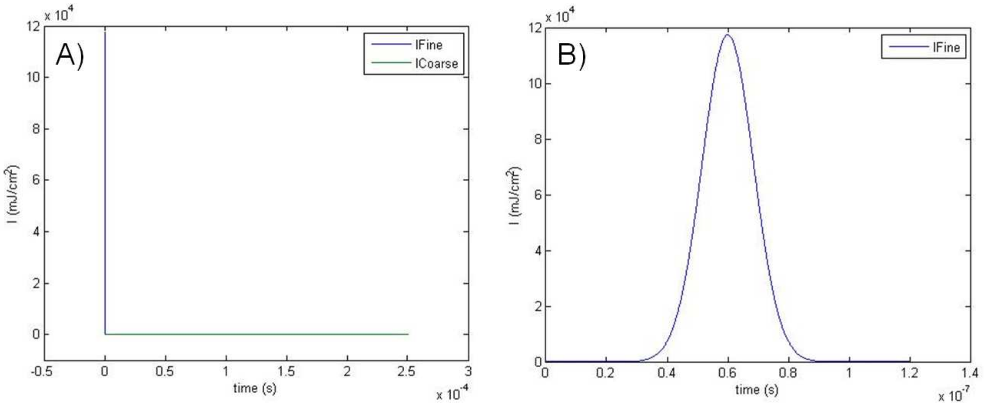

Figure 5.1: Intensity profile of a laser. A) Snapshot of a single pulse. B) Snapshot of the region around peak intensity.

(see Figure 5.1B). After this initial time period passes, no further energy is delivered for the remainder of the pulse.

The description of the intensity profile in Equation 5.1 is used in combination with Equation 2.15 to solve for the acid generation. Because of the difference in the intensity profile between the region immediately surrounding the peak intensity and the rest of the pulse, the intensity profile can be divided into two regimes, “fine” and “coarse”. A solution was devised for each regime.

5.3.1 Solution for the “Fine Regime”

The “fine regime” is define as the region immediately surrounding the peak intensity ($t = 0$ s to $t = 2 \times t_0$). In this regime, the intensity changes dramatically with small increments in time. Given the initial concentrations at the beginning of the pulse and appropriate kinetic parameters, Equations 2.15 and 5.1 are integrated using a 4th order Runge-Kutta method [11]. The resulting concentrations are then used as inputs for the "coarse regime" solution.

5.3.2 Solution for the "Coarse Regime"

The "coarse regime" is defined as the time period between the end of the fine regime and the end of the pulse, and is considerably larger than the fine regime. Although this regime can be solved using the same numerical integration method as the fine regime, a simplified solution can be obtained by noticing that the intensity for the laser is zero within this regime. Equation 2.15 simplifies to

$$\begin{aligned} \frac{d[A]}{dt} &= 1/\tau_1[B] \\ \frac{d[B]}{dt} &= -1/\tau_1[B] + 1/\tau_2[Acid] \\ \frac{d[Acid]}{dt} &= -1/\tau_2[Acid]. \end{aligned} \tag{5.2}$$

If τ_2 was assumed to be very large such that the conversion of the intermediate species to acid is assumed to be irreversible, Equation 5.2 can be further simplified to

$$\begin{aligned} \frac{d[A]}{dt} &= 1/\tau_1[B] \\ \frac{d[B]}{dt} &= -1/\tau_1[B] \\ \frac{d[Acid]}{dt} &= 0. \end{aligned} \tag{5.3}$$

Since no energy is applied by the laser in this regime, this result is expected and shows that the only chemistry that occurs in this regime is the "relaxation" of the intermediate species. As mentioned, this relaxation is crucial in maintaining the nonlinearity of the material by preventing a buildup of the intermediate species. The extent of relaxation can be calculated via analytical integration of the rate equation for the intermediate from $t = 2 \times t_0$ to $t = t_f$ to yield the following

$$\Delta[B] = [B]_{2t_0}\left[1 - \exp\left(-\frac{t_f - t_{2t_0}}{\tau_1}\right)\right]. \tag{5.4}$$

Applying the mass balance, the final concentrations at the end of a single pulse are

$$\begin{aligned}
[A]_{t_f} &= [A]_{2t_0} + \Delta[B] \\
[B]_{t_f} &= [B]_{2t_0} - \Delta[B] \\
[Acid]_{t_f} &= [Acid]_{2t_0}.
\end{aligned} \tag{5.5}$$

These concentrations are then used as inputs to the next pulse. The simplified solution for the coarse regime reduced the computational time required compared to using the ODE solver.

5.3.3 Time Step Size Selection

The size of the time step used in the ODE solver for the 'fine regime' was crucial to the performance of the simulator. The time step needs to be sufficiently small to maintain accuracy and stability. However, smaller time steps also increase the computational time required. For the simulator to be effective, the solver should complete its task in a reasonable amount of time.

The selection for the size of time step for the ODE solver was determined through an error study as function of the time step size. The kinetic and laser parameters used in the study are listed in Table 5.2. The value of 60 ns for t_0 results in a cycle time of 120 ns for the fine regime. To test the accuracy, the cycle time was divided into 20, 50, 100, 200, 500, 1000 time step increments which yielded step sizes of 6 ns, 2.4 ns, 1.2 ns, 0.6 ns, 0.24 ns, and 0.12 ns, respectively. The solver, including both the fine and coarse regimes, was allowed to run until the conversion of acid reached 0.2 (16591 laser pulses). The concentrations after each pulse was recorded. A sample concentration profile is shown in Figure 5.2.

Table 5.2: Simulation parameters used in the time step size study for the ISTP solver.

Parameter	Value
σ_1 (cm^2/mJ)	0.235
σ_2 (cm^2/mJ)	0.235
τ_1 (s)	0.01
t_f (s)	0.00025
t_0 (ns)	60
$A0$ (mJ/cm^2)	0.05
ϕ	1
FWHM (ns)	20
$[A]_{\text{initial}}$	1
$[B]_{\text{initial}}$	0
$[Acid]_{\text{initial}}$	0

The resulting concentration distribution for the 1000 increments case was assumed to be the most accurate and served as the base case for comparison. The acid concentration was used in the calculation for the error in the

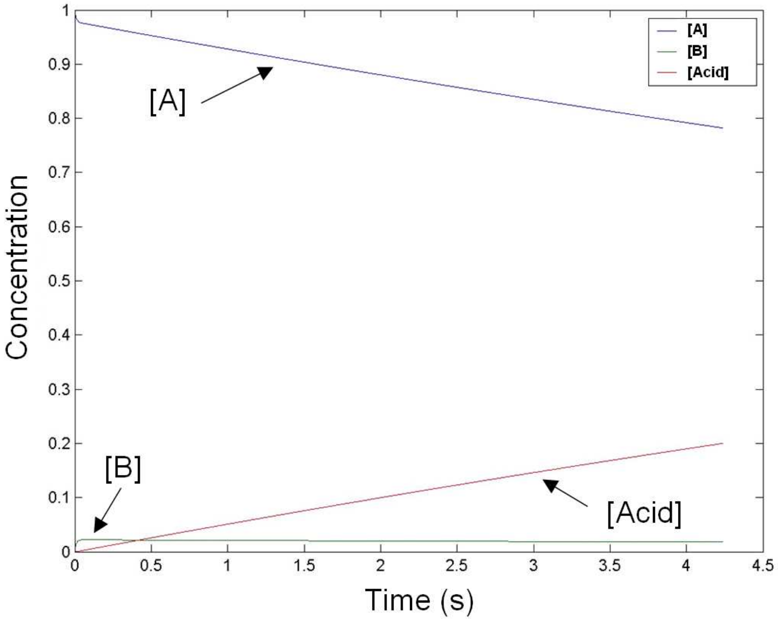

Figure 5.2: Concentration profile as a function of time.

following manner

$$\text{error}_{testinc,t} = \text{abs}\left[\frac{[Acid]_{testinc,t} - [Acid]_{1000,t}}{[Acid]_{1000,t}}\right]. \tag{5.6}$$

The tabulated errors are plotted and shown in Figure 5.3. Figure 5.3 shows that even for the smallest number of increments (20), the error was initially on the order of 10^{-4} and stabilizes to the order 10^{-6}. As the number of increments increased, the order of the error reduced. Some erratic behavior was observed for the 200 and 500 cases, but these were below the order of 10^{-11} or, effectively zero. It should be noted that the data output from the solver only had eight significant digits.

The computational time required for each run was also recorded and

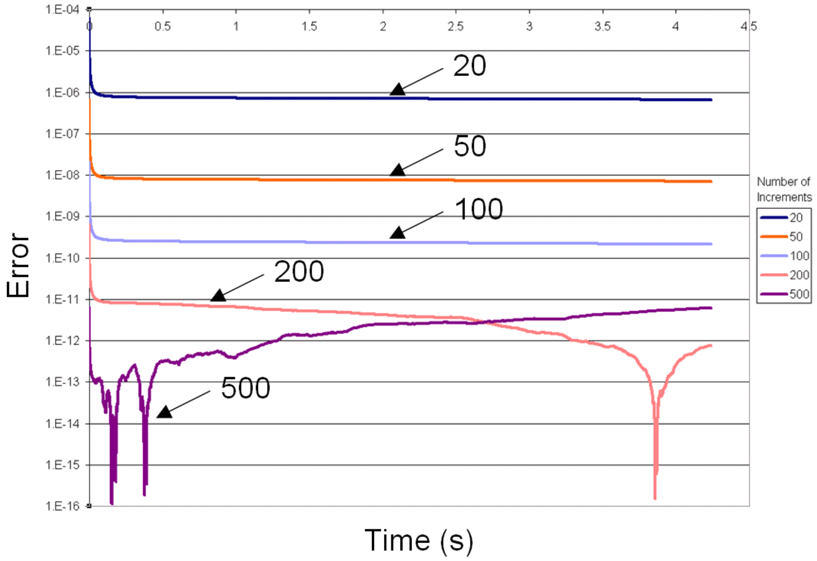

Figure 5.3: Tabulated error with respect to time for different number of increments.

shown in Figure 5.4. As expected, the computational time increased linearly as the number of increments increased. With the 20 increments, the solver required 7.2 min to finish (0.025 s/pulse) whereas with 1000 increments the computational time increased almost ten-fold. This study was performed using a desktop PC with a Pentium 4 2.20 GHz processor and 2.0 GB of RAM. The solver was implemented in MATLAB, an interpreted language. The computational time could be reduced by switching to a faster processor and to a compiled language such as C++ (indeed the final version used in the simulator was implemented in C++). However, the trends should remain the same. Due to the relatively long computational time required for each run, the minimum number of increments with an acceptable error is preferred. The error for the

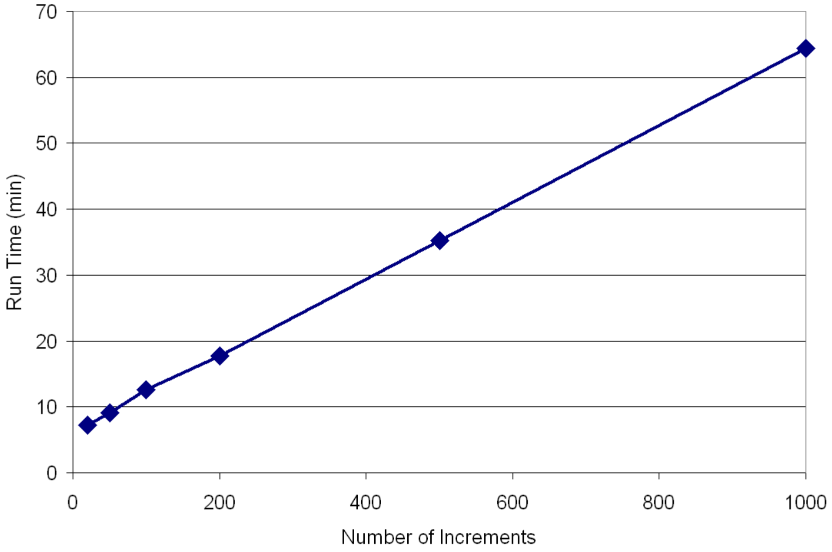

Figure 5.4: Computational run time required for different number of increments.

20 increments case was determined to be acceptable, and a time step size of 6 ns was selected.

5.4 Modeling the OTL Material Response

The behavior of an ideal OTL material was discussed in Section 2.5.4. Initially, there was difficulty in devising a suitable general model with this material mainly because many possible, and very different, mechanisms can be conceived. The mechanisms can range from the ‘alloying’ type model described in Section 2.5.4, where two layers mix to form a substance with a different solubility/etch resistance, to a proposed ‘diffusion valve’ type model, where the OTL material is used as a diffusion valve layer separating two reactants.

In the absence of a known mechanism, it was important to recognize that these mechanisms all share the stepwise or digital threshold dose behavior – i.e. photochemical event only occurs above the threshold dose and dose is 'forgotten' by the material below the threshold. Hence, the simulator was developed based on the behavior described in Equation 2.19.

The lack of a known mechanism also posed a challenge in how to capture the OTL phenomenon within the PROLITH framework. It was decided that the most direct method to capturing the threshold behavior was to directly implement the OTL behavior and resulting patterning response into a single layer. In this case, the resist was selected to be the OTL and the acid generation behavior was selected to be the threshold response. However, it is important to note that the eventual mechanism is not limited to and may not necessitate acid generation. Equation 2.19 was modified to describe the threshold response in conversion in the following manner

$$f\left(I\right)=\begin{cases} [PAC]_{th} & , \quad E_{Actual}\geq E_{th} \\ 1 & , \quad E_{Actual}<E_{th} \end{cases} \tag{5.7}$$

$$\text{where } E_{Actual}=\int_{pulses} I\cdot dt,$$

as before, E_{Actual} and E_{th} represent the actual dose received by the material and the threshold dose, respectively. $[PAC]_{th}$ is the step wise conversion concentration of the photoactive compound after reaching E_{th}.

5.5 Integration of the Modules

The effectiveness of the DEL simulator depends on the ability to integrate the custom modules with PROLITH. The integration of the various custom modules was accomplished using the MATLAB PROLITH Programming Interface (PPI). The PPI is composed of a library of helper functions scripted in MATLAB that is able to communicate with the PROLITH simulation engine via a COM-based linkage. The library replicates most of the functionalities accessible via PROLITH's graphical user interface (GUI) environment. In addition, it also provides access to variables within the simulation engine not available through the GUI. The MATLAB scripting environment and PPI serve as the base platform for the 'driver' function. This function was written to facilitate the interactions between the different modules such as supplying inputs and requesting outputs, and managing the order in which the different modules are called.

The necessary simulation inputs are first supplied to the driver function in the form of parameter files. The driver function then calls the PROLITH file with the desire imaging setup (mask, filmstack, source, etc.) to obtain the image data in resist. The image data is used by the custom code to determine the theoretical behavior of the material after exposure. Depending on the number of exposures, this process is repeated as necessary. After all of the exposures have completed, the resulting resist volume is passed by to PROLITH by the driver function to complete the PEB and development steps. Subsequently, the metrology information and resist profile is extracted. The driver function is also able to run in batch mode to generate the raw data necessary for process window calculations in ProDATA (see Section 5.6). A graphical representation of this work flow is shown in Figure 5.5.

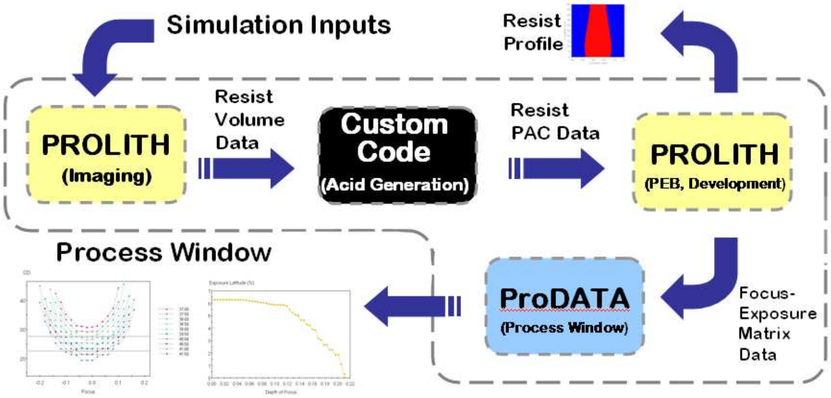

Figure 5.5: Schematic of the work flow in the custom DEL simulator.

5.5.1 Integration of the ISTP Module

The ODE solver described in Section 5.3 is able to model the acid generation given the laser specifications, kinetic parameters, and the number of laser pulses. For a given simulation, the laser specifications and kinetic parameters are constant. However, the number of laser pulses, or dose, is not. In addition, the relative intensity of the exposure light also varies within the film due to material absorbance and optical interference. Fortunately, this information can be obtained from the imaging module of PROLITH. A sample plot of the relative intensity distribution output is shown in Figure 5.6.

After the imaging module has calculated the relative intensity profile

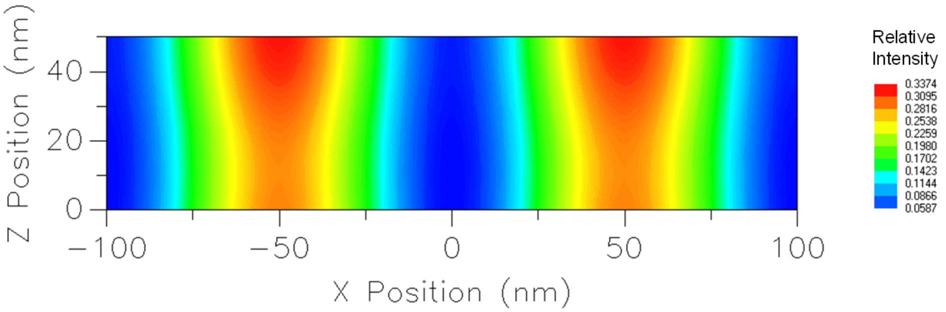

Figure 5.6: Relative intensity profile within the material.

within the material, the integration begins by first outputting the profile to a text file. This text file is subsequently read in by the ISTP module. It was assumed that at the top of the film stack the relative intensity is equal to one, or the incident $A0$. The desired dose to be applied for the particular run was also given to the ISTP module. This dose was used to calculate the number of laser pulses required based on $A0$ in the following

$$\text{number of laser pulses} = \text{ceiling}\left(\frac{\text{dose to be applied}}{A0}\right), \tag{5.8}$$

where the ceiling function is used to round up to the next integral pulse. The ISTP module then iterates through each grid point and solves for the concentrations of all species after exposure at each relative intensity. The resulting acid concentration profile is outputted by the ISTP module and given as an input either to the next exposure pass or the development module.

The ISTP module is mostly implemented in the MATLAB scripting language. But as it was necessary to run the solver for each individual grid point, the solver portion was implemented in C++. Although the C++ version was considerably faster than the MATLAB implementation, it was still the most time consuming portion of the ISTP DEL simulator. The idea of using a look-up table was considered but was rejected after the realization that it would not be practical. First, the table would need to be sufficiently large to encompass a large dose range. Second, the table would only be useful for the first exposure pass. For the second exposure, the individual grid points would have different concentrations depending on their relatively intensities from the first exposure pass. Although more time consuming, it was decided that running the solver at each grid point was a more flexible solution that could easily accommodate multiple exposure passes and changing laser parameters.

5.5.2 Integration of the OTL Module

The behavior described for the OTL module in Equation 5.7 was implemented using the MATLAB scripting language. Similar to the ISTP module, the OTL module first reads in data generated by the imaging module. In this case, only the total dose delivered at each grid point per exposure pass was used. The module checks the dose at each grid point. If the dose is greater or equal to the threshold dose, then the $[PAC]$ is set to $[PAC]_{th}$. Otherwise, $[PAC]$ is set to zero for that grid point. For the second exposure pass, the process is repeated using only the dose distribution from the second exposure pass with no accumulation effects from the first exposure pass. If a grid point has already reached E_{th}, the concentration of PAC remains at $[PAC]_{th}$ even with further exposure. The final distribution of $[PAC]$ is then passed onto the

PEB and development modules.

5.6 Data Analysis

The eventual output of the DEL simulator, after the development module, is metrology information regarding the features in resist such as resist CD, sidewall angle, and resist loss. In a single run mode, the metrology information provides valuable feedback on individual input conditions. When the metrology information from multiple runs and input conditions is aggregated, it can be used to construct a process window that provides a clear picture of the manufacturability of the process. Specifically relevant for a DEL material are the dose and focus latitude of the process. These two factors represent how sensitive the system is to deviations during imaging, one of the most critical steps during manufacturing, and can be studied using a focus-exposure (FE) matrix.

The FE matrix was constructed by systematically varying the dose and focus input values in the imaging module. The result metrology information was recorded. These information were then converted to the appropriate format and processed using commercially available ProDATA v1.4.3 package from KLA-Tencor to generate the process windows. The settings used in the generation of the process windows are shown in Table 5.3. A sample plot of the process windows is shown in Figure 5.7. Figure 5.7A is known as a Bossung plot and shows the trend of the CD as a result of focus and exposure changes. The two gray horizontal lines indicates edge of CD tolerance. The process

Table 5.3: Parameters used to generate the process windows.

Parameter	Value
Target Critical Dimension (nm)	25.0
Critical Dimension Specification (%)	10.0
Sidewall Angle Specification (deg)	0.001
Exposure Latitude Specification (%)	5.0
Resist Loss Specification (%)	100.0
Process Window Shape	Ellipse
Removal Method	None

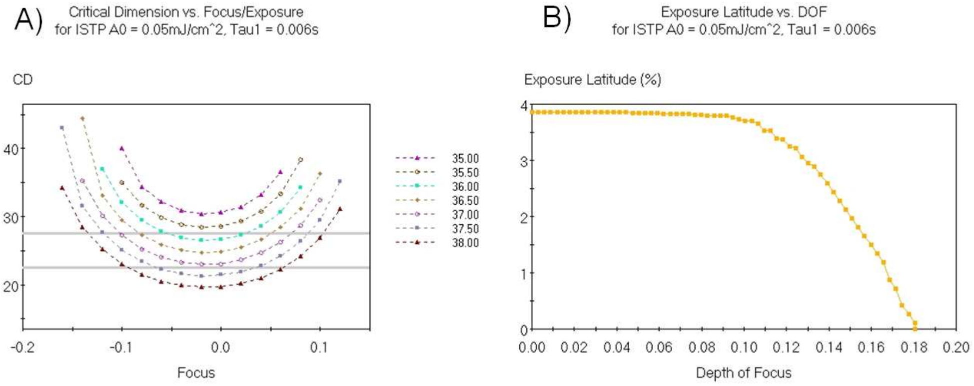

Figure 5.7: Sample process windows. A) Bossung plot (Units: CD (nm), Focus (μm), Exposure Dose (mJ/cm^2)). B) EL (%) vs DOF (μm).

window information is better represented in Figure 5.7B where the exposure latitude (EL) is plotted versus the depth of focus (DOF). An optimized process would operate at a point on the curve such that both the EL and DOF are maximized or the largest total window [82]. This was done by finding the point which had the largest area under the curve.

5.7 Conclusions

The conceptual nature of some of the proposed materials require that custom algorithms be developed to fully model their behavior. An effective DEL simulator was constructed using a combination of available commercial packages and the custom algorithms. This combination allowed the leveraging of existing software packages which have undergone years of refinement and the flexibility of custom algorithms to model the behavior of new materials. The DEL simulator enabled the feasibility studies described in this work.

Chapter 6

Summary of the DEL Material Development Progress

6.1 Introduction

Following the decision to pursue the ISTP and OTL materials, the first step was to find the materials that exhibit the behaviors prescribed by the theoretical descriptions in Sections 2.5.3 and 2.5.4. The theoretical descriptions provided the desired material responses, which were easily captured with mathematical equations on paper and in simulation. In reality, translating the designs to physically realizable materials is challenging. The final material would need to fulfill many requirements including the appropriate chemistries at the operating wavelength, compatibility in device manufacturing conditions, etc. To make the search process more manageable, the first goal was to identify proof-of-principle systems. It should be noted that this overall effort is a collaboration amongst groups in academia (Willson Research Group at The University of Texas at Austin and Professor Nicholas Turro's group at Columbia University) and industry (SEMATECH and its various member companies). The next step in the progression was to use the results to guide the materials development effort, which is to pursue the development of ISTP and OTL materials.

6.2 ISTP Materials Development

To date, the majority of the ISTP proof-of-principle system development was completed by the Columbia group, and the findings have been reported [58]. A summary of the development process is provided here to highlight the current progress. Many of the challenges for the ISTP material were discussed in Sections 2.5.3 and 3.3, but the requirements for the ISTP materials can be reduced to the follow two main criteria or requirements:

Requirement 1 Photons need to be absorbed sequentially, but only generate acid upon absorption of the second photon

Requirement 2 Intermediate species must reverse or decay to maintain nonlinearity

Initial work on Requirement 1 revealed that it was difficult to design and find materials which exhibited both functions. It was determined that the system would be simplified if the functions were decoupled to allow the use of other classes of materials which only exhibit one of the functions. One such method was devised that uses electron transfer to facilitate the generation of acid. The proposed reaction scheme, adapted from Figure 2.9, is shown in Figure 6.1. In this method, the latent PAG is replaced by a latent sensitizer. Similar to the latent PAG, the inactive latent sensitizer can be switched to a functional sensitizer by the absorption of the first photon. The subsequent absorption of a second photon activates the sensitizer. Finally, the activated sensitizer can induce an electron transfer to the PAG and generate acid.

The electron transfer required a proper pairing of the reduction potentials of the sensitizer/donor and PAG/acceptor. Using commercially available software packages, the reduction potentials of various sensitizers and acceptors were calculated. The sensitizer must not be able to directly generate acid upon exposure while the PAG must only generate acid upon electron transfer from the sensitizer. These requirements were met with the donor/acceptor pairing shown in 6.2. Acid generation via electron transfer was experimentally confirmed.

Requirement 2 for the material was met when it was discovered that the sensitizer, 2-methoxynapthalene, undergoes reversible photoinduced dimerization and decomposition back to the monomer as shown in Figure 6.3. This discovery allowed the construction of a proof-of-principle system. The struc-

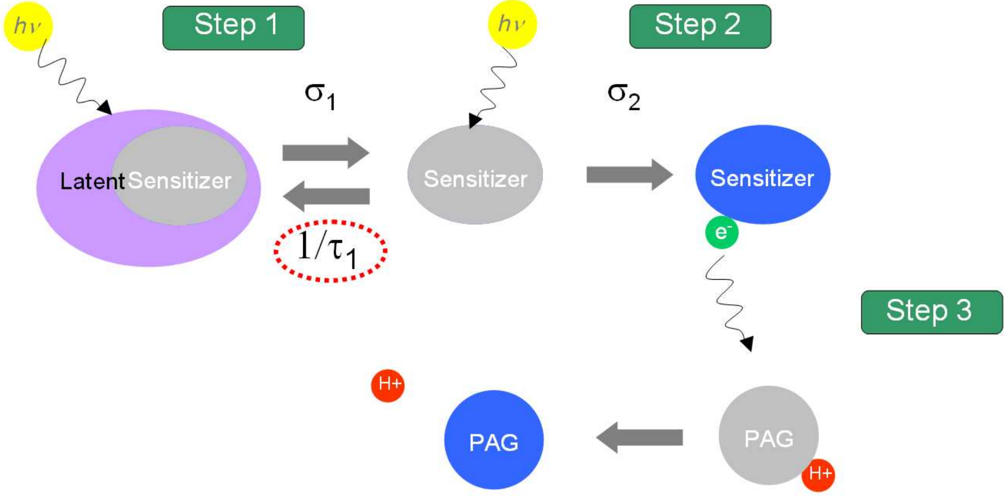

Figure 6.1: Example reaction sequence for a potential ISTP material where acid generation is faciliated via electron transfer.

tures were substituted into the reaction scheme from Figure 6.1, and the resulting system is shown in Figure 6.4. Acid generation starting from the dimer compound was experimentally confirmed. This was an encouraging result and demonstrated the feasibility of the material on a proof-of-principle basis. However, as Figure 6.4 shows, the acid generation was obtained via exposure with 254 nm light. The current state-of-the-art exposure systems uses 193 nm light.

The future work for this material includes identifying an analogous set of molecules that will operate effectively in the 193 nm wavelength range. In addition, the kinetics of the acid generation will need to be quantified and calibrated to achieve the desired nonlinear behavior.

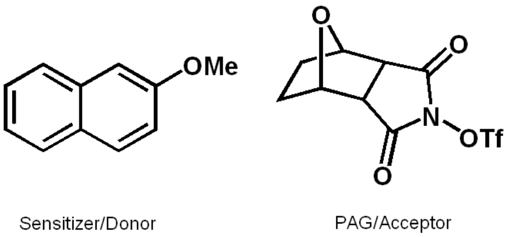

Figure 6.2: Structures of the donor/acceptor pair.

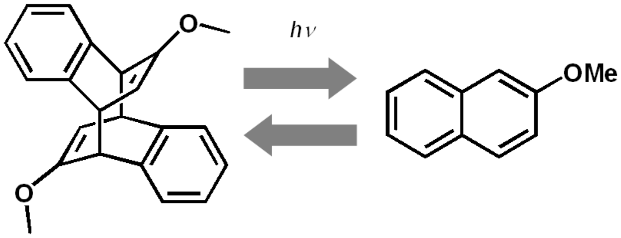

Figure 6.3: Dimerization of 2-methoxynapthalene sensitizer.

6.3 OTL Materials Development

Most of the OTL material development work was performed at The University of Texas at Austin. The section to follow describes the work of Adam Berro, Dr. Younjin Cho, Xinyu Gu, Tomoki Nagai, and Dr. Toshiyuki Ogata [4, 24]. In the same spirit as the previous section, a summary of the development process is provided here to highlight the current progress of the OTL materials development.

As mentioned in the Section 2.5.4, OTLs require the absorption of a threshold exposure dose to induce a photochemical event. This type of behavior is inherent to thermal phase change systems; however, the challenge is to obtain the threshold response with an optical dose as opposed to a thermal dose. One of the main reasons that thermal systems are not suitable for state-

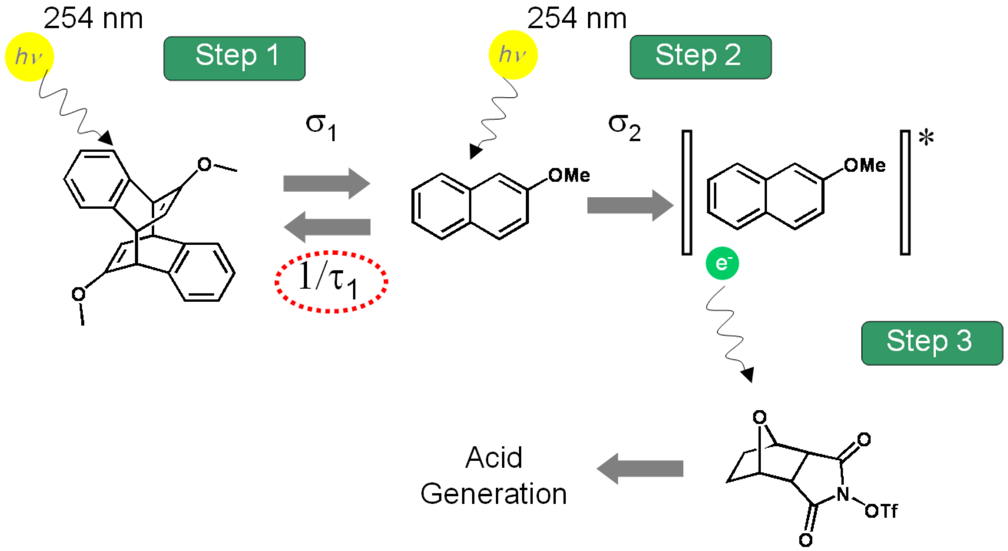

Figure 6.4: Proof-of-principle reaction scheme via electron transfer.

of-the-art lithographic patterning is that the output of current exposure tools is insufficient to perform heating. In addition in order to maintain the strict overlay alignment, the temperature within exposure chambers are carefully controlled. The direct introduction of local temperature variations through exposure can interfere with overlay alignment.

The preceding issues are resolved by not requiring the exposure tool output to perform heating, rather, to induce molecular structural changes within the material. The structural changes subsequently induce changes in the phase transition temperature of the material. For example, the threshold phase behavior can be accomplished by using a material that initially has a melting temperature above ambient (> 25 °C). Upon threshold exposure, the structural properties are changed to bring the melting temperature below ambient. This then allows the energy available in the ambient to induce the necessary threshold phase change response.

As a starting point, we considered a simple OTL system where two reactive substances are separated by a ‘barrier layer’. The barrier layer is initially impermeable to both substances. The regions which receive the required threshold dose undergo phase change and become permeable for one of the reactants. This allows the reactant to diffuse through the barrier layer, mix with the second reactant, and undergo reaction. The products of the reaction then allow for pattern transfer. Finally, the barrier layer is reverted back to the initial impermeable phase before subsequent exposures. This concept of the barrier layer was motivated by the work of O’Leary and Paul [59, 60] where the permeability of CO_2 through a poly(n-alkyl acrylate) polymer film increased by two orders of magnitude through melting phase transition. The specific requirements for this approach are:

Requirement 1 Identifying materials that have photo-switchable/photo-induced phase changes

Requirement 2 Developing processes to exploit the phase change to do patterning

In pursuit of Requirement 1, several azobenzene containing polymers were designed to undergo photo-induced phase change upon exposure. A sampling of the polymer structures is shown in Figures 6.5 and 6.6. Azobenzenes

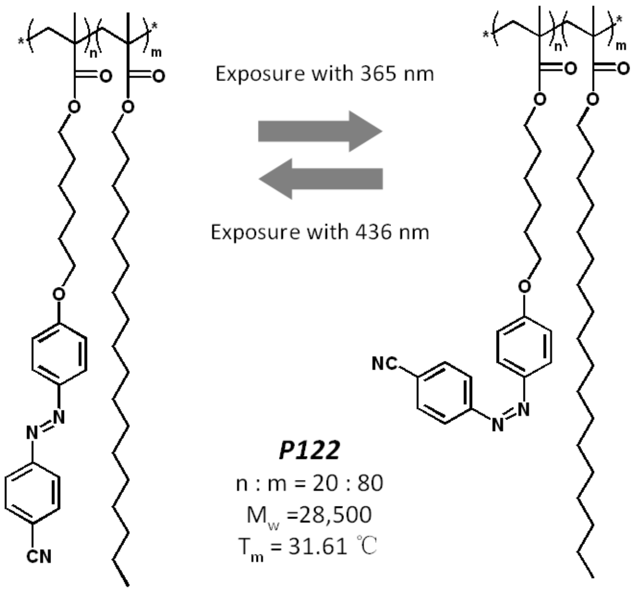

Figure 6.5: Structure of azobenzene containing side-chain crystalline polymer.

were used because of their ability to undergo photo-induced isomerizations at the azo moiety. Figure 6.5 shows the structure of a side-chain azobenzene polymer. The azobenzene group can be reversibly isomerized from the trans to cis and then back to trans by illumination with 365 nm and 436 nm light, respectively. When in the cis conformation, the azobezene group and its substituent act as an impurity to disrupt the crystalline lattice, and cause a shift in the melting temperature (T_m). This phenomena was confirmed by experiment where a shift in T_m of approximately 2 °C was observed in a film after exposure with 365 nm light.

Figure 6.6 shows the structure of a liquid crystalline polymer. Photo-induced isomerization was observed from the trans to cis form with exposure from 340 nm source. But in this case, reverting the cis to trans requires the application of heat. The phase transition was observed by monitoring the refractive index of a film through cycles of exposures with 340 nm light followed by baking (90 °C for 120 s). A 6.1 % change in the refractive index was observed.

The results from the side-chain and liquid crystalline polymers demonstrated the ability to perform photo-induced phase changes. The next step

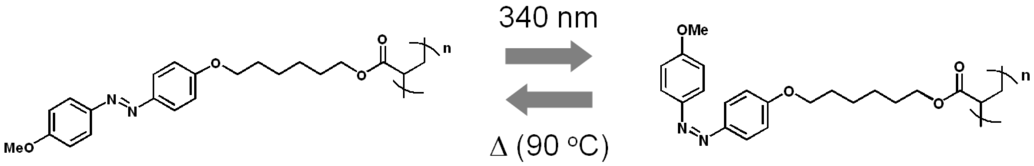

Figure 6.6: Structure of azobenzene containing liquid crystalline polymer.

was determine how to use the phase changes to perform lithographic imaging, which is also the focus of Requirement 2. Although O'Leary and Paul were able to observe large permeability changes with CO_2 as the diffusant, CO_2 is not useful in lithographic imaging applications. In order for this phase change to be useful, a diffusant that can participate in lithographic imaging was required. Since most of the resist chemistries are dependent on acid catalyzed reactions, the use of acid molecules as diffusants, or the ability to modulate the permeability of acid molecules in a polymeric film, was investigated.

A film stack was constructed to test the 'barrier layer' concept with acid molecules. A schematic of the film stack is shown in Figure 6.7. In the setup shown in Figure 6.7, a barrier layer is sandwiched between the feeder layer and detector layer. The barrier layer was composed of film of poly(octadecyl methacrylate) or PODMA. PODMA has a T_m of 31.5 °C and is initially impermeable to acid molecules below the T_m. The feeder layer was composed of poly(butyl methacrylate) with triphenyl sulfonium (TPS) triflate PAG. The

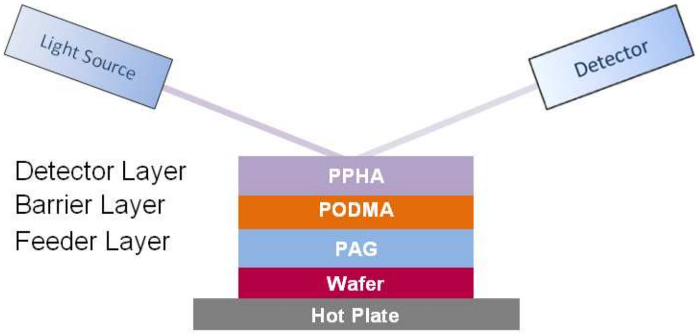

Figure 6.7: Schematic of the filmstack used for testing the modulation of acid diffusivity. *(Courtesy of Xinyu Gu)*

detector layer was composed of end-capped poly(phthalaldehyde) or PPHA. The end-capped PPHA is thermally stable up to 200 °C. However, acid can catalyze a deprotection of PPHA. The deprotected PPHA has a ceiling temperature of −40 °C. At ambient temperatures, the deprotected PPHA rapidly decomposes or "unzips" to its volatile monomeric form. The "unzipping" action serves to amplify the detection of acid. The decomposition of PPHA, subsequent to acid generation due to light exposure, was detected by monitoring the reflectance of the filmstack as a function of the bake temperature. The results are shown in Figure 6.8.

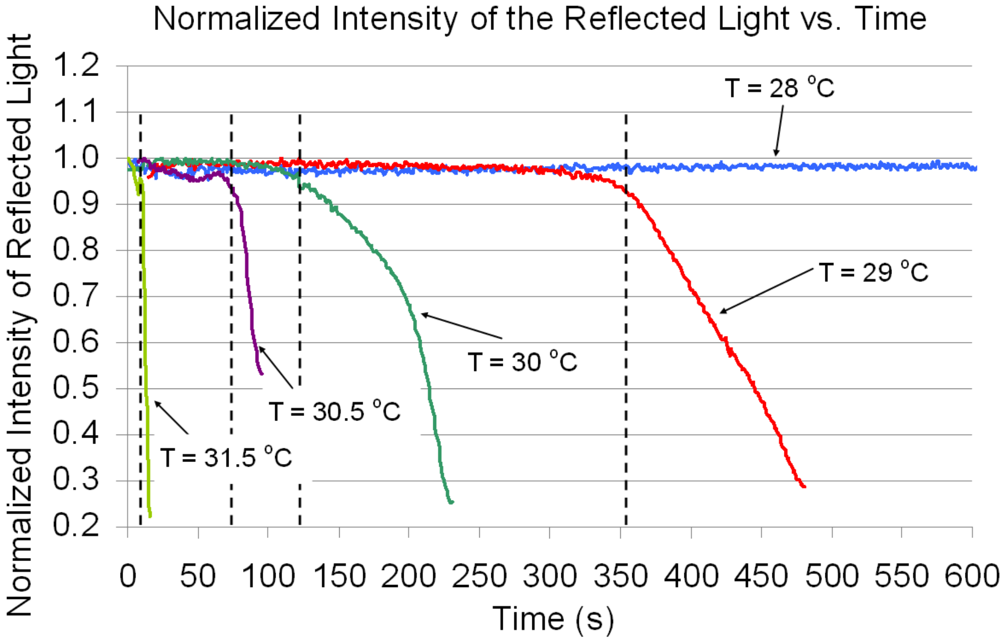

Figure 6.8: Reflectance of the PPHA film after exposure and bake. *(Courtesy of Xinyu Gu)*

Figure 6.8 shows that below the T_m, the reflectance of the film at a bake temperature of 28 °C was unchanged even after a 10 min bake time. As the bake temperature was increased toward the T_m, the bake time required to observe a decrease in reflectance decreased such that at a bake temperature of 31.5 °C (above the T_m) the decrease occurred in less than 10 s. This result confirmed the ability to modulate the permeability of acid molecules through a polymeric film and was a key step towards achieving Requirement 2.

The various experiments have demonstrated the concepts necessary for an OTL material including photo-induced phase change and phase-modulated diffusion of lithographically relevant moieties. However, more work is required in order to achieve a proof-of-principle system. The PODMA barrier layer was able to demonstrate the modulation of diffusion, but the phase change was thermally and not photo-induced. In addition, the transition temperature needs to be reduced to the ambient or room temperature range. The eventual photoactive system will also need to respond to 193 nm radiation. Finally, the specifics of using the photo-induced phase change to perform lithographic imaging also has to be worked out.

6.4 Conclusions

Using the results from the simulation studies, work on the development of the potential ISTP and OTL materials has begun and been described in preceding sections. The first goal was to identify proof-of-concept systems that have the prescribed material responses. A potential system was identified for the ISTP type material using electron transfer to a PAG. However, the kinetics of the process still have to be characterized in detail. Some key concepts such as photo-induced phase change and phase-modulated diffusion were demonstrated through experiments for the OTL material. Work is ongoing to identify a suitable proof-of-concept system. In both cases, the ultimate goal is to find truly manufacturable systems operating in the 193 nm range.

Chapter 7

Introduction to the MUFFINS Platform

7.1 Introduction

Biosensor arrays or “biochips” have become important diagnostic tools with applications in the medical and defense industries. The ability to deliver biosensor arrays at low cost is an important target for the diagnostics community. Although modern biochips have been used in the identification of DNA sequences [14, 43, 47, 62–64, 67, 74, 76], proteins [1, 19, 28, 29, 49], and small molecules [27, 30, 48], low-cost biosensor arrays can potentially increase the availability of advanced diagnostic technologies beyond niche applications such as gene expression studies to more widespread applications such as the diagnosis of common diseases and drug discovery. Achieving the latter will have far-reaching implications on the improvement of public health.

The origin of modern biosensor arrays can be traced back to the British biologist Edwin Southern and the Southern blotting technique [9, 75]. The first generation of modern biochips were fabricated using a spot deposition process in which individual spots of probe samples were deposited onto a glass slide through either non-contact inkjet printing or contact pin printing [68]. These methods were able to print spot-sizes on the order of 100 μm and yield approximately 100,000 spots on a 1 in × 3 in microscope slide.

Several types of biosensor arrays are available commercially [62, 63, 74, 76] and range from silicon-based biochips of Affymetrix (Santa Clara, CA) to bead-based technology of Illumina (San Diego, CA). The Affymetrix "GeneChip" technology uses a combination of photolithography and solid-phase DNA synthesis to produce sequenced target probes on a silicon substrate. The use of photolithography allows for well-controlled fabrication of small spot-sizes (<50 μm) with high spot density. However, the probe length is limited to less than 25-mers. The Illumina technology uses hundreds of thousands of 3 μm beads deposited into etched wells. The beads are functionalized with gene-specific probes sequences that also contain sequences for identification. Although these technologies have shown success and can achieve high information densities, they suffer the drawback that they require specialized and dedicated equipment both for fabrication and detection. Additionally, the systems have mainly been developed for nucleic acid assays and have limited applications with other analytical methods that employ moieties such as proteins and cells.

A new biochip platform named "Mesoscale Unaddressed Functionalized Features INdexed by Shape" (MUFFINS) was developed in the Willson Research Group at The University of Texas at Austin as a potential method to achieve a new low-cost biosensor system. The platform uses poly(ethylene glycol) or "PEG" hydrogels with bioprobes covalently cross-linked into the matrix for detection. Each hydrogel is shape-encoded with a unique pattern such that the information of the hydrogel is associated with the pattern and not its position. Detection occurs through hybridization of the probes with fluorescently labeled targets. Sample images are shown in Figure 7.1. In this document, individual shape-encoded hydrogel shall be generally referred to as a "sensor" while the detection moiety contained within the hydrogel, e.g. DNA sequence, shall be referred to as a "probe". Photolithography enables the encoding of complex patterns and, when appropriately used with self-assembly, also allows parallel fabrication. Several key design elements of the MUFFINS platform have been described in previous publications [22, 51–54, 65, 70–72] and are briefly described here.

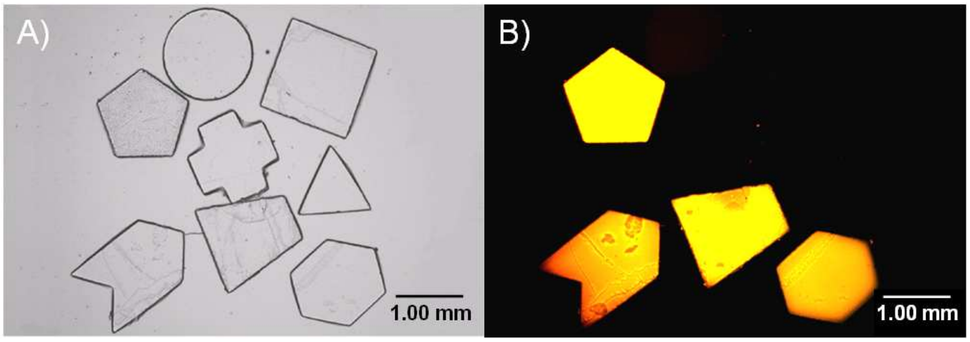

Figure 7.1: Images MUFFINS shape-encoded sensors captured with an optical microscope. A) Bright-field image. B) Fluorescent image showing sensors with hybridized fluorescently-labeled targets. *(Courtesy of Dr. Matthew Schmid)*

7.2 Parallel Fabrication through Photolithography and Self-Assembly

Individual hydrogel sensors were prepared by photolithographically patterning poly(ethylene glycol) diacrylate (PEG-da) into desired shapes through a contact mask. The fabrication process is illustrated in Figure 7.2. Briefly, a pre-polymer solution is dispensed onto a chromium-coated substrate. A photomask is then placed in contact with the liquid prior to exposure. The thickness of the entrapped liquid film is defined by shims. The mask/pre-polymer/substrate assembly is exposed with UV light to polymerize the PEG hydrogels in a negative-tone fashion. After the exposure, the remaining unreacted pre-polymer is rinsed away to reveal the patterned sensors. As seen in Chapter 1, photolithography is a robust and well-understood process. The possible feature patterns and size ranges are only limited by the availability of masks and the resolution limit of contact printing. Projection printing may be used if smaller features are desired. An example a MUFFINS sensor with a more complex pattern is shown in Figure 7.3.

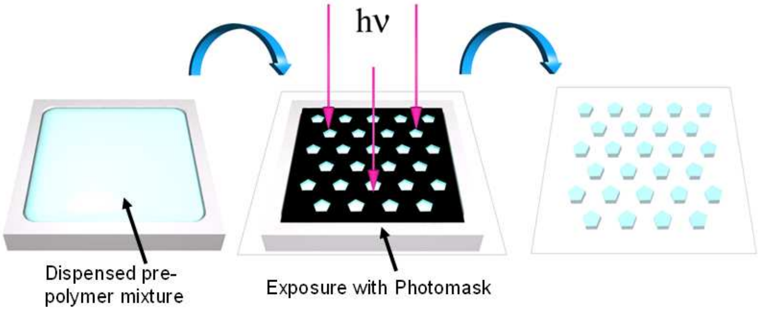

Figure 7.2: Fabrication of the MUFFINS sensor.

The pre-polymer solution is composed of a mixture of PEG-da, bioprobes, water, and photoinitiator. The structures of PEG-da and photoinitiaor are shown in Figure 7.4. The bioprobes are modified with a functional group

Figure 7.3: Complex “Longhorn” shape achievable through photolithography.

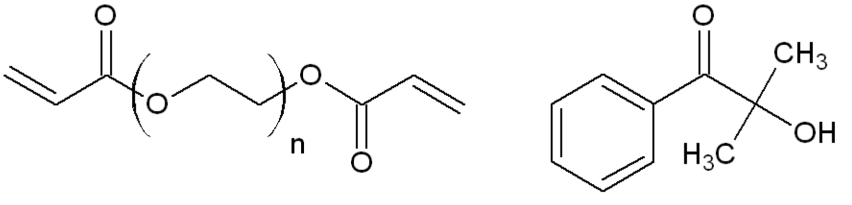

Poly(ethylene glycol) Diacrylate

Darocur 1173 Photoinitiator

Figure 7.4: Chemical structures of poly(ethylene glycol) diacrylate and Darocur 1173 photoinitiator.

(such as acrylamide modification for DNAs) such that they can participate in polymerization and are covalently attached into the polymer matrix.

The PEG-da material used in the fabrication of the hydrogel has demonstrated a wide range of use in biological applications from separations, drug delivery, to biosensing. This is in part due to several of PEG's intrinsic characteristics such as its nonfouling nature or low nonspecific adsorption for proteins and cells [25, 26]. PEG-conjugated proteins and peptides, i.e. protein and peptide sequences that have been covalently attached to PEG, have also been shown to retain their activity. In addition, PEG polymers with molecular weights greater than 2,000 are nontoxic and nonimmunogenic. Previous works have demonstrated the use of different bioprobes such as proteins [83] and cells [38] as analytes in sensing applications.

Decoupling the sensor identification from the location also enables parallel fabrication of the arrays. Large quantities of individual sensors can be produced separately and then self-assembled to form random arrays. This process is illustrated in Figure 7.5. The self-assembly process takes advantage of attractive lateral capillary forces that exist between an air-liquid interface. The phenomenon is often referred to as the "Cheerios Effect" [6, 78].

To create a self-assembled array, the sensors were first placed on the surface of a cross-linkable liquid pre-polymer. Although the sensors are denser than the liquid, surface tension enables them to float [45]. Attractive capillary forces between the sensors drive the aggregation of the sensors. An external agitation force is used to increase sensor mobility and to break up small aggre-

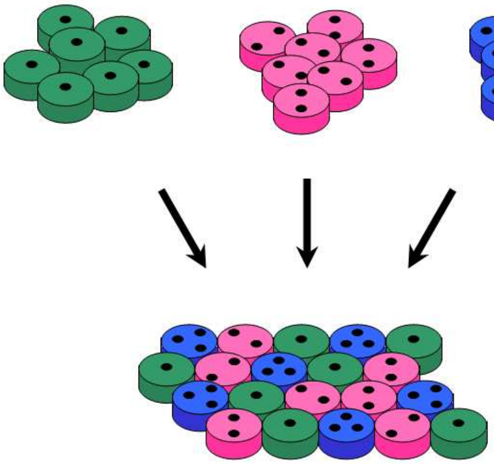

Figure 7.5: Parallel fabrication process: large batches of individual sensors are fabricated in parallel and then subsequently combined to form a large array.

gates caught in local energy minima that tend to hamper the overall assembly. Over time, a dense, hexagonally close-packed array forms on the pre-polymer surface. To permanently set the sensors, the whole array is exposed to ultraviolet radiation, thereby cross-linking the liquid pre-polymer. The resulting array is then extracted and used for sensing. This process is illustrated in Figure 7.6. An example of an array after self-assembly is shown in Figure 7.7.

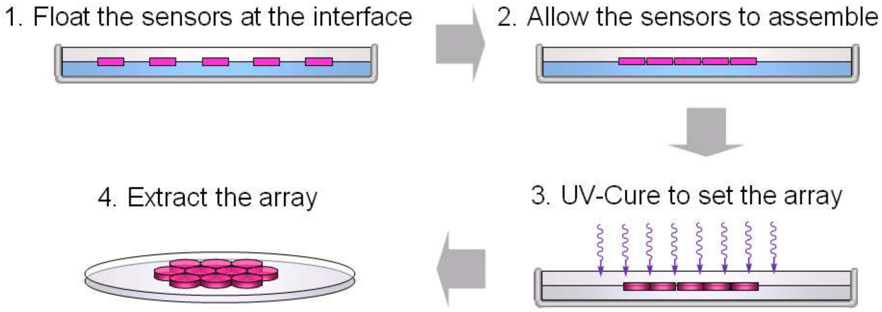

Figure 7.6: Self-assembly process used to fabricate the MUFFINS array.

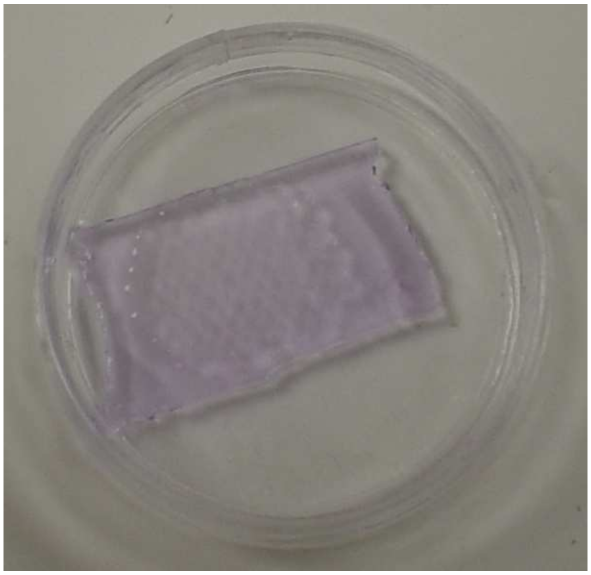

Figure 7.7: Extracted array (the color is from the fluorescently labeled targets) after self-assembly process.

7.3 Multiplexing

The information density is increased by the use of multiplexing, or the incorporation of more than one unique probe in each sensor. Probe multiplexing is a unique ability afforded by the hydrogel. The high signal-to-noise response of the hydrogels enables multiple sequences to be placed in each sensor, thereby reducing the number of sensors required. In the simplest probe loading scheme, each unique probe is mapped to one unique sensor type. In a multiplexed loading scheme, multiple probes are loaded into individual sensors in a predetermined scheme. The response of the array is decoded by observing the combinations of positive sensors that correspond to the predetermined scheme. In previous work by Schmid and co-workers [70, 71], a binary encoding scheme was used to build an array for the purpose of detecting single-nucleotide-polymorphism (SNP) within the p53 gene. The array used five multiplexed sensors to detect for twenty-nine possible SNPs. Generally, when sensing for a single analyte, the number of possible probes is determined by

$$\text{number of probes} = 2^{n_{shapes}} - 2 \tag{7.1}$$

where n_{shapes} is the number of unique sensor shapes. A comparison of the conventional one-to-one probe-to-sensor loading method versus the multiplexed method is shown in Figure 7.8.

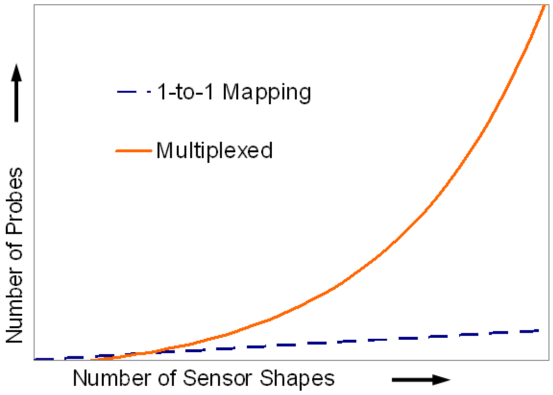

Figure 7.8: Comparison of the one-to-one probe-to-sensor loading method versus a multiplexed method. *(Adapted from Ref. [70])*

7.4 Shape-Encoding

Initially, simple geometric shapes (as seen in Figure 7.1) were chosen in earlier work to mainly demonstrate the efficacy of hydrogel-based sensors. As the number of sensors in an array increased, a more sophisticated and systematic shape-encoding scheme was required. Subsequently, a shape-encoding scheme was developed along with a new pattern recognition algorithm to perform automated detection and demonstrate the efficacy in full scale usage [51, 52].

The shape-encoding scheme is based on a two-dimensional grid system of "dots" as illustrated in Figure 7.9. The identity of a sensor is encoded within the region of "coding dots" using a binary encoding system. The presence of

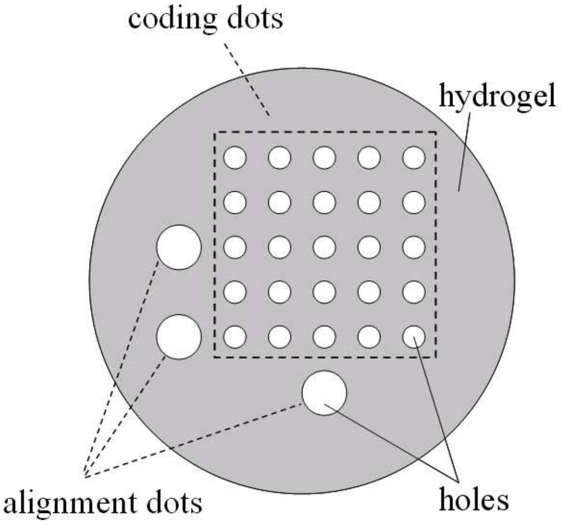

Figure 7.9: Shape-encoding system used to identify each hydrogel sensor. The system is comprised of a 5 × 5 grid of coding dots and three larger alignment dots.

a coding dot corresponds to a value of ‘1’ whereas the the absence of a coding dot corresponds to a value of ‘0’. Using this system, a sequence of binary numbers can be generated by concatenating the values from each row in a top-down fashion as illustrated by Figure 7.10. In addition to the coding dots, the encoding scheme also includes three larger alignment dots. These dots impart “chirality” to the sensors and are used to identify the rotation and orientation of individual sensors. These alignment dots are necessary since the assembly process deposits the sensors in the array randomly. Each sensor is also given a circular outer shape that aids in packing during self-assembly.

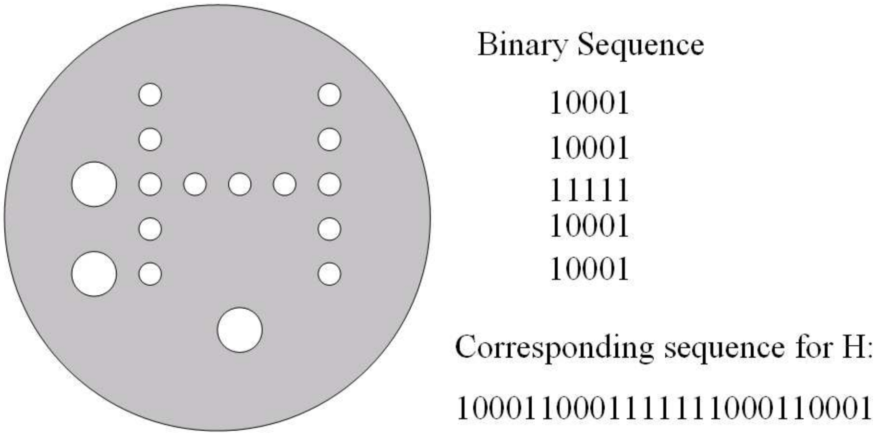

Figure 7.10: Sample image of the “H” sensor pattern and the corresponding binary number sequence.

The number of possible pattern combinations using the grid pattern design is a function of the number of rows and columns and scales as $2^{(n_{rows} \times n_{cols})}$. Depending on the number of unique sensors required, the pattern can range from a 2×2 grid (16 unique patterns) to a 5×5 grid ($>$ 33.5 million unique patterns) and beyond. The systematic grid design also facilitates automated pattern recognition of the sensors that adapts easily to the size of the grid, even as the size of the grid increases. As mentioned, the use of photolithography in the fabrication of the MUFFINS sensors readily accommodates the increased complexity of the dot-matrix encoding scheme.

7.5 Comparison of the MUFFINS Platform and Existing Technologies

The aim of the MUFFINS project is to develop a versatile platform for deployment of various biological probes that is technologically comparable to existing platforms, but achieved with potentially lower manufacturing and operating complexity. This section briefly compares the attributes of the MUFFINS platform with other technologies.

Although both the Affymetrix and MUFFINS platform are manufactured using photolithography, the two manufacturing processes differ in their respective complexity. The MUFFINS platform utilizes a single contact printing exposure step to pattern the pre-polymer (with pre-sequenced probes), whereas the Affymetrix process requires multiple exposure steps to sequence individual probe sequences onto the substrate. The latter not only increases the number of processing steps required, but also requires additional materials such as photomasks. As previously mentioned, the Affymetrix technology is limited to probe lengths less than 25-mers; the MUFFINS and Illumina platforms do not have this limitation. Depending on the substrate used, the

Illumina BeadArray technology may also require a photolithography step and subsequent etching to prepare the individual wells [31].

Both the Illumina and MUFFINS platforms employ parallel batch fabrication and self-assembly during array formation. The Illumina technology requires individual 3 μm beads to assemble into pre-patterned wells, whereas the MUFFINS technology requires lateral capillary forces to assemble the sensors into close-packed configurations. To some extent, both of these methods depend on inherently random self-assembly processes that may be difficult to control in a manufacturing setting. However, the detection of the MUFFINS sensors do not require close-packed configurations.

The Affymetrix and Illumina platforms do offer significantly higher information density compared to the current MUFFINS design. The Affymetrix GeneChip has a total of 500,000 25-mers on a 12.7 × 12.7 mm glass chip, ($\approx$ 3100 probes/mm^2) while the Illumina Sentrix Beadchip has a total of 46,000 79-mers on a 25 × 75 mm glass slide ($\approx$ 24.5 probes/mm^2) [69]. In comparison, approximately 1,875 1 mm MUFFINS sensors can fit on a 25 × 75 mm glass slide ($\approx$ 1 probes/mm^2). While the Affymetrix and Illumina platforms have higher information density, the main trade-off is that they require very specialized, expensive equipment to read the arrays. The MUFFINS sensors in principle can be read by a typical laboratory fluorescence-capable optical microscope. In addition to the possibility of increasing the information density through multiplexing, the density can also be increased by reducing the size of the MUFFINS sensors. Similar information density of the Illumina platform can be obtained by using 0.2 mm sensors (≈ 25 probes/mm^2). The relationship between the information density of the MUFFINS platform and the individual sensor size is shown in Figure 7.11.

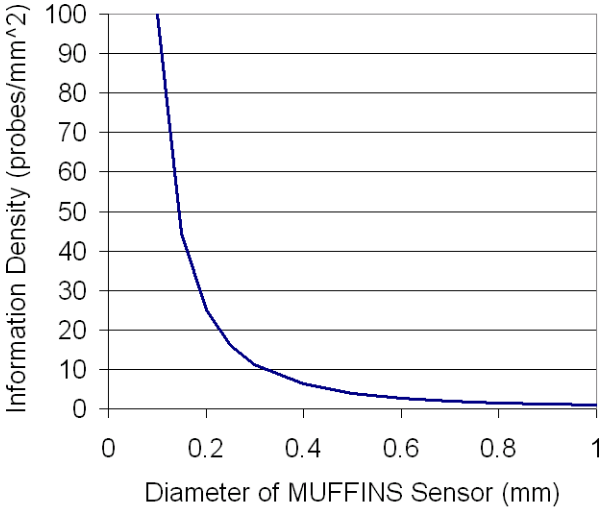

Figure 7.11: Information density of the MUFFINS platform as a function of sensor size using a 1-to-1 (no multiplexing) probe loading scheme.

Due to its three-dimensional design, the MUFFINS platform also offers the potential for increased signal-per-unit area compared to the Affymetrix and Illumina platforms which use rigid glass or silicon substrates. The MUFFINS hydrogel introduces an additional height dimension to entrap additional probes. The glass or silicon substrate only allows surface attachment. However, this does introduce diffusion considerations for the MUFFINS platform that may be mitigated by the adjustment of polymer properties (molecular weight, composition, etc.) and shape design. Additionally, the PEG hydrogel design also allows the incorporation of bioprobes such as cells that would be difficult to implement on rigid substrates. These aforementioned attributes and comparisons suggest that the MUFFINS technology is a potential biosensor array platform, and warrants investigation.

7.6 Platform Development

The development of the MUFFINS platform thus far has been the culmination of the work of many former graduate students, post-doctoral fellows, and undergraduate students. The nonexhaustive list includes Benjamen Rathsack, David Johnson, Matthew Schmid, Jason Meiring, Michael Dickey, Elizabeth Costner, Peter Carmichael, Scott Grayson, Jason Bates, Romy Kirby, Kalpana Manthiram, and Steven Abboud.

Several aspects of the MUFFINS platform design including the sensor fabrication, multiplexing, and analyte sensing have been demonstrated in previous publications [22, 52–54, 65, 70–72]. The chapters to follow describe the details of two remaining aspects of the platform, namely, self-assembly mechanics and pattern recognition algorithm. Finally, Chapter 10 describes a demonstration of all the key design elements using a single array.

Chapter 8

Self-Assembly Dynamics of MUFFINS Array Formation

8.1 Introduction

The shape-encoding design of the MUFFINS platform allows for random assembly of different sensor types that are fabricated in a parallel fashion. Large numbers of individual sensors can be produced separately, combined, and then self-assembled to form arrays. The self-assembly process takes advantage of attractive lateral capillary forces that exist for objects floating at an air-liquid interface. The phenomenon was popularized by Whitesides and co-workers and is often referred to as the "Cheerios Effect" [6, 78]. The assembly of hydrogel features entailed floating the MUFFINS on the surface of a pre-polymer solution. The sensors then self-assemble to form a close-packed configuration. The surrounding pre-polymer solution is subsequently UV-cured to set the array to lock-in the configuration. The self-assembly process is illustrated in Figure 8.1. These self-assembly dynamics are explored through modeling in this chapter.

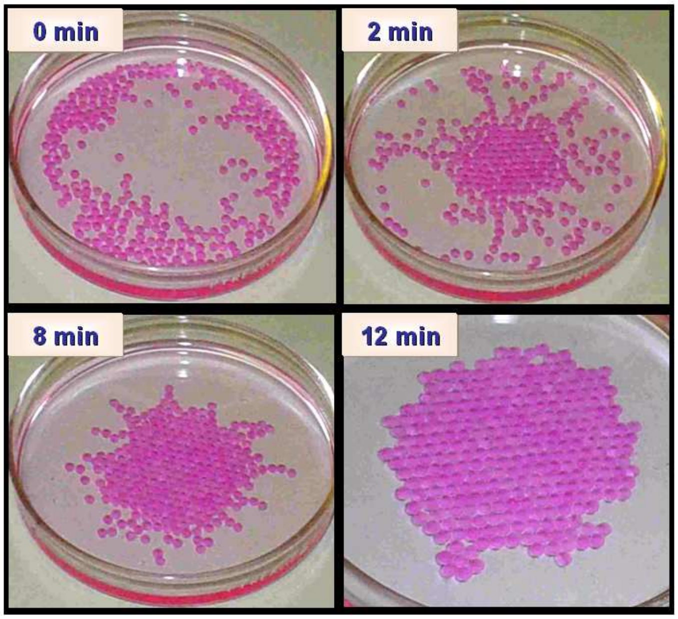

Figure 8.1: Time lapsed images showing the self-assembly of sensors floating at an air-liquid interface. (*Courtesy of Prof. Scott Grayson*)

8.2 Describing the Surface Interactions

The self-assembly of objects floating at an liquid-air interface has been studied extensively [5, 6, 12, 39, 40]. In general, the attractive force is due to a combination of surface tension and buoyancy induced hydrodynamic forces. However, most of these efforts have focused on objects that are less dense than the liquid phase. The MUFFINS sensors are denser than the pre-polymer liquid phase and form a wetting contact angle with the liquid. Both of the preceding arguments suggested that the objects should not float, but the contrary was observed in practice. This phenomena is studied through modeling. The first part of the model attempts to describe the flotation phenomenon of hydrophilic mesoscale objects that are denser than the liquid and their assembly behavior.

8.2.1 Flotation of One Particle

The flotation of a MUFFINS sensor or, more generally, a particle is governed by the balance between gravitational and buoyant forces. However, if the particle is denser than the fluid, the buoyant term cannot supply enough force to keep the particle afloat and must require alternate sources to maintain flotation. In this case, that force is supplied by surface tension.

It is important to note that for objects that form wetting contact angles with the liquid, the contact angle constraint dictates that the contact line should be less than 90 °. This leads to a downward vertical component of the surface tension that does not aid in flotation, please see Figure 8.2A. The only

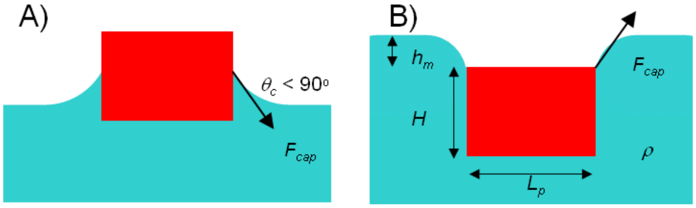

Figure 8.2: A) Contact line shape for objects with density less than the fluid. B) Contact line shape for floating objects that are denser than the fluid.

possibility which allows the meniscus to be directed upwardly occurs if the meniscus is pinned at the top corner of the object. If the corners are assumed to be rounded on a microscopic scale, an effective "contact line" forms that can rotate locally about the corner to maintain the contact angle constraint. The orientation of this interface is defined as the "contact line angle", θ_c, which is able to change to accommodate the force balance and keep the particle afloat.

The vertical force balance per unit width w (the object is assumed to be infinitely long bars into the page to simplify the calculations) is shown below

$$\begin{aligned} F_w &= F_b + F_m + F_{cap} \\ F_w &= Mg/width \\ F_b &= \rho g L_p H \\ F_m &= -\rho g L_p h_m \\ F_{cap} &= \gamma sin\theta_c \end{aligned} \tag{8.1}$$

where F_w is the weight of the object, F_b is buoyant force, F_m is additional upward force due to the object's sinking below the water line by height h_m,

F_{cap} is the vertical component of the surface tension γ, θ_c is the contact line angle, and $\Delta\rho$ is the density difference between the lower and upper fluids.

In order to obtain the contact line angle θ_c, it is necessary to first describe the fluid surfaces around the objects. The surfaces can be described by the balance between the capillary and hydrostatic pressures as shown in the relation

$$\gamma \nabla \cdot \underline{h} = -\rho g \underline{h} \tag{8.2}$$

where $\underline{h}$ is the position vector describing the interface. After linearization and application of the appropriate differential operator in rectangular coordinates, Equation 8.2 simplifies to the ordinary differential equation

$$\frac{d^2h}{dx^2} - q^2 h = 0 \qquad \text{where } q^2 = \frac{\rho g}{\gamma}. \tag{8.3}$$

The inverse of q is commonly known as the capillary length. Equation 8.3 was solved with the appropriate boundary conditions to obtain solutions that describe the surface

$$h(x) = \frac{-\tan\theta_c e^{-qx}}{q}. \tag{8.4}$$

Please consult Appendix A for detailed derivation.

8.2.2 Flotation of Two Particles in Close Proximity

The solution derived for the flotation of the one particle case can be extended to describe the flotation of two particles in proximity. For the two particles case, the boundary conditions are slightly altered due to the presence of the second particle which disturbs the meniscus. The solution for the meniscus is separated into an inner region that exist between the two particles and an outer region that extends from the particle to an infinite undisturbed surface. To simplify the geometry and mathematical complexity of the problem, two rectangular particles were used as shown in Figure 8.3. In Figure 8.3, the subscript "i" denotes the inner region while the subscript "o" denotes the outer region. The variables ρ_U and ρ_L represent the densities of the upper and lower fluid, respectively. The coordinate system is set such that $x = 0$ is at the center between the two particles and $x = L_s$ is the half distance between the particles. The length of the particle is defined by L_p. Figure 8.3 also introduces a new variable, L_{eff}, which is the projection of the original particle length L_p in the x-coordinate. The L_{eff} variable is useful if the particle ex-

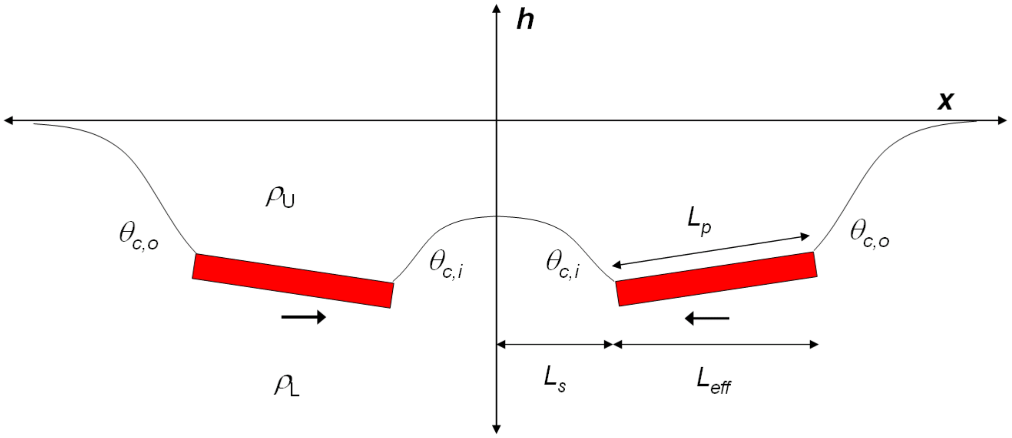

Figure 8.3: Schematic of the Two Particles.

periences rotation and will be discussed in the next section. The particles are also assumed to be long bars extending into the page so that the end effects are minimal.

For the outer solution, the boundary conditions are as follows

$$\begin{aligned} h_o(x \to \infty) &= 0 \\ \frac{dh_o}{dx}(x = L_s + L_{eff}) &= \tan\theta_{c,o}. \end{aligned} \tag{8.5}$$

The coordinate system assumes that the height of the unperturbed surface is zero and the height gradient at the interface between the particle and meniscus is determined by the contact line angle, $\theta_{c,o}$. Applying the boundary conditions gives the resulting equation describing the height of the meniscus

$$h_o(x) = \frac{-\tan\left(\theta_{c,o}\right) e^{-q\left(x-(L_s+L_{eff})\right)}}{q}. \tag{8.6}$$

Again, these equations are given without derivation in the interest of brevity. Please consult Appendix A for more details.

The boundary conditions for the inner region are as follows

$$\begin{aligned} h_i(x = L_s) &= h_{i,p} \\ \frac{dh_i}{dx}(x = 0) &= 0. \end{aligned} \tag{8.7}$$

The second boundary condition is obtained assuming the meniscus shape is symmetrical so that the gradient at the midpoint, x = 0, is equal to zero. Applying the boundary conditions gives the resulting equation describing the height of the meniscus in the inner region

$$h_i(x) = \frac{h_{i,p} cosh(qx)}{cosh(qL_s)}. \tag{8.8}$$

Furthermore, the inner contact line angles can be obtained through the following relation

$$\frac{dh_i}{dx}(x = L_s) = \left. \frac{h_{i,p}\, qsinh(qx)}{cosh(qL_s)} \right|_{x=L_s} = \frac{h_{i,p}\, qsinh(qL_s)}{cosh(qL_s)} = -\tan\theta_{c,i}. \tag{8.9}$$

8.2.3 Meniscus Induced Tilt

Due to the proximity of the second particle in the inner region, the meniscus of the two particles superimpose and the contact line angle in the inner region changes in order to maintain a smooth meniscus curvature. The change in $\theta_{c,i}$ causes a discrepancy in the vertical contribution of the capillary force between the inner and the outer regions and results in tilting of the particles, this is shown in Figure 8.4. Figure 8.4 shows that the tilt angle of

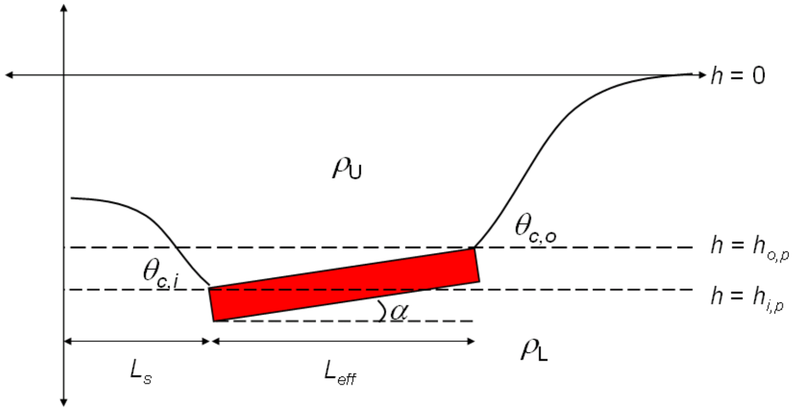

Figure 8.4: Close-up Schematic of One Particle

the particle is described by α and can be obtained through the trigonometric relation

$$\sin \alpha = \frac{h_o - h_i}{L_p}. \tag{8.10}$$

The tilt angle is governed by the torsional forces acting on the particle which is dependent on various variables such as $h_{o,p}$, $h_{i,p}$, $\theta_{c,o}$, $\theta_{c,i}$, and L_{eff}. These variables are in turn all dependent on the separation distance L_s through a system of equations relating the vertical force balance, torque balance, and meniscus shape. In the interest of brevity, the complex system of equations and its derivation is not shown here. Suffice it to say that the solutions to the variables can be obtained by specifying L_s and simultaneously solving the system of equations. Please consult Appendix A for more details.

8.3 Tilt Modeling

The system of equations described in the previous section and Appendix A was solved using a script written in the MATLAB programming language to determine the orientation of two floating objects after assembly. It was assumed that the objects had come into contact when the separation distance L_s is 1×10^{-5} m. The density of the particle ρ_p, surface tension of the liquid phase γ, and the particle length L_p were varied to study the effects on α. The particle thickness H and the liquid density were kept constant at 0.57 mm and 1000 Kg/m^3, respectively. In the first run, γ was varied from 0.02 N/m to 0.1 N/m and L_p was varied from 0.1 mm to 20 mm while the ρ_p was held constant.

In the second run, ρ_p was varied from 1000 Kg/m^3 to 4000 Kg/m^3 and L_p was varied from 0.1 mm to 20 mm while the γ was held constant.

The results of the simulation were plotted as surface plots that are shown in Figures 8.5 and 8.6. Figure 8.5 shows that α decreases with increasing γ. At lower γ values, the liquid surface has less contribution from surface tension to support the particle. As the $\theta_{c,i}$ reduced due to lower separation distances, the F_{cap} in the inner region is also reduced and causes the inner corner to sink until the force due to the sunken height rebalances the torque. Figure 8.5 also shows a rapid increase in α at small L_p as γ is decreased. The solver began to fail at γ values less than 0.020 N/m, signifying that the tilt was no longer able to compensate for the torque and weight of the particle.

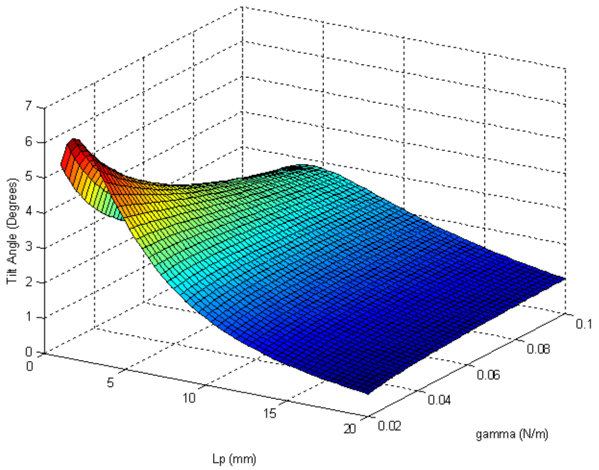

Figure 8.5: Surface plot showing the dependence of the tilt angle α on γ and L_p.

Figure 8.6 shows that α increased with increasing ρ_p. As ρ_p increased,

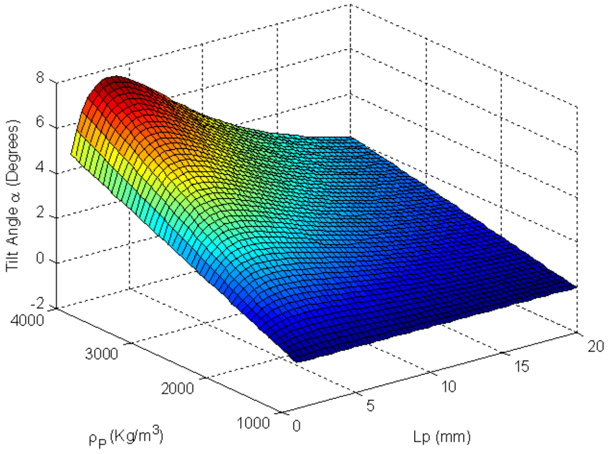

Figure 8.6: Surface plot showing the dependence of the tilt angle α on ρ_p and L_p.

the amount of weight that must be supported by the surface tension also increased. Since γ was held constant, the particle must increase α to balance the torque. Similar to the previous case, the tilt angle also increased to a critical ρ_p where the solver began to fail.

The increased L_p also amplifies the contribution of γ by increasing the moment arm. Small changes in α resulted in larger changes in sunken height due to the longer hypotenuse in Equation 8.10. A maximum in α was observed when L_p was approximately 3 mm. When L_p was less than 3 mm, the weight of the particle was low enough to be supported by the changing $\theta_{c,i}$.

To illustrate the effect of the separation distance L_s on α, a model system with silicon particles floating on water was simulated. This system was selected because silicon is denser than water, but forms a wetting contact angle. The relevant parameters are shown in Table 8.1.

Table 8.1: Parameters used in the study of the separation distance L_s on α.

Parameter	Value
Particle Density ρ_p (Kg/m^3)	2300
L_p (mm)	6.10
L_{depth} (mm)	5.0
Liquid Density ρ_L (Kg/m^3)	1000
Surface Tension γ (N/m)	0.073

Various L_s values were used from 0.01 mm to 10.0 mm. The results of the simulation are shown in Figures 8.7 - 8.9. Figure 8.7 shows that when the particles are far apart $L_s = 10.0$ mm, essentially no tilt (0.002 °) was observed. At this distance, the meniscus has ample room to form the desired shape and contact line angle. The simulated tilt angle begins to decrease as the L_s is reduced. At shorter distances, the inner contact line angle must change in order to maintain a smooth curvature. This effect can be observed in Figure 8.8. Both the $\theta_{c,i}$ and $\theta_{c,o}$ has a constant value of approximately 9 ° when L_s is greater than 7 mm. When L_s is less than 7 mm, $\theta_{c,i}$ begins to reduce rapidly toward zero. Finally, the tilting of the particle is observed in the pinned height of the inner and outer meniscus as shown in Figure 8.9. The height of the inner meniscus decreases while the height of the outer meniscus increases as L_s is reduced.

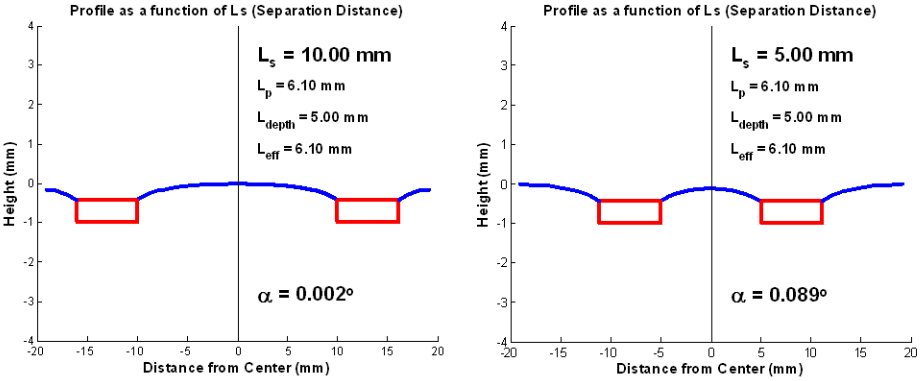

L_s = 10.00 mm
α = 0.002°

L_s = 5.00 mm
α = 0.089°

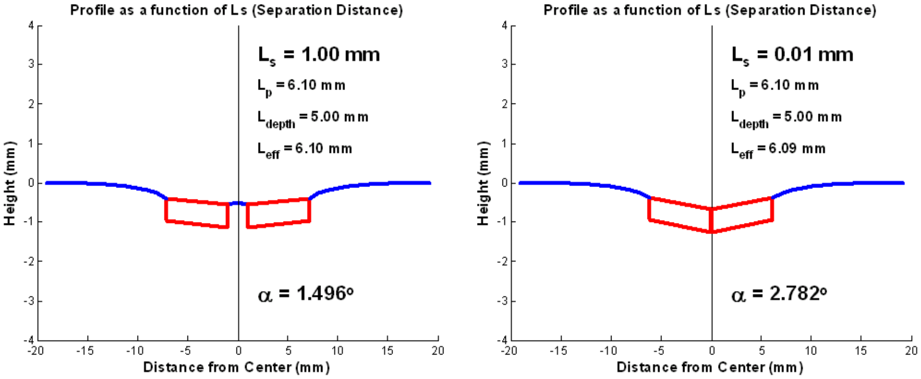

L_s = 1.00 mm
α = 1.496°

L_s = 0.01 mm
α = 2.782°

Figure 8.7: Meniscus profile and tilt angle with respect to the separation distance L_s for the model system.

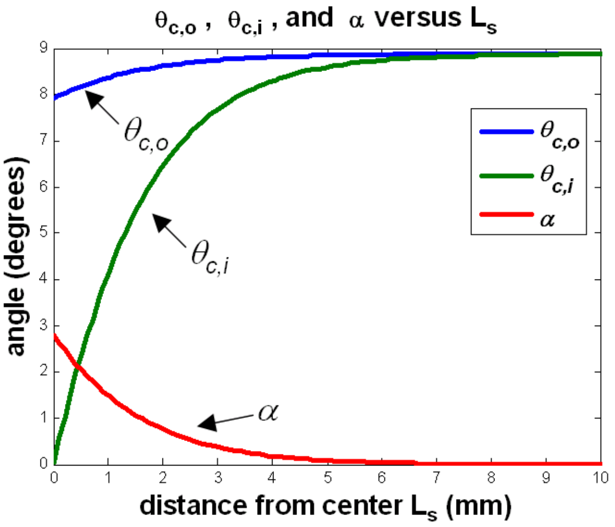

Figure 8.8: Tilt and contact line angles with respect to the separation distance L_s for the model system.

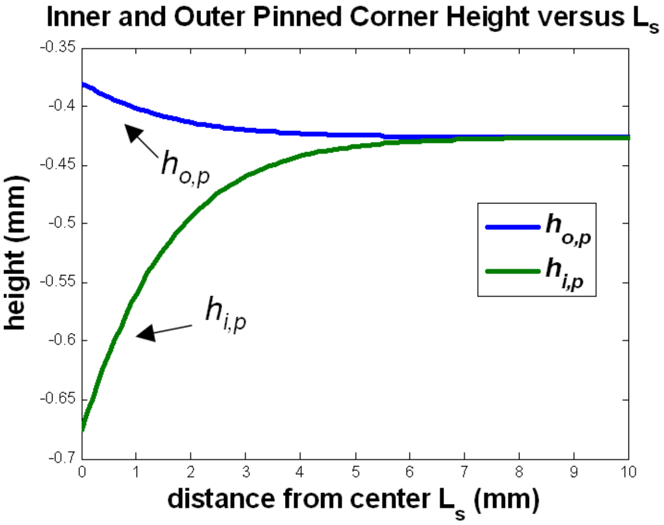

Figure 8.9: Pinned height of the inner and outer meniscus with respect to the separation distance L_s for the model system.

8.4 Tilt Model Validation

As a validation for the self-assembly modeling which suggested that two assembling particles tilt toward each other when in close proximity, particles fabricated from silicon wafers were assembled at a water and air interface.

8.4.1 Experimental

The experimental setup is shown in Figure 8.10. The chamber was constructed using glass slides. The working fluid was HPLC grade water. The density of the water was assumed to be 1000 Kg/m^3. The surface tension of

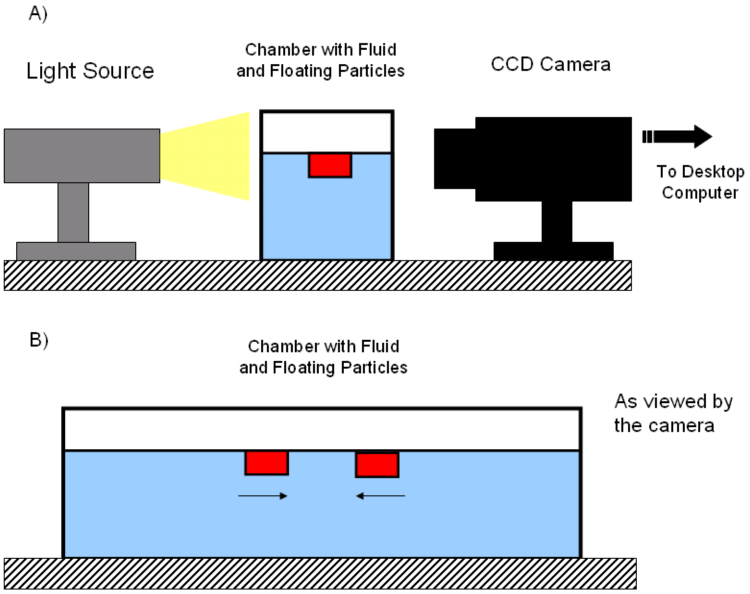

Figure 8.10: Schematic of the tilt measurement experimental setup. A) The setup consists of a illumination light source, fluid chamber containing the floating particles, and camera. B) Pictorial representation of the chamber as viewed by the camera.

was determined to be 0.075 N/m using a Rame-Hart Model 100 goniometer and the pendant drop method. A Sony XCD-X710 CCD camera with the field of view positioned at the air-water interface was used for imaging.

The floating particles were fabricated from Si wafers. Si was selected as the material because it is both denser than water ($\rho = 2300$ Kg/m^3) and forms a wetting angle with water. An Si wafer was cut into desired sizes by using a Disco 321 wafer dicing saw. The particles had a thickness of 0.57 mm. One dimension of the particles was fixed to 6.10 mm while the second dimension was varied from 2.37 mm to 30.0 mm. Sample particles are shown in Figure 8.11.

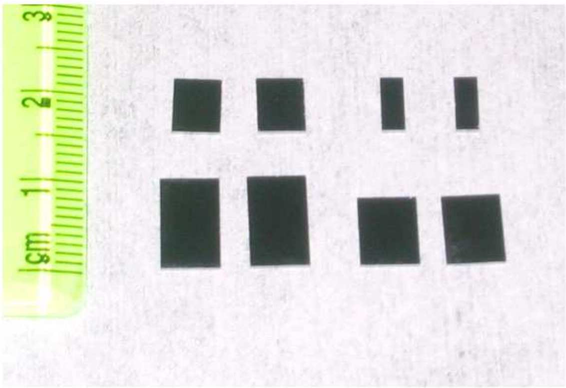

Figure 8.11: Sample diced Si particles.

A reference measurement was performed by first placing a single particle onto the air/water interface. After the surface has equilibrated, an image of the single particle was captured. A sample image is shown in Figure 8.12. The reference angle as compared to the axes of the image was determined

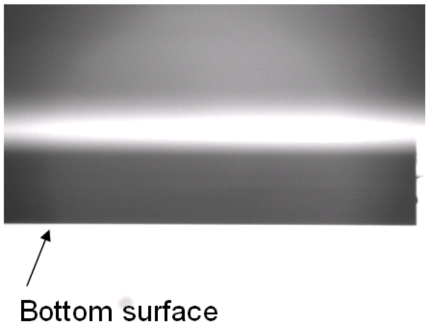

Figure 8.12: One particle floating at the air/water interface, this image is used for the reference angle measurement.

from the bottom surface of the particle using the “Straight Edge Detection Tool” function in the commercially available NI Vision Assistant software. The function detects straight lines in a region of interest and fits an equation using the coordinate system to calculate the tilt angle of that line. Since the software used the CCD sensor pixels as the reference axis, a baseline image of a particle that was not tilted was required to correct for any offset in alignment between the camera and the interface. The measurement from this image served as the baseline for comparison with subsequent images of tilted particles and compensates for any angle skewing of the setup.

A second particle of the same dimensions as the first was subsequently added to the interface. The two particles were allowed to assemble and an image was acquired. A sample image is shown in Figure 8.13. The particles were then rotated 90 ° and allowed to reassemble. It should be noted that the particles are not infinitely long as described in previous derivations. A third dimension “L_{depth}” was introduced to describe the length of the particle

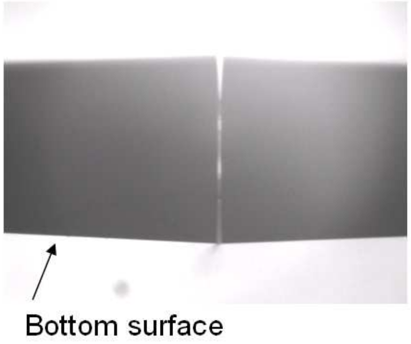

Figure 8.13: Two particles floating and assembled at the air/water interface.

into/out of the page. The assembled image was acquired. This process was repeated for all pairings of dimensions. A sample image of the edge detection is shown in Figure 8.14.

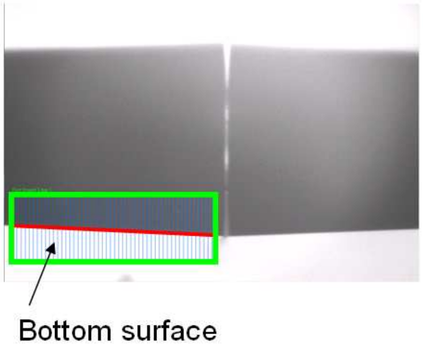

Figure 8.14: Image of two particles floating and assembled at the air/water interface and demonstrates the post-processing using the straight edge detection tool.

To generate the modeling results for comparison, the physical properties of the water and Si particle system was used as inputs to the tilt solver described in the previous section.

8.4.2 Results and Discussion

For each dimension pairing, the tilt angle was measured at four regions of interest – at the ends and the center (as defined by where the two particles meet) of both the left and right particles. This was accomplished by acquiring three images as shown in Figure 8.15. The measured angles after offset correction are shown in Table 8.2. Table 8.2 shows that the measured angles had good agreement between the left and the right particle. The tilt angles increased as the L_{depth} increased. Increasing the L_{depth} also increased the capillary force contribution from edges constituting the inner and outer L_{depth}. This also increased the dependence on the changing contact line angle and increased the tilt. The opposite was observed when L_{depth} was held constant. The largest deviation of 0.28 ° was observed for the L_{depth} = 6.10 mm and L_p = 30.0 mm case.

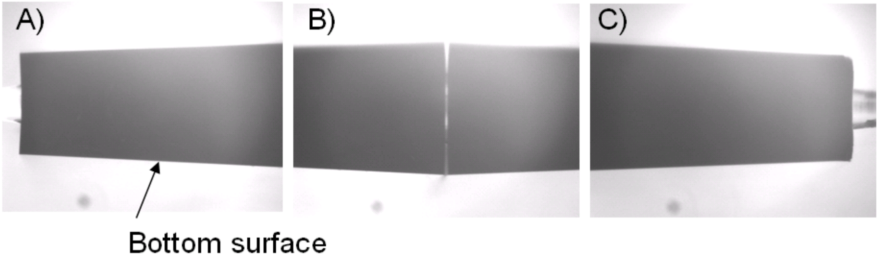

Figure 8.15: Sample images used in the tilt angle measurement. A) End of the left particle B) Center of the left and right particles C) End of the right particle

The tilt angles from the simulation are shown in Table 8.3. Table 4 shows that the model was able to predict the measured tilt angle within 15

Table 8.2: Measured tilt angles.

L_{depth} (mm)	L_p (mm)	Left Particle (°)		Right Particle (°)		Average (°)	Stdev (°)
		End	Center	Center	End		
2.37	6.10	0.96	0.94	0.89	1.01	0.95	0.050
5.00	6.10	1.50	1.42	1.42	1.51	1.46	0.049
7.50	6.10	1.84	1.76	1.73	1.88	1.80	0.069
10.0	6.10	2.00	1.98	2.01	2.08	2.02	0.043
30.0	6.10	2.57	2.58	2.47	2.48	2.52	0.058
6.10	2.37	2.00	1.90	2.05	2.03	1.99	0.067
6.10	5.00	1.82	1.67	1.74	1.85	1.77	0.081
6.10	7.50	1.40	1.30	1.33	1.47	1.38	0.076
6.10	10.0	1.14	1.08	1.01	1.10	1.08	0.054
6.10	30.0	0.25	0.08	-0.03	0.23	0.13	0.132

Table 8.3: Comparison of measured and model predicted tilt angles.

L_{depth} (mm)	Lp (mm)	Measured Average (°)	Model Predicted (°)	Error (%)
2.37	6.10	0.95	1.08	-13.9
5.00	6.10	1.46	1.63	-11.2
7.50	6.10	1.80	1.91	-6.20
10.0	6.10	2.02	2.10	-4.20
30.0	6.10	2.53	2.60	-3.10
6.10	2.37	2.00	2.12	-6.30
6.10	5.00	1.77	1.94	-9.60
6.10	7.50	1.38	1.56	-13.1
6.10	10.0	1.08	1.22	-13.0
6.10	30.0	0.13	0.28	-115

% error in most cases. The results are better visualized in Figures 8.16 and 8.17. Similar to the experimental trend, the tilt angles increased as the L_{depth}

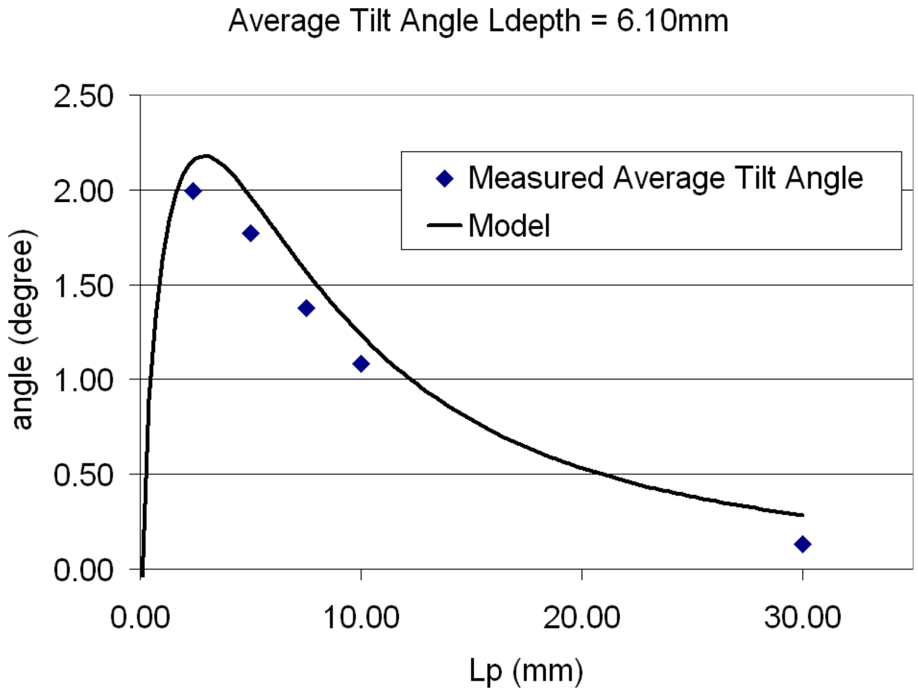

Figure 8.16: Comparison of the measured and model predicted tilt angles with constant $L_{depth} = 6.10$ mm

increased. The agreement of the model with the experimental data suggests that the model is able to describe the behavior of the interface and particles during assembly. The results of the model were used to calculate the forces acting on the particles during assembly.

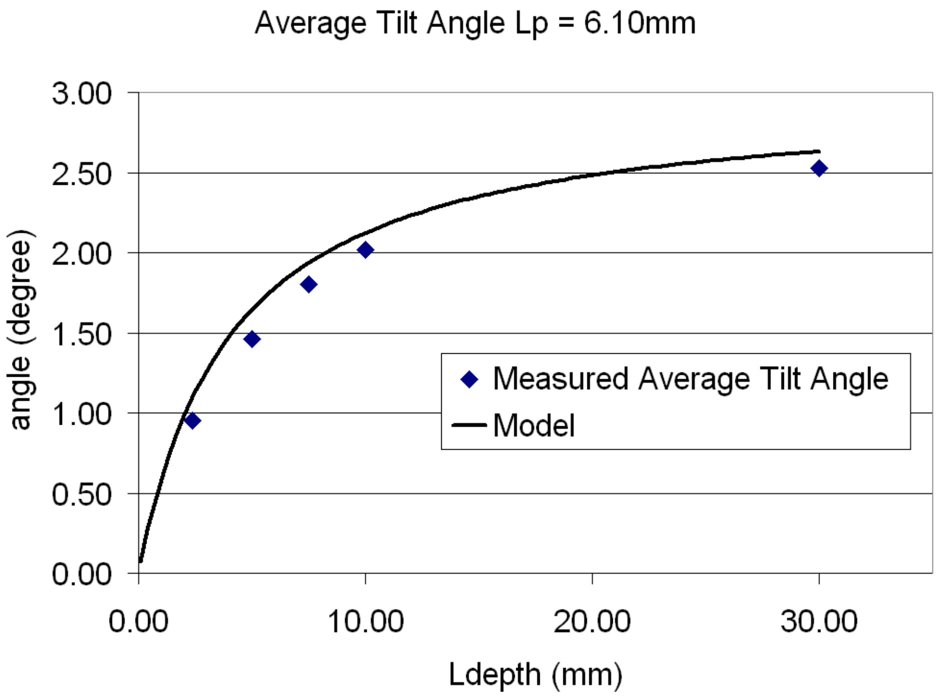

Figure 8.17: Comparison of the measured and model predicted tilt angles with constant $L_p = 6.10$ mm

8.5 Modeling the Self-assembly due to Lateral Capillary Interactions

The vertical and torque balance developed in the flotation model was able to describe the shape of the meniscus and spatial orientation of two particles in close proximity. This information is used to calculate the horizontal forces acting on the particles during assembly. As mentioned, the assembly is due to a combination of the lateral capillary and hydrodynamic pressure forces attracting the particles as a function of the separation distance. This attractive force per unit width can be written as the following

$$F_{attractive} = F_{cap,h} + F_{m,h}. \tag{8.11}$$

The lateral capillary component is given by

$$F_{cap,h} = \gamma \left(\cos\left(\theta_{c,i}\right) - \cos\left(\theta_{c,o}\right) \right). \tag{8.12}$$

The hydrodynamic pressure component per unit width is given by

$$\begin{aligned} F_{m,h} = \Delta P = \int P_{outer}\, dh - \int P_{inner}\, dh \\ = \rho_L g \left[\frac{\left(h_{o,p} + H\cos\alpha + L_p \sin\alpha\right)^2}{2} - \frac{\left(h_{i,p} + H\cos\alpha\right)^2}{2} + h_{i,m}\left(H + h_{i,m}\right) \right], \\ \text{where} \qquad h_m = h_i(x=0) = \frac{h_{i,p}}{cosh(qL_s)}. \end{aligned} \tag{8.13}$$

The forces were used in a rigid body dynamics simulation to model the assembly of cylindrical disks floating at the air-water interface. Cylindrical disks were selected to simplify the geometry of the system.

8.6 Potential Applications in Directed-Assembly

The assembly process described thus far is non-specific and can be susceptible to locally metastable configurations with short range order. It was proposed that specific or directed assembly may be achieved through the addition of an external agitation or "repulsive" force to counteract the attractive lateral capillary forces and a tunable binding force between particular species such that desired pairings have higher binding force than others. The forces can be adjusted so that the repulsive force is on the same order as the attractive forces where the particles can freely assemble or disassemble. The system is then able to sample different configurations. The binding force will allow desired pairs to have higher binding affinities and have increased probability of staying attached compared to other non specific pairings.

The concept of directed-assembly was explored through experiment by Dr. Peter Carmichael with polycarbonate squares floating at the air-water interface and is briefly described here. Five one inch polycarbonate squares were used, each was marked with one of the letters T, E, X, A, or S. The goal was to start from a random configuration and get the squares to assemble the word TEXAS in sequence. Magnets affixed into predrilled holes in the squares provided the adjustable binding forces between the particles. The pair-wise binding affinities were adjusted by manipulating the north/south encoding shown in Figure 8.18.

The experimental setup is shown in Figure 8.19. A cylindrical dish containing water and the polycarbonate squares was placed onto an orbital

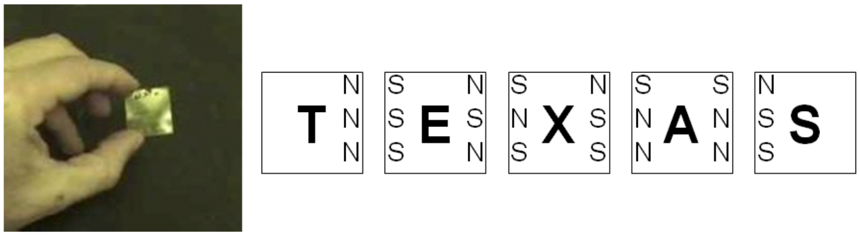

Figure 8.18: Polycarbonate square and the magnet encoding scheme used in the directed assembly experiment. *(Courtesy of Dr. Peter Carmichael)*

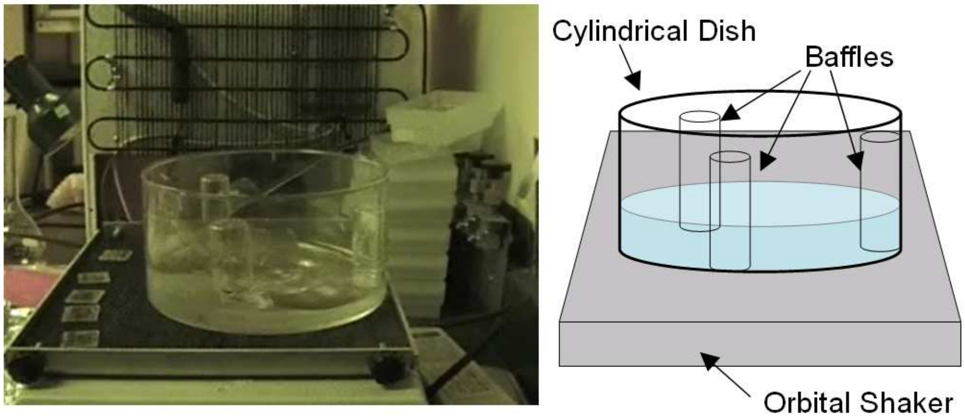

Figure 8.19: Experimental setup for the directed assembly of magnet-encoded polycarbonate squares. *(Courtesy of Dr. Peter Carmichael)*

shaker which provided the repulsive force by generating fluid flow in the system. Baffles were added to increase the complexity of the flow patterns. A video camera was placed above the dish to capture the configuration of the squares. Initially, the squares were in a random configuration as shown in Figure 8.20. The assembly of the particles was controlled by manipulating the rotation rate of the orbital shaker. At low rotation rates, the agitation force is not enough to overcome the attractive lateral capillary forces. Particles may be trapped in metastable configurations that are not the most favorable pairing. Conversely, at high rotation rates, the agitation force overcomes the binding forces such that even the most favorable pairings will separate. At the optimal range of rotation speeds where the attractive and repulsive forces are balanced, the system was able to assemble into the desired T-E-X-A-S sequence as shown in Figure 8.21.

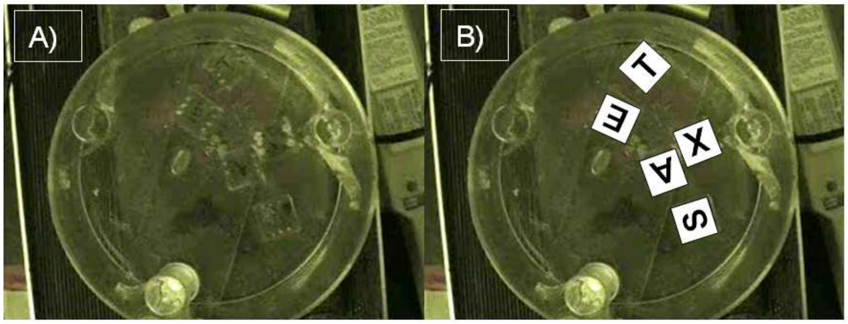

Figure 8.20: A) Configuration of magnet-encoded polycarbonate squares prior to assembly. B) Pictorial representation of the polycaronate squares superimposed to enhance contrast. *(Courtesy of Dr. Peter Carmichael)*

The polycarbonate/magnet system demonstrated the possibility for directed self-assembly using the correct balance of attractive, binding, and re-

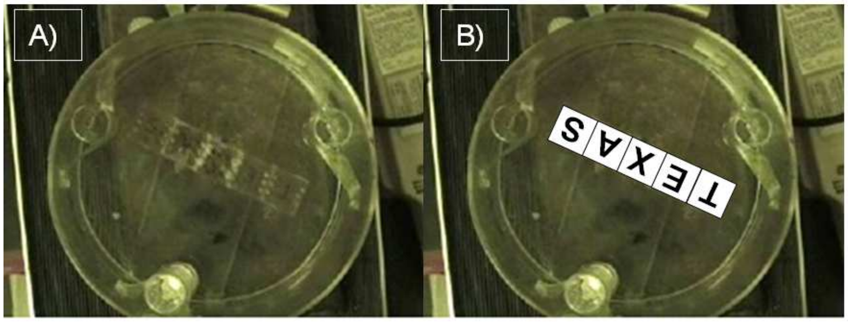

Figure 8.21: A) Configuration of magnet-encoded polycarbonate squares after assembly. B) Pictorial representation of the polycaronate squares superimposed to enhance contrast. *(Courtesy of Dr. Peter Carmichael)*

pulsive forces. However, the number of different pair-wise interactions, and consequently, the sequence length, of the system was limited by the binary response (north or south) of the magnets. If the pair-wise binding affinities can be performed with more complex encoding schemes such as DNA or proteins, the sequence length can also be increased leading to more complex structures.

8.7 Conclusions

The system of equations developed was able to describe the flotation of objects which are denser than the supporting fluid and have a wetting contact angle with the fluid. When two objects are in close proximity, the contact line angles change to maintain a smooth curvature which causes the particles to tilt. Simulations showed that the tilt angle of the particles decreased with increasing γ but increased with increasing ρ_p to balance the torque. Increase in L_p caused the tilt angle to decrease in both cases. Understanding the behavior of the particles will aid the calculation of the lateral capillary forces involved in the assembly, and lead to the eventual full scale modeling of the self-assembly dynamics. The concept of directed-assembly was also demonstrated through experiment. Although the directed self-assembly was demonstrated on macro scaled-objects, the force balance concept is also applicable objects at other size scales. An understanding of the dynamic interactions of the attractive, repulsive and binding forces can guide in the design of assembly systems.

Chapter 9

Pattern Recognition of Shape-Encoded Biosensors

9.1 Introduction

The design of the MUFFINS platform is intended to provide a method for mass-production of low-cost sensors. The use of photolithography to fabricate the individual sensors affords great flexibility in the types of patterns that can be generated – limited only by the photolithography process itself. As the number of sensor types in an array increased, a more sophisticated shape-encoding scheme was also required. Simple geometric shapes were chosen in early work [54] to demonstrate the efficacy of hydrogel-based sensors. Subsequently, a shape-encoding scheme along with a new pattern recognition algorithm was devised by Meiring [51] to handle the increased number of sensor types and to perform automated detection. As this is a crucial component of the MUFFINS platform, it was necessary to demonstrate the efficacy through a large-field detection experiment. This chapter presents the details of the demonstration.

9.2 Shape Definition

The shape-encoding scheme was originally described by Meiring [51], and is briefly included here for completeness. The dot-matrix shape-encoding scheme is shown in Figure 9.1 and is comprised of dot patterns (in the form of holes) that uniquely code for the sensor function. This arrangement enables large catalogs of shapes to be built quickly and systematically. Each "coding" dot represents a 0 or 1 in a binary number, providing for a large number of unique possibilities, e.g. up to 2^{25} ($> 3.3 \times 10^7$ combinations) distinct arrays can be created with the 5×5 pattern shown in Figure 9.1. In general, the

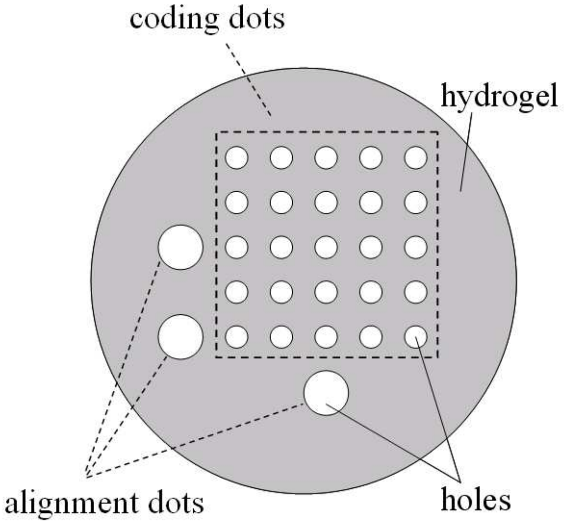

Figure 9.1: Shape encoding system used to identify each hydrogel sensor. The 5×5 array of small holes or coding dots represents a unique binary code for each sensor type. The three large holes or alignment dots are used to identify the rotation and orientation of the sensor in the randomly assembled array

number of distinct arrays is defined by

$$n_{arrays} = 2^{(n_R \times n_C)}, \tag{9.1}$$

where n_R and n_C refer to the number of rows and columns in the coding array, respectively. In addition to the coding dots, the encoding scheme also includes three larger alignment dots. These dots impart "chirality" to the sensors and are used to identify the rotation and orientation of individual sensors. These alignment dots are necessary since the assembly process deposits the sensors in the array randomly. To facilitate assembly, all sensors are given an outer circular shape, providing the necessary shape homogeneity described above. This new system enables large assays to be conducted and rapidly identified with a pattern recognition algorithm.

The positions of the alignment dots relative to each other and to the coding array were chosen to convey information to the software about the position and nature of the coding array. As shown in Figure 9.2, the alignment dots (numbered 1 to 3) are placed in specific sites relative to the boundaries of the coding array. The centers of dots 1 and 3 are placed on the horizontal and vertical axes Ax_1 and Ay_2, respectively, running through the center of the dot array. The center of dot 2 is placed on the horizontal axis Ax_2 passing through the bottom row of the array. The distance between the alignment dots and the array (d_a) is the made constant for dots 1-3. Using these relationships, the coordinates of each coding dot can be calculated. Given the alignment dot coordinates $(x_1, y_1), (x_2, y_2)$, and (x_3, y_3) for dots 1-3 with rotation and orien-

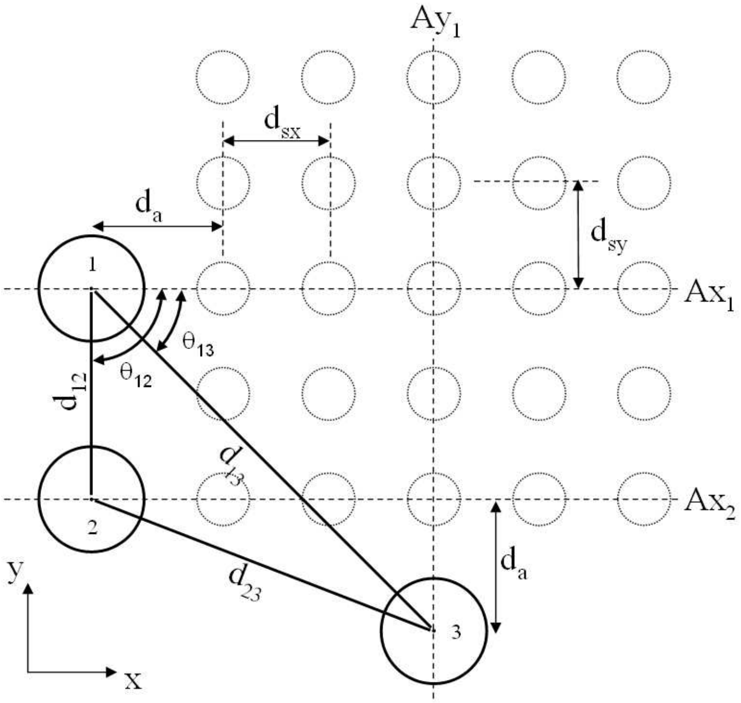

Figure 9.2: Schematic representation of the relationships between the alignment dots and the coding dot array

tation as in Figure 9.2, and a given distance d_a, a dot array can constructed with the following equations,

$$d_{sx} = 2 \cdot \frac{(x_3 - x_1 - d_a)}{n_R - 1} \tag{9.2}$$

$$d_{sy} = 2 \cdot \frac{(y_1 - y_2)}{n_C - 1} \tag{9.3}$$

$$x_{di} = x_1 + d_a + i \cdot d_{sx} \qquad i \in \{0, 1, 2, ..., n_C - 1\} \tag{9.4}$$

$$y_{dj} = y_2 + j \cdot d_{sy} \qquad j \in \{0, 1, 2, ..., n_R - 1\} \tag{9.5}$$

where d_{sx} and d_{sy} are the x and y spacings between the coding dots, and x_{di} and y_{dj} are the x- and y-coordinates of a coding dot in column i and row j. Although it is possible to use the size of the alignment dots to convey additional information, this approach was not taken because the dot sizes are highly sensitive to slight changes in experimental conditions, such as substrate reflectivity, photoinitiator concentration, exposure dose, *etc.* The relative center-to-center distances between the dots are conversely much more tolerant to experimental variation.

The distances and angles between the alignment dots (see the triangle overlayed on Figure 9.2) are critical and must be known to the pattern recognition software. During recognition of the alignment dots, assignments of the numbers 1 to 3 are decided by comparing the distances d_{12}, d_{13}, and d_{23} (see below). The distances must be differentiated within a tolerance limit, so it is important that the difference between d_{13} and d_{23} is sufficiently large. For example, if the tolerance is 10%, the distance $d_{13} - 10\%$ should be greater than $d_{23} + 10\%$. Recognition errors may occur if these two distances are confused.

9.3 Getting Large-Field Images

Due to the limited field of view of the microscope at the required magnification, early imaging of the array entailed capturing small sections of an array at a time and later stitching the images together. The stitching process often introduced unwanted artifacts at the image boundaries which is further complicated by barrel distortion effects near the corners of the images. A sample image of a stitched image is shown in Figure 9.3. A fluorescent imaging system capable of acquiring a large field of view ($\sim$ 0.5 in × 1 in) with sub 10 μm resolution would be required to properly image the sensors.

The stitching issues were resolved with the use of a Genepix 6000B (Molecular Devices, Sunnyvale, CA) full-field fluorescence capable microarray scanner ("scanner"). Although the scanner is able to gather a full-field image, it still suffered from two drawbacks. First, the scanner is only capable of detecting fluorescent images in two wavelength ranges (532 nm and 635 nm excitation wavelengths). This means that observing the conventional bright-field images captured using white light on an optical microscope was not possible.

Second, the scanner had a suboptimal focus setup for imaging the MUFFINS sensors. The default focus plane of the scanner is set at the top of the stage, or the bottom of the substrate (in this case a standard 1 in × 3 in

Figure 9.3: Sample of fluorescent images captured with optical microscope and stitched to form a composite image of the array.

glass slide with 1 mm thickness) resting on the stage. This setting is typical for spot-deposited microarrays as the slides are imaged spot-side down. However, this setup does not work for MUFFINS imaging as the sensors are usually placed on the top side of a glass slide. Because they are weakly adhered to the glass slide surface, imaging with the sensors-side down risks detachment of the sensors into the scanner. Additionally, the sensors are usually immersed in a liquid media during imaging to prevent dehydration. Thus, the MUFFINS sensors must be imaged on the top side of the glass slide. This posed another issue as the scanner only has a focus range of -50 to 200 μm (0 μm is the defined at the stage/substrate interface) and is not able to penetrate the 1 mm thick glass slide.

The bright-field issue was resolved by incorporating an additional "background" DNA probe sequence into each sensor. During hybridization, a separate target sequence complementary to the background was added to the target mixture. The target mixture refers to the solution containing buffer and dye-modified DNA sequences that are complementary to specific DNA probe sequences embedded in the sensors. The background target sequence was modified with a different fluorophore (Cy5) than the other target sequences that responds in the 635 nm spectral range. This setup allows the 635 nm range to serve as the background bright-field wavelength while reserving the 532 nm range for target detection.

The focus issue was resolved by the construction of a customized sample holder as shown in Figure 9.4. The sample holder was constructed by drilling

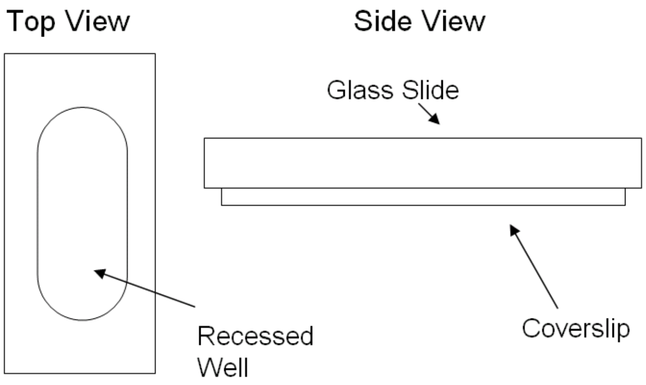

Figure 9.4: Custom slide for MUFFINS imaging in an microarray scanner

a series of openings in the center of a standard glass slide. A 22 mm × 45 mm No. 1 coverslip was trimmed to size and glued on the bottom side of the glass slide. The edges of the well were sealed with glue to prevent leakage. This arrangement created a recessed well in which the MUFFINS sensors could be placed along with liquid media. More importantly, attaching the coverslip to the underside of the slide also moved the sensors into the focal range of the tool. The aforementioned adjustments enabled high resolution large-field imaging of MUFFINS sensors.

9.4 Pattern Recognition Algorithm

The initial implementation of the pattern recognition algorithm was devised by Meiring [51] and was able to process images captured from an optical fluorescence microscope. Upon switching to the microarray scanner, however, a decrease in the recognition efficiency of the algorithm was observed. Specifically, most of the recognition errors were due to sensor-to-sensor nonuniform intensity values and skewing of the coding dot array relative to the alignment dots. Depending on the binding affinity and concentration of various target and probe sequences, the observed fluorescence was much higher for certain sensor types. In some cases, the coding dots of some sensor types were near the intensity of the fluorescing areas of other sensors. The non-uniform intensity issues were perhaps further exacerbated by the increased sensitivity and decreased depth-of-focus of the microarray scanner. To resolve these recognition issues, a new version of the pattern recognition algorithm based on the shape-encoding scheme described in Section 9.2 and some elements of the previous implementation by Meiring was devised. The details of the new version are described below.

9.4.1 Intensity Definition

In this document, "bright" regions refer to sensors that have positive response or fluorescence while "dark" regions refer to the background, non fluorescing sensors, and holes representing the alignment and coding dots. The intensity values are scaled between zero and one such that after binarization, bright and dark regions are assigned values of one and zero, respectively.

9.4.2 Preprocessing

Several steps are performed by the software to generate a high quality binary image input. Prior to binarization, the color image is first converted to grayscale by calculating the overall intensity magnitude using the three individual RGB intensity values in the following manner

$$I = \sqrt{I_{Red}^2 + I_{Green}^2 + I_{Blue}^2}. \tag{9.6}$$

A variety of binarization techniques were tested. A global minimum threshold (T_{MIN}) is used to filter out low level intensity values that may contribute to noise. But because the micrographs generally exhibit considerable non-uniform intensity variations from sensor to sensor, a global thresholding algorithm gives poor results if used to perform segmentation of the alignment and coding dots inside each sensor. The intensity variations are caused by differences in binding affinities of the complementary fluorescently labeled DNA sequence. In addition, some sensors display low contrast between the holes and the fluorescing sensor or "graying" of holes within sensors. Low global thresholds are ineffective in resolving gray holes while high global thresholds inaccurately wash out sensors with lower average intensities. The non-uniform intensity variations suggest that local thresholding techniques were more appropriate. As such, the preprocessing step only applied the global minimum thresholding binarization to facilitate individual sensors recognition. A second local thresholding and binarization step, described below, was performed prior to alignment and coding dot recognition.

9.4.3 Sensor Recognition

After preprocessing, the individual circular sensors are detected using the Hough circle detection algorithm by D. H. Ballard [2]. A range of radius guesses (R_{guess}) is given to the algorithm which then calculates the possible center locations. The coordinates and frequency of occurrence of the locations are stored, and only locations with frequency counts above a specified threshold (T_{Hist}) are recognized as centers. The center coordinates and the median of radius guesses are subsequently used to extract individual sensors for recognition.

9.4.4 Local Thresholding and Binarization

In order to resolve the alignment and coding dots within each sensor after the sensor recognition step, a second local thresholding and binarization was necessary. However, poor results were observed when using direct local thresholding based on mean intensity by applying the Sauvola method [66]. Acceptable results were obtained via a two-step method that first compares the intensity standard deviation within a local window (3 × 3 pixels) to a defined standard deviation threshold (T_σ). For a window of size $w \times w$ centered at (i, j), the binarization function $B(i, j)$ can be summarized as,

$$B(i,j) = \begin{cases} 0 & \text{if} \quad \sigma_{w\times w} \geq T_\sigma \\ 0 & \text{if} \quad \sigma_{w\times w}(i,j) < T_\sigma \text{ and } m_{w\times w}(i,j) < I_s \\ 1 & \text{if} \quad \sigma_{w\times w}(i,j) < T_\sigma \text{ and } m_{w\times w}(i,j) \geq I_s \end{cases}, \tag{9.7}$$

where $\sigma_{w\times w}$ is the local standard deviation of the window, $m_{w\times w}$ is the local mean of the window, and I_s is the mean sensor intensity. A local standard deviation that is above the threshold suggests that the pixel is an edge point and the pixel value is set to zero. Points that have local standard deviation below the threshold are binarized by comparing the local mean intensity to the sensor mean intensity. The sensor mean intensity is calculated by averaging the intensities inside the entire active sensor under investigation. Pixel is set to one if the local mean intensity is greater than the sensor mean intensity or to zero if less than the sensor mean. The method is less susceptible to intensity variations from feature to feature, but it is prone to falsely set the intensity values in the centers of the dots to one if the holes are gray (see Figure 9.5). The center points inside holes usually have low local standard deviation values because they are not close to the edge. Therefore, binarization is done using the local mean intensity which may lead to formation of rings instead of holes if the local mean intensity value is larger than the sensor mean intensity. The "ring effect" is corrected with a subsequent algorithm that removes the falsely binarized centers. For a window centered at (i, j) of radius r_r and size $w_r = 2r_r + 1$, we have

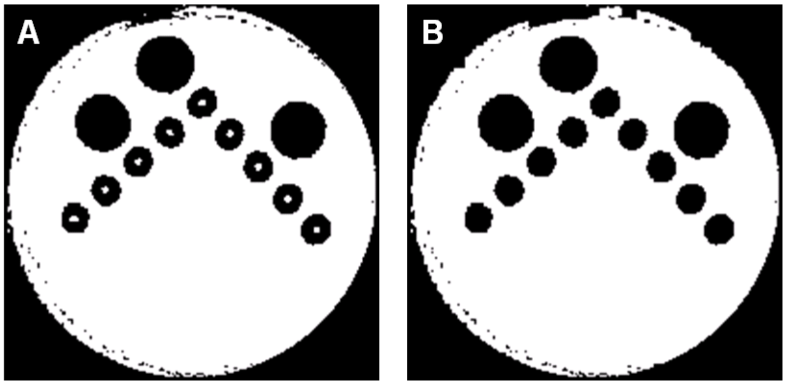

Figure 9.5: A) Image showing the "ring effect" observed after local standard deviation thresholding B) Corrected image after ring removal

$$S = \{-r_r, +r_r\} \tag{9.8}$$

$$I_C(i,j) = \sum_{m \in S} \sum_{n \in S} I_{m,n}(i,j) \tag{9.9}$$

$$R_{w_r \times w_r}(i,j) = \begin{cases} 0 & \text{if} \quad I_C(i,j) = 0 \\ 1 & \text{if} \quad I_C(i,j) > 0 \end{cases}, \tag{9.10}$$

where I_C is the sum of the intensities of the window's corner pixels and $R_{w_r \times w_r}$ is the set of all pixels in the window. This algorithm examines the intensity values at the four corners of a moving square window in which the size is specified to fall within the "ring" range. If all of the corner values are zero, the algorithm replaces all values within the square with zeros. The software is able to accept multiple input w_r values within a single run to remove rings of various sizes.

9.4.5 Alignment and Coding Dot Shape Recognition

Since the alignment and coding dots are circular by design, their detection could theoretically be performed using the Hough circle detector. However, the use of the Hough circle detector proved to be laborious and computationally intensive. The sheer number of alignment and coding dots within one image increases the computation time required in calculating possible center points and also makes verification difficult.

Compared to individual sensors which contain both bright and dark regions formed by the alignment and coding dots, the alignment and coding dots themselves are less complex — comprised of bright circular shapes with only dark interiors. Thus, dot detection does not require the more complex

Hough circle detector, but rather can be achieved with a simpler algorithm, which checks for bright regions that have dark points within a prescribed radius as shown in Figure 9.6.

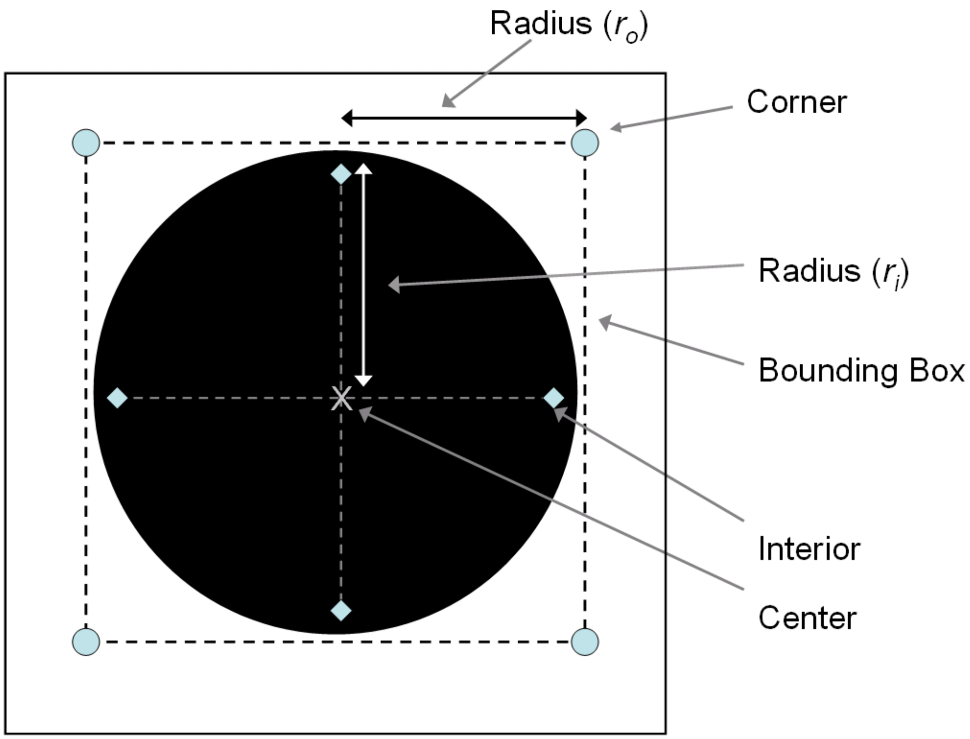

Figure 9.6: Illustration describing the alignment and coding dot detection.

An algorithm similar to the ring removal first examines the corners of a moving square window. For a window centered at (i, j) of outer radius r_o, first the corner intensity sum I_C is calculated using Equations 9.8-9.10. The radius of the inner region is specified by r_i. Then dots are found using the following equations

$$U = \{-r_i, +r_i\} \tag{9.11}$$

$$I_H = \sum_{m \in U} I_{m,0}(i,j) + \sum_{n \in U} I_{0,n}(i,j) \tag{9.12}$$

$$H_d = \{i, j \mid I_C(i,j) = 4, \text{ and } I_H(i,j) = 0\}, \tag{9.13}$$

where I_H is the sum of four interior intensities in the circle of radius r_i, and H_d is the set of (i,j) coordinates that meet the given criterion for radius set r_o and r_i. In this case, the algorithm checks to see if the corners are bright. If so, the algorithm then checks to see if the interior is dark by checking the intensity values at points within a specified radius r_i designated by the diamonds. Only center points that satisfy all criteria are marked as dots of a particular size. This process is used to detect both the alignment and coding dots; the two types are differentiated by the size of the radius and bounding box. The software is able to accept multiple sets of input r_o and r_i values within a single run when searching for either the alignment or coding dots.

9.4.6 Alignment Dot Recognition

Alignment dots are located by searching for sets of three dots that match the specified radius sizes. The center-to-center distances between the dots are calculated by pairing up two dots at a time for all pair-wise combinations. The calculated distances are sorted and used in the assignment of the numbered dots from 1 to 3 that form the triangle in Figure 9.2. A unit vector is subsequently calculated from dot 2 to dot 1, and used to determine the orientation of the sensor. These angles are "absolute" in that they are always referenced to a vertical axis passing through the center of dot 2. Inversion can be determined by computing the angle from d_{12} to d_{23}. If the angle is negative (counterclockwise direction), then the sensor is inverted, and the pattern is mirrored. Using the orientation angle, the image is rotated to the 'upright' position such that the unit vector from dot 2 to dot 1 is pointing in the positive vertical axis.

9.4.7 Coding Dot Detection

For each sensor, a search is conducted for the coding dots. The search begins by extracting the region of interest containing the coding dots which is calculated using Equations 9.2 to 9.5 with additional padding pixels on the edges. The coding dots are then found using the same technique as described for the alignment dots with the exception of a smaller specified radius and bounding box width.

9.4.8 Dot Array Skew Detection and Correction

By design, the orientation of the sensors and thus the coding dot array should be determined by the alignment dots. However, in practice, it was found that orientation of the coding dot array can sometimes be skewed slightly from the alignment dots. These discrepancies are caused by minute errors in the detection of the alignment dots, errors in the fabrication process, or deformations experienced by the sensors during imaging or assembly. The skewing angle, though small, is often large enough to cause errors in recognition by shifting the dot into an adjacent grid point or entirely out of the area of interest and needs to be corrected. The skewing is corrected by first detecting the skew angle using an algorithm based on the Hough Transform [61], not to be confused with the Hough circle detector, and then rotating the extracted region of interest appropriately to correct for the skewing. The maximum angle rotation tolerance was set at $+/-2°$. This tolerance was necessary since some features such as the letter X have more coding dots in the diagonal directions. In this case, the algorithm could incorrectly recognize the diagonal as the main axis, and over rotate the image.

9.4.9 Coding Dot Array Recognition

Once the coding dots are properly oriented, the image is divided into grids with dimensions as defined by Equations 9.2 to 9.5 depending on the number of rows and columns specified (5×5 in this case). If a coding dot is found within a grid, the bit for the grid point denoted by the row and column number is set to 1; otherwise it is set to 0. The recognition algorithm outputs a binary number sequence representing the result of the search. The number is cross-referenced with a predefined key to determine the identity of the sensor. A sample sensor pattern and corresponding binary number sequence is shown in Figure 9.7.

The preceding steps were implemented in a script using MATLAB

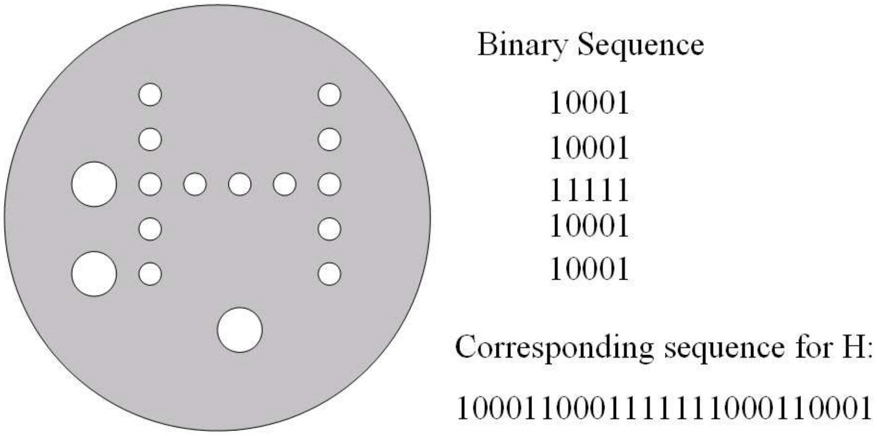

Figure 9.7: Sample image of the “H” sensor pattern and the corresponding binary number sequence.

R2006a with the image processing toolbox. The script accepts the relevant parameters specified in an input file and outputs a final “report” of the recognition results. Total processor time on large images on a fast computer is a few minutes. Switching to a compiled language and performing optimization of the algorithms would likely reduce the time significantly, should faster recognition be required.

9.5 Experimental

9.5.1 Masks

Mask patterns were designed with AutoCAD LE 2002 and fabricated as chromium on 5 in × 5 in soda lime glass by Advance Reproductions, Inc. Twenty-five 2 cm × 2 cm fields, each with a different dot pattern, were fabricated. The sensor patterns as printed on the mask had a 1 mm outer diameter, with 100 μm diameter alignment dots and 50 μm diameter coding dots. Each 4 cm^2 field contained 82 features. Fourteen fields with dot patterns in the form of various letters were used make the DNA sensors.

9.5.2 Materials

Poly(ethylene glycol) diacrylate (PEG-da) with a weight-average molecular weight of 10,000 was purchased from SunBio. All pre-polymer formulations are described in volume percents. Darocur 1173, a liquid, photoinitiated free-radical generator, was obtained from Ciba-Geigy. Functionalized single-stranded DNA sequences were purchased from Integrated DNA Technologies.

9.5.3 Pre-Polymer Formulations

Sensors for the assay were made from a pre-polymer solution consisting of 20 % PEG-da, 2 % Darocur 1173, and 78 % of a probe DNA mixture in DI water diluted to 10 μM probe and background DNA final concentration (see Table 9.1 for the shape assignment for each probe). In addition to the probe DNA, an additional background DNA sequence (5' - TGCCTGTTT - 3') designated 'BG' was added to each sensor. The complementary sequence to sequence BG was attached to a different fluorophore (Cy5) than the target sequences (Cy3) to allow for BG to aid in the illumination of the background bright-field image. The 'W' shape was reserved as an experimental negative control and was formulated with only the BG sequence.

Table 9.1: Sensor Loading Method.

Feature	Probe	DNA Sequence
V	1	5' - GTGCATGTT - 3'
X	2	5' - GTGCTTGTT - 3'
Y	3	5' - CGTATTTGTG - 3'
P	4	5' - TGCGTCTTT - 3'
R	5	5' - GCGTTTTTG - 3'
I	6	5' - GTGGTTGTG - 3'
K	7	5' - GTGCTTGTG - 3'
L	8	5' - GTTAGTGCC - 3'
M	9	5' - GTGTTGGTG - 3'
N	10	5' - GTGTTCGTG - 3'
Z	11	5' - GTGTTTATGC - 3'
U	12	5' - GTTTCTGCC - 3'
H	REF	5' - CGTGTTTGT - 3'
W	None	(only BG) N/A

9.5.4 Exposure Tool and Hydrogel Fabrication

Broadband ultraviolet radiation from a 200 W high-pressure mercury arc lamp (Oriel) was used for curing the pre-polymer. The bulb was housed in an Oriel shutter enclosure that collimated the radiation to approximately a 15 cm diameter area and filtered out wavelengths below 365 nm. The nominal intensity of the collimated light was 12.1 mW/cm^2, as measured by a Molectron PowerMax 5200 intensity meter. An Oriel 68810 arc lamp power supply, coupled with an Oriel 68705 igniter, was used to power the bulb. The shutter was controlled by an Oriel 8160 timer. Sensors were prepared by placing the pre-polymer solution between the photomask and a chrome coated plate with 0.25 mm thick cover slips acting as spacers. The curing dose was determined empirically to be 970 mJ/cm^2 based on the physical properties of the hydrogels and their shape under a microscope. Sensors were rinsed with DI water after exposure to remove any unreacted pre-polymer and stored until use in the hydrated state.

9.5.5 Hybridization Media Formulation

The DNA detection assay was conducted in a hybridization mixture composed of 200 μL of the following constituents in DI water: tris(hydroxymethyl)aminomethane (pH 7.6), NaCl, ethylenediaminetetraacetic acid (EDTA), formamide, Cy3 fluorescently labeled target DNA sequences, and Cy5 fluorescently labeled background DNA sequence (see Table 9.2). After hybridization, the sensors for the DNA assay were rinsed in a 2.5 M NaCl solution to remove unbound target DNA sequences.

Table 9.2: Target DNA Sequences.

Target Name	DNA Sequence
TGT 4	5' - /Cy3/ GCCACAAAGACGCAG - 3'
TGT 8	5' - /Cy3/ GGCACTAACACGCAC - 3'
TGT REF	5' - /Cy3/ GGCACAAACACGCAC - 3'
TGT BG	5' - /Cy5/ GGCACAAACAGGCAC - 3'

9.5.6 Imaging and Pattern Recognition

A GenePix 4000B microarray scanner from Molecular Devices was used for fluorescent imaging. The scanner was capable of capturing fluorescent images at 532 nm (Cy3) and 635 nm (Cy5) with 5 μm resolution. Fluorescent images were acquired at 532 nm and 635 nm. The image at the 532 nm wavelength was obtained to show the binding response to the target DNA sequences while the image at 635 nm wavelength was obtained as a bright-field image to show all sensors in the array. The images were processed using the methods and script described earlier. The relevant parameters are listed in the Appendix B.

9.6 Results and Discussion

Sensors with dots representing various letters were fabricated in batches and randomly assembled into an array. Each sensor type contained two types of single stranded DNA (loading dictated by Table 9.1), one for target sensing and one for background illumination, copolymerized into the hydrogel matrix via a 5' methacrylate functionality. The sensors were designed to register a positive, i.e. fluorescence signal, when complementary "target sequences" with a 5' Cy3 fluorescent tag or "background sequence" with a 5' Cy5 fluorescent tag bound to the corresponding probe sequences in the hydrogels. For each target listed in Table 9.2, the designation after the "TGT" represents the identification of the complementary probe sequence. The sensors were soaked overnight in a hybridization medium containing known target sequences. After hybridization, the sensors were rinsed twice for several hours in a salt solution containing no DNA, and then imaged on a fluorescent microarray scanner. The acquired images are shown in the Figure 9.8.

Figure 9.8 shows images acquired with 635 nm and 532 nm illumination

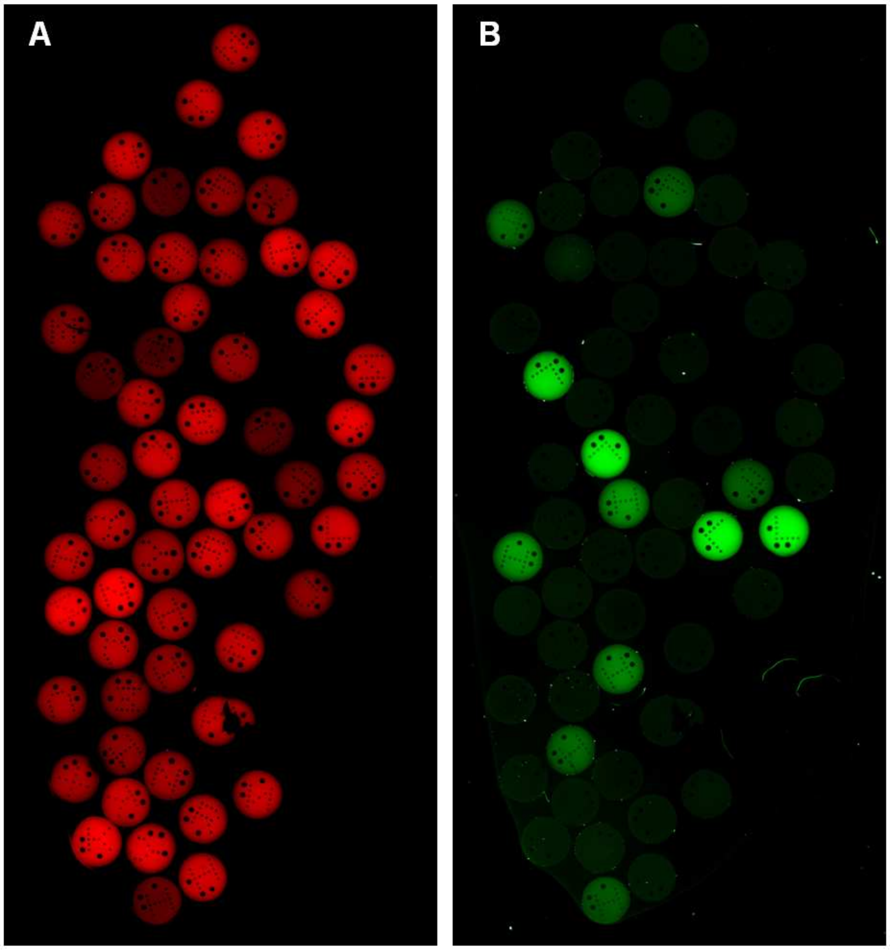

Figure 9.8: A) Bright-field background image showing fluorescence at 635nm B) Target image showing fluorescence at 532 nm.

and are designated “background image” and “target image”, respectively. Figure 9.8A shows that the use of the Cy5 labeled probe BG was able to provide a background bright-field like image that shows all the sensors while Figure 9.8B shows the specific binding of the fluorescently labeled complementary target sequences. A total of 57 fluorescing sensors are fully visible, *i.e.* the dot patterns are completely within the frame of the image. The target images shows that positive target fluorescence result was only observed for the 12 sensors which were comprised of P, L, and H features that corresponded to TGT 4, TGT 8, and TGT REF, respectively. In addition, no P, H, or L sensors were found to give negative results. These results, in conjunction with a non fluorescing negative control (sensor W), suggest the sensing experiment was successful. Pattern recognition was performed on the images. To demonstrate the recognition process, the sequence processing steps are shown in Figure 9.9. The results for the background and target images are shown in Figure 9.10 and Figure 9.11, respectively. Detailed reports of the pattern recognition runs are shown in Appendix B.

9.6.1 Background Image

Figure 9.10A shows the individual MUFFINS images extracted after grayscale conversion, global thresholding, and circular feature recognition. The standard deviation thresholding and binarization results are shown in Figure 9.10B. The results of the coding dot recognition are shown in Figure 9.10C. The software has rotated the image of each dot pattern to its upright and non-

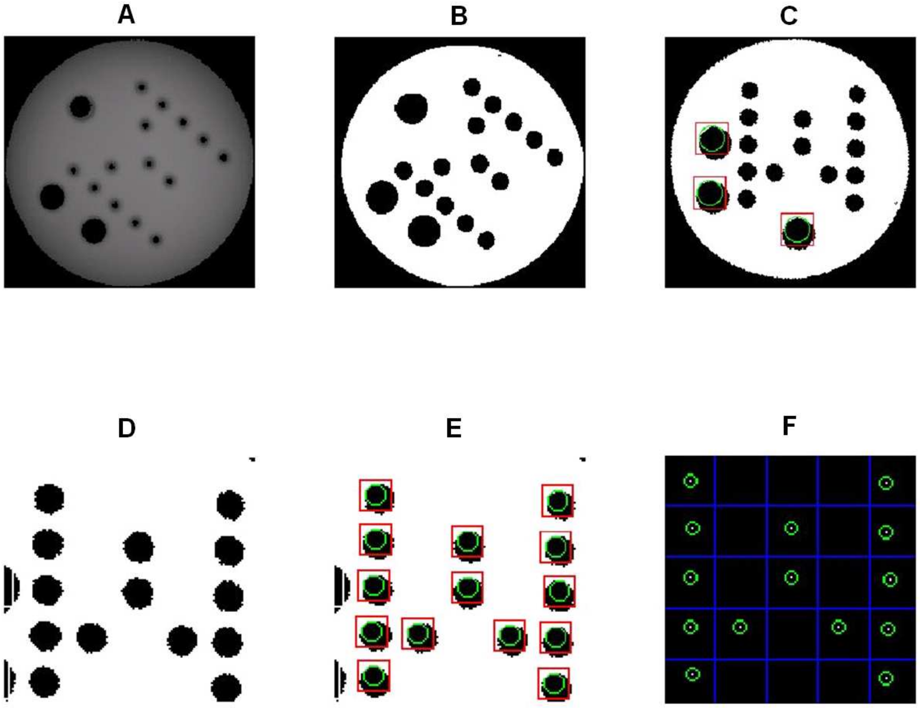

Figure 9.9: Pattern recognition processing steps: A) Extracted sensor image after grayscaling and global minimum thresholding B) Binarized image after local standard deviation thresholding and ring removal C) "Upright" image after rotation and inversion of the image D) Extracted region of interest containing the coding dot array E) Recognized coding dots after skew correction (1.06 °) F) Pattern found to be letter "W" after matching binary number with predefined key.

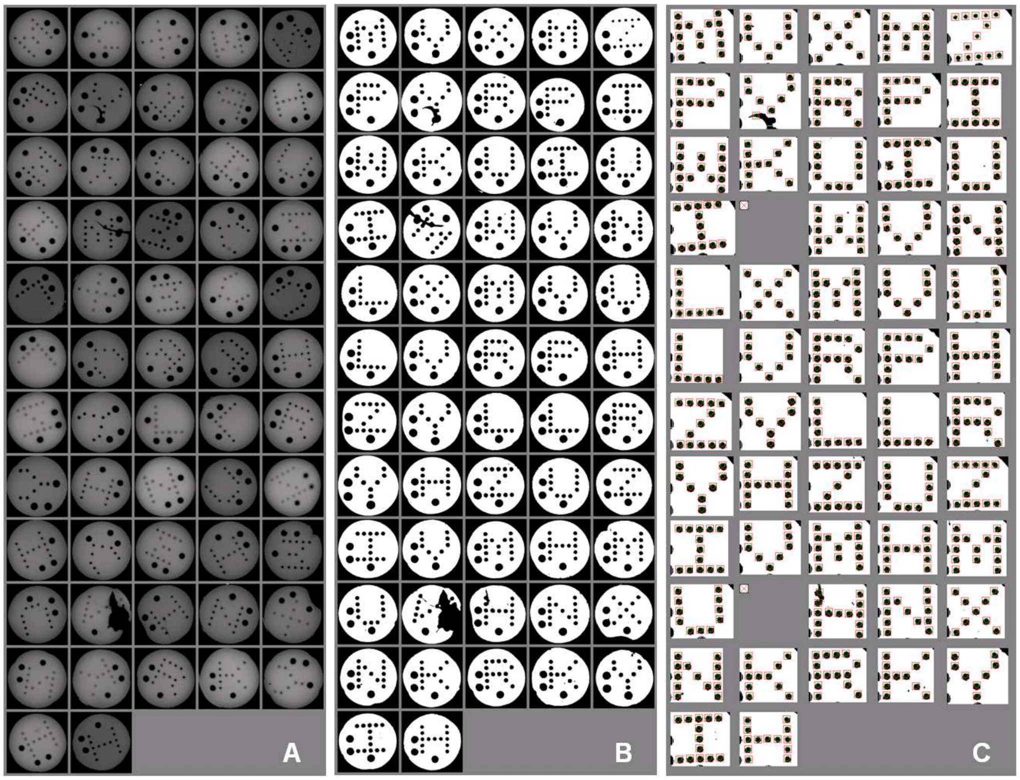

Figure 9.10: Shape recognition results for the background image (635 nm illumination). A) Fluorescent micrograph after grayscaling, circle feature recognition, and image extraction. B) Image after local standard deviation thresholding and binarization. C) Pattern recognition results, with recognized coding dots in red boxes.

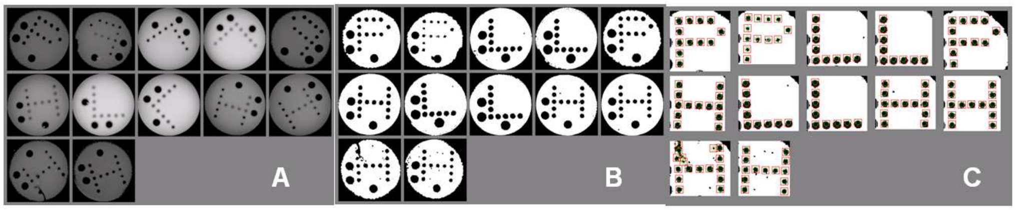

Figure 9.11: Shape recognition results for the target image (532 nm illumination): A) Fluorescent micrograph after grayscaling, circle feature recognition, and image extraction. B) Image after local standard deviation thresholding and binarization. C) Pattern recognition results, with recognized coding dots in red boxes.

mirrored position, and circled the coding dots that were recognized. Certain letter pairings such as "H" and "I", "N" and "Z", and "M" and "W" were explicitly selected because they form mirror images that can only be distinguished through the proper recognition of the alignment dots. The algorithm was able to distinguish all fourteen different coding dot patterns representing the letters. Of the 57 fluorescing sensors, four were recognized incorrectly (7.0 % failure rate). Three of the four errors, as shown in Figure 9.12, indicate that recognition failed due to defects and deformities present in the sensors, not to shortcomings in the pattern recognition code. The origin of these defects is not completely clear; however, they were most likely caused by debris on the mask, or stresses experienced during imaging. Ignoring the errors caused by defects, the recognition success rate was 98 %.

9.6.2 Target Image

Figure 9.11 shows that of the 12 fluorescing sensors one was recognized incorrectly, as shown in Figure 9.13, leading to a failure rate of 8.3 %. This

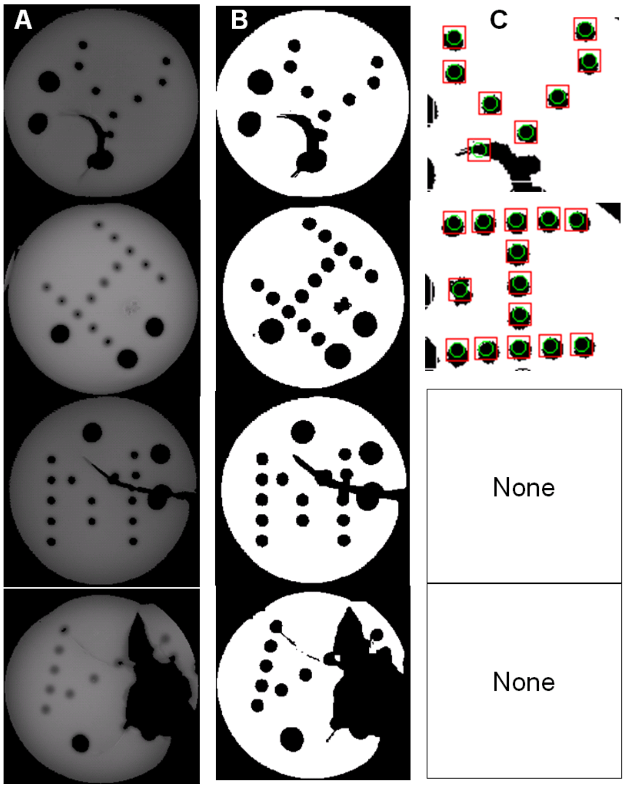

Figure 9.12: Recognition errors for background image (635 nm illumination): A) Original extracted image. B) Thresholded and binarized image. C) Recognition result.

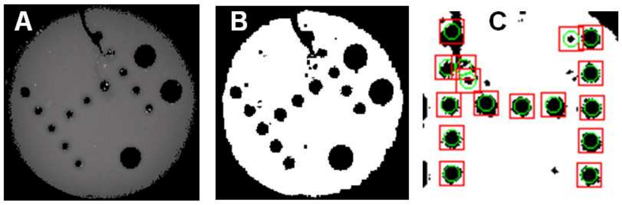

Figure 9.13: Recognition errors for target image (532 nm illumination): A) Original extracted image. B) Thresholded and binarized image. C) Recognition result.

failure rate is higher than the failure rate of the background image due to the smaller sample size of 12 versus 57. As in the errors in the background image, the observed error was mainly due to a physical deformity in the sensor; a crack extending from the edge of the sensor through one of the coding dots. If the defective sensor is excluded from the set, the success rate of recognition is 100 %.

The pattern recognition results show that the implemented algorithms had an average success rate of 93 %. However, most of the errors can be attributed to defects in the sensors originating from fabrication or handling, rather than limitations of the recognition software. Taking into account these sources of errors, i.e. excluding the defective sensors, the algorithm has an adjusted average success rate of 98 %.

The use of a local standard deviation threshold to segment the dark holes within each feature was effective in overcoming sensor-to-sensor intensity variations and also 'graying' of holes inside a sensor. The standard deviation threshold had to be set low enough to enable segmentation of the holes; however, thresholds that were too low caused dark spots or 'pits' to form in the sensor and led to errors in recognition. The Hough circle detector was able to successfully isolate each individual circular sensor, although the iterative process of generating the acceptable combination of initial radius guesses proved to be laborious. These difficulties arose due to the sensor-to-sensor intensity variations which caused the sensors to have different diameters after the initial global thresholding step.

The alignment and coding dots were successfully detected using the bounding box with embedded circle technique. Due to the variations in sizes of the dots from sensor to sensor, careful selection of the size of the bounding box and circle was critical to the process. The bounding box has to be large enough to include slightly larger dots but not so large that it would overlap with other dots. The radius of the embedded circle has to be small enough to sample the smaller dots but not so small that it causes the algorithm to accept erroneous points. The skewing discrepancies between alignment and coding dots were resolved with the implementation of skew detection and correction using the Hough Transform.

For the MUFFINS platform and the automated pattern recognition to be effectively used in the framework of biosensing, the sensor arraying and fabrication processes must be well controlled such that an optimal set of algorithm parameters will consistency produce a high success rate. Defects and debris in all steps of the process must also be reduced to prevent pattern recognition errors. Aside from the defects, other recognition difficulties were due to the sensor-to-sensor and within-sensor intensity variations. The low contrast between the sensor and the dots, *i.e.* ‘graying’ effect, can be attributed to incomplete rinsing of unbound fluorescent target DNA sequences which can diffuse into the holes during imaging. Contrast can be enhanced with additional rinsing of the sensors.

9.7 Conclusions

A successful pattern recognition and shape-encoding scheme for the MUFFINS biochip platform has been demonstrated. The shape encoding system, using dot patterns embedded in three dimensional hydrogels, has been designed to facilitate batch photolithography and automated pattern recognition, both key requirements for a cost-effective biochip. Software was written to perform the recognition, and was tested on an array. A high resolution fluorescence capable array scanner and modified sample holder was required to obtain the necessary large-field image. The results show that this system is quite viable with an 98 % recognition accuracy of the non-defective sensors.

Chapter 10

Demonstration of the Complete MUFFINS Platform: Biosensing, Multiplexing, Random Fabrication, and Automated Pattern Recognition

10.1 Introduction

The MUFFINS platform offers several advantageous features including increased biocompatibility from the use of PEG hydrogels, multiplexing, parallel random fabrication, to an enhanced shape-encoding scheme with automated pattern recognition. Although the different aspects of the MUFFINS platform have been individually explored in previous works [22, 45, 52–54, 65, 70–72], they have not been leveraged collectively. To this end, a multiplexed, self-assembled microarray was designed, fabricated, and used in sensing to demonstrate the full potential of the platform.

10.2 Experimental

The photolithography and sensing methods have been previously described (Section 9.5 and [22, 52–54, 71, 72]). For completeness, a brief description of the modifications relevant to this experiment is described.

10.2.1 Materials

Poly(ethylene glycol) diacrylate (PEG-da) with a weight-average molecular weight of 10,000 was purchased from SunBio. All pre-polymer formulations are described in volume percents. Darocur 1173, a liquid, photoinitiated free-radical generator, was obtained from Ciba-Geigy. Functionalized single-stranded DNA sequences were purchased from Integrated DNA Technologies.

10.2.2 Pre-Polymer Formulations

The sensors were made from a pre-polymer solution consisting of 20 % PEG-da, 2 % Darocur 1173, and 78 % of probe DNA solution in DI water diluted to 10 μM DNA concentration (see Tables 10.1 and 10.2 for the sequence of each probe and the multiplexing shape-encoding assignments). The probe DNA sequences contained 5' methacrylamide functionality to enable covalent attachment of the DNA into the hydrogel matrix during polymerization. In addition to the probe DNA, an additional background DNA sequence designated "BG" was added to each sensor. The complementary sequence to BG was attached to a different fluorophore (Cy5) than the target sequences (Cy3). The purpose of the BG was soley to aid in the illumination of the background bright-field image for the analysis. It is not required for ascertaining the sequence of unknowns. The sensor shape-encoded with the "U" pattern was reserved as an experimental negative control and was formulated with only the BG sequence.

Table 10.1: Probe sequences used in the detection assays.

Probe	DNA Sequence
1	5' - GTGCATGTT - 3'
2	5' - GTGCTTGTT - 3'
3	5' - CGTATTTGTG - 3'
4	5' - TGCGTCTTT - 3'
5	5' - GCGTTTTTG - 3'
6	5' - GTGGTTGTG - 3'
7	5' - GTGCTTGTG - 3'
8	5' - GTTAGTGCC - 3'
9	5' - GTGTTGGTG - 3'
10	5' - GTGTTCGTG - 3'
11	5' - GTGTTTATGC - 3'
12	5' - GTTTCTGCC - 3'
REF	5' - CGTGTTTGT - 3'
BG	5' - TGCCTGTTT - 3'

Table 10.2: Binary loading patterns for each of the probes used in the array. (0 - sensor does not contain probe, 1- sensor contains probe).

Probe	Shape-encoding					
	U	T	E	X	A	S
1	0	0	0	0	0	1
2	0	0	0	0	1	0
3	0	0	0	0	1	1
4	0	0	0	1	0	0
5	0	0	0	1	0	1
6	0	0	0	1	1	0
7	0	0	0	1	1	1
8	0	0	1	0	0	0
9	0	0	1	0	0	1
10	0	0	1	0	1	0
11	0	0	1	1	0	0
12	0	0	1	1	0	1
REF	0	1	0	0	0	0

10.2.3 Exposure Tool and Hydrogel Fabrication

Broadband ultraviolet radiation from a high-pressure mercury arc lamp (Novacure) was used for photocuring the pre-polymer. The nominal intensity of the collimated light was 16 mW/cm^2, as measured by a Molectron PowerMax 5200 intensity meter. The shutter was controlled by an internal timer. Sensors were prepared by placing the pre-polymer solution between the photomask and a chromium-coated plate with 0.25 mm thick cover slips acting as spacers. The curing dose was determined empirically to be 1600 mJ/cm^2 based on the physical properties of the hydrogels and an evaluation of their shape viewed under an optical microscope. After exposure, The sensors were separated from the mask and plate, and rinsed with DI water to remove any unreacted pre-polymer.

10.2.4 Array Formation through Self-Assembly

After individual batches of the sensors were fabricated and rinsed, the sensors were inspected using an optical microscope for defects. The well-formed sensors were combined and stored in a single container filled with DI water. The pre-polymer composition for the array backing was identical to the pre-polymer composition for the sensors except that water was used in place of the probe and background DNA. Approximately 3 mL of the pre-polymer solution was dispensed into a small plastic Petri dish (BD Falcon, Model 351008 35 × 10 mm). The dish was placed on top of an orbital shaker (VWR Advanced Orbital Shaker Model 3500). The sensors were carefully lowered one at a time onto the surface of the pre-polymer solution. Care was taken to ensure the sensors floated and did not overlap. After all of the sensors were deposited, the orbital shaker was set to 45 rpm for 30 min. A pipette tip was used to loosen sensors that adhered to the wall of the container. The orbital shaker was then set to 60 rpm for 30 min. This initial process was repeated two more times to release most of the sensors attached to the wall. The orbital shaker was then set to 45 rpm overnight to complete the assembly and allow the array to obtain a hexagonally close-packed configuration. After assembly, the array of sensors was fixed in the backing by cross-linking the pre-polymer with a 60 s exposure using a handheld UV lamp (Upland UVP UVGL-25 Compact UV Lamp). The active array portion was extracted and soaked in DI water to remove unreacted pre-polymer from the backing.

10.2.5 Hybridization Media Formulation

The DNA detection assay was conducted in a hybridization mixture which included: 500 μL buffer solution, 5.0 μL Cy3 fluorescently labeled target DNA sequence in DI water (1 mM), and 5.0 μL Cy5 fluorescently labeled background DNA sequence in DI water (1 mM). The target sequences are listed in Table 10.3. The buffer solution consisted of 2.0 % (v/v) tris(hydroxymethyl)aminomethane (pH 7.6), 6.9 % 5 M NaCl, 0.4 % ethylenediaminetetraacetic acid (EDTA), 20 % formamide, and 70.7 % DI water. Three separate assays were performed, each containing one unique Cy3 target (TGT 4, TGT 9, or TGT REF) and the Cy5 background target (TGT BG).

Table 10.3: Target DNA Sequences.

Target Name	DNA Sequence	Fluorophore
TGT 4	5' - /Cy3/ GCCACAAAGACGCAG - 3'	Cy3
TGT 9	5' - /Cy3/ GGCACTAACACGCAC - 3'	Cy3
TGT REF	5' - /Cy3/ GGCACAAACACGCAC - 3'	Cy3
TGT BG	5' - /Cy5/ GGCACAAACAGGCAC - 3'	Cy5

10.2.6 Hybridization Procedure

For each assay, prehybridization buffer rinses were performed by rinsing the array three times in 10 mL of buffer to establish the proper hybridization environment within the hydrogel. The elapsed time for each rinse was at least 8 h. Between each rinse, the array was washed three times with 2.5 mL of the buffer. After the third prehydridization buffer rinse, the buffer solution was removed. The hybridization mixture containing the target DNA sequences was then dispensed onto the array and hybridization was allowed to occur for 24 h. To ensure even distribution, the hybridization mixture was periodically drawn up and redispensed during the 24 h hybridization time. After hybridization, the array was rinsed with buffer solution (posthybridization buffer rinses) in the same manner as described in the prehybridization buffer rinses. The array was then rinsed two times in 10 mL of 2.5 M NaCl solution to remove unbound target DNA sequences. The elapsed time for each rinse was at least 1 h. Between each rinse and prior to imaging, the array was washed three times with 2.5 mL of 2.5 M NaCl solution. All of the posthybridization rinses were conducted in a water bath held at 21 °C. Between each assay, i.e. shifting target DNA sequences, the array was rinsed once in 10 mL of DI water (3 h) followed by two rinses in 10 mL formamide (3 h each) to remove all bound target DNA sequences and to "reset" the array.

10.2.7 Imaging and Pattern Recognition

A GenePix 4000B microarray scanner from Molecular Devices was used for fluorescent imaging. The scanner is capable of capturing fluorescent images using a 532 nm (Cy3) and 635 nm (Cy5) excitation source, with 5 μm resolution. Fluorescent images were acquired at 532 nm and 635 nm. The image at the 532 nm wavelength was obtained to show the binding response to the target DNA sequences while the image at 635 nm wavelength was obtained as a bright-field image to show all sensors in the array. The images were processed using the methods and scripts described previously (Section 9.4 and [52]). The relevant parameters used in the pattern recognition algorithm are listed in the Appendix C.

10.3 Results and Discussion

The sensors encoded with dot patterns representing various letters were fabricated in batches and randomly self-assembled into an array. An image of the array viewed via an optical microscope is shown in Figure 10.1. Since the array is larger than the field of view of the lens, Figure 10.1A is a composite of images of sections of the array (manual stitching). The distribution of the sensor types in the array was obtained through visual inspection, and is summarized in Table 10.4. The identities of the individual sensors are also

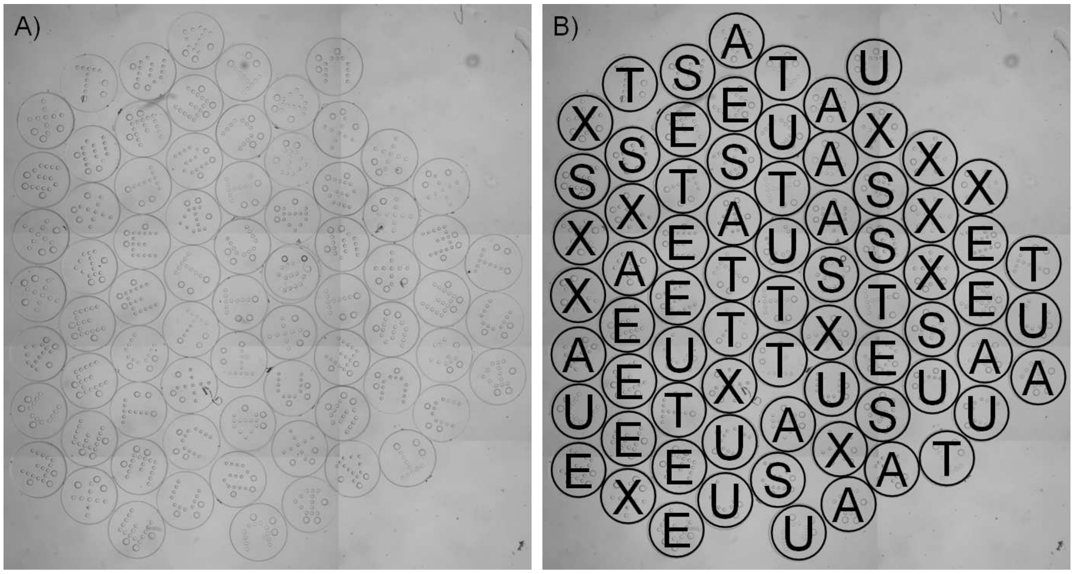

Figure 10.1: A) Image of the assembled array captured with an optical microscope in transmission mode and manually stitched. B) Image of the assembled array with overlay identifying individual sensors.

Table 10.4: Distribution of each sensor type within the array.

Sensor Type	Count	Composition Fraction
U	12	0.167
T	12	0.167
E	13	0.181
X	13	0.181
A	12	0.167
S	10	0.139

superimposed as shown in Figure 10.1B. A total of 72 sensors were incorporated into the array. Table 10.4 shows that the six different types of sensors were evenly distributed in the array with composition fractions close to one-sixth (from 0.139 - 0.189). The inspection also revealed that 34 out of 72 (47 %) of the sensors were inverted.

10.3.1 Array Formation through Self-Assembly

Figure 10.1A shows that, with the exception of several sensors on the outer edge of the array, the self-assembly process was successful in assembling the sensors into a hexagonally close-packed configuration. The selection of the 45 rpm rotation speed was determined empirically. This rotation speed provided the system with enough energy to overcome any local minima or configurations other than the hexagonally close-packed configuration, but not so much energy that the system would not self-assemble. Several rotation speeds were used during the optimization of the self-assembly conditions. High rotation speeds (> 60 rpm) resulted in a vigorous and unstable flow of the liquid pre-polymer that caused the array to become disordered. Low rotation speeds (< 45 rpm) did not provide enough agitation to break-up the local minima. Three initial "annealing-like" cycles from 45 rpm to 60 rpm back to 45 rpm were used to speed up the assembly by allowing several isolated groups of sensors to come to close proximity. Ultimately, 45 rpm was selected for the assembly process and allowed the array to assemble to the close-packed configuration.

The selection of the array backing material was also important. The backing of the array had to provide sufficient structural integrity, while at the same time be porous enough to allow adequate diffusion of target probe species. Additionally, the backing material should accommodate any swelling of the individual sensors. Since the MUFFINS sensors were intentionally constructed as a porous hydrogel, the amount of water uptake and, thus, the amount of swelling depends on the concentration of ionic species in the surrounding medium. In the course of a sensing experiment, solutions of various ionic strengths are used. An array in which the swelling characteristics of the backing and sensors are not matched can introduce nonuniform stresses on the sensors and cause deformations such as skewing of alignment and coding dots. Therefore, the backing material needs to have the proper balance of rigidity and porosity characteristics to meet these structural integrity, diffusion, and swelling requirements.

Several pre-polymer materials (PEG-da MW 700 and MW 10,000) and compositions (varying ratios of water, PEG-da monomer, and photoinitiator) were tested. Backings with low monomer content had poor structural integrity whereas backings with higher monomer content had improved structural integrity. Backings constructed with PEG-da 700 did not have the same swelling profile. The pre-polymer composition similar to the MUFFINS sensors was used to match the swelling and diffusion properties of the backing and sensors. The structural integrity of the array was improved by increasing the thickness of the backing.

10.3.2 DNA Sensing with Multiplexing

After the post-hybridization rinses, the sensors were imaged with a fluorescent microarray scanner. The acquired images with each of the three different target DNA trials are shown from Figure 10.2 to Figure 10.4. Each sensor type contained multiple types of single stranded DNA (loading dictated by Table 10.2), for target sensing and background illumination when observed with a fluorescent scanner, copolymerized into the hydrogel matrix via a 5' methacrylamide functionality. The sensors were designed to register a positive, i.e. fluorescence signal, upon binding of the probe to its complementary target sequence (with a 5' Cy3 fluorescent tag) or background sequence (with a 5' Cy5 fluorescent tag). For each target listed in Table 10.3, the designa-

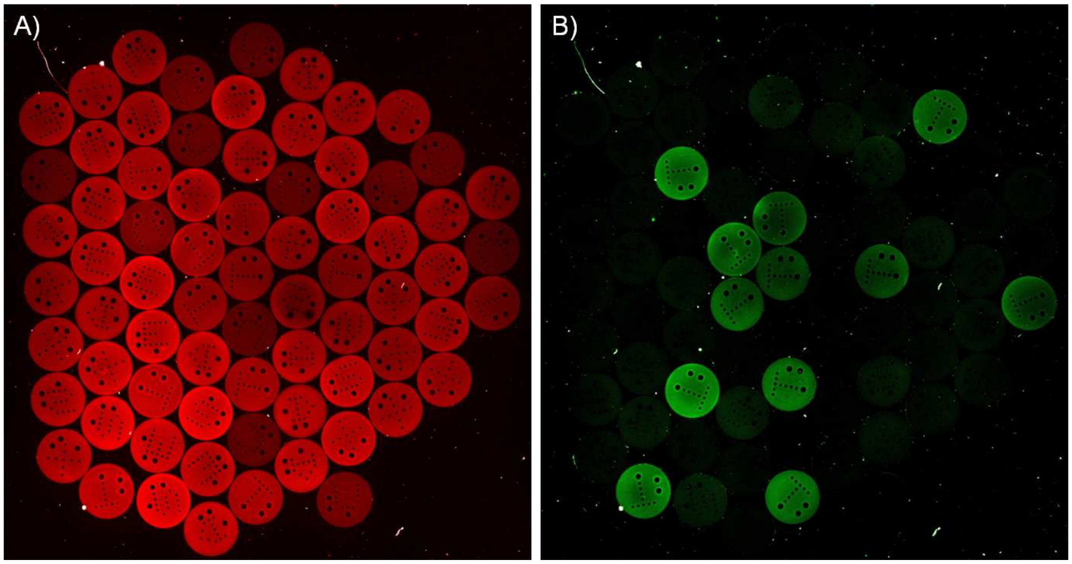

Figure 10.2: Results with the TGT REF labeled target. A) Bright-field background image showing fluorescence using 635 nm illumination. B) Target image showing fluroescence using 532 nm illumination.

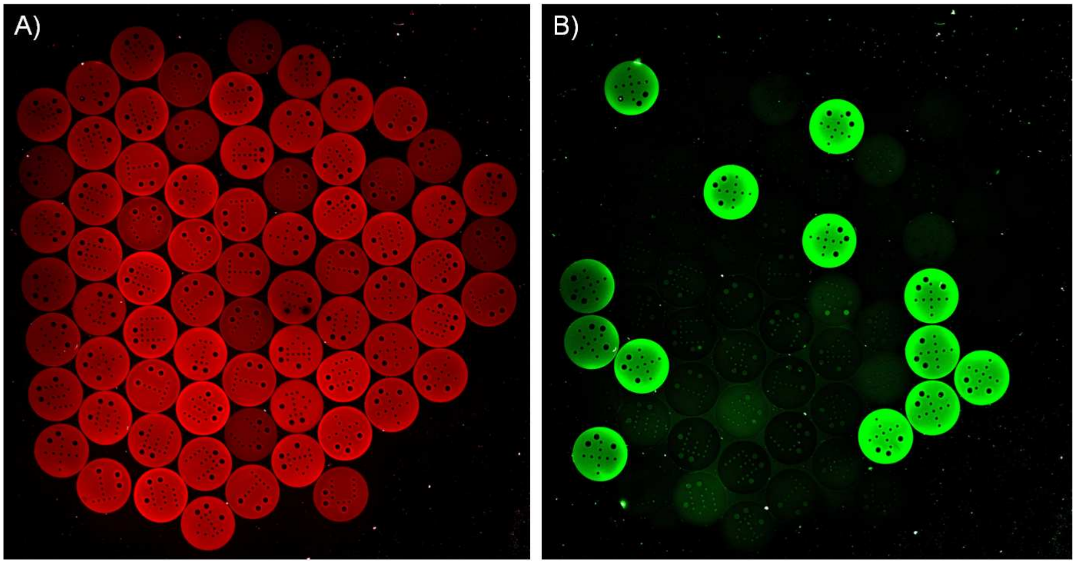

Figure 10.3: Results with the TGT 4 labeled target. A) Bright-field background image showing fluorescence using 635 nm illumination. B) Target image showing fluroescence using 532 nm illumination.

tion after the "TGT" refers to the complementary probe sequence shown in Table 10.2. Figures 10.2 to 10.4 show images acquired with 635 nm and 532 nm illumination and are designated "background image" and "target image", respectively.

The background images in Figures 10.2A, 10.3A, and 10.4A show that the use of the Cy5 labeled probe BG was able to provide a background bright-field image that allows all sensors in the array to be seen. The images also correspond to those captured by the optical microscope where 72 fluorescing sensors are fully visible, i.e. the dot patterns are completely within the frame of the image. Figures 10.2B, 10.3B, and 10.4B show the specific binding of the fluorescently labeled complementary target sequences. Based on visual

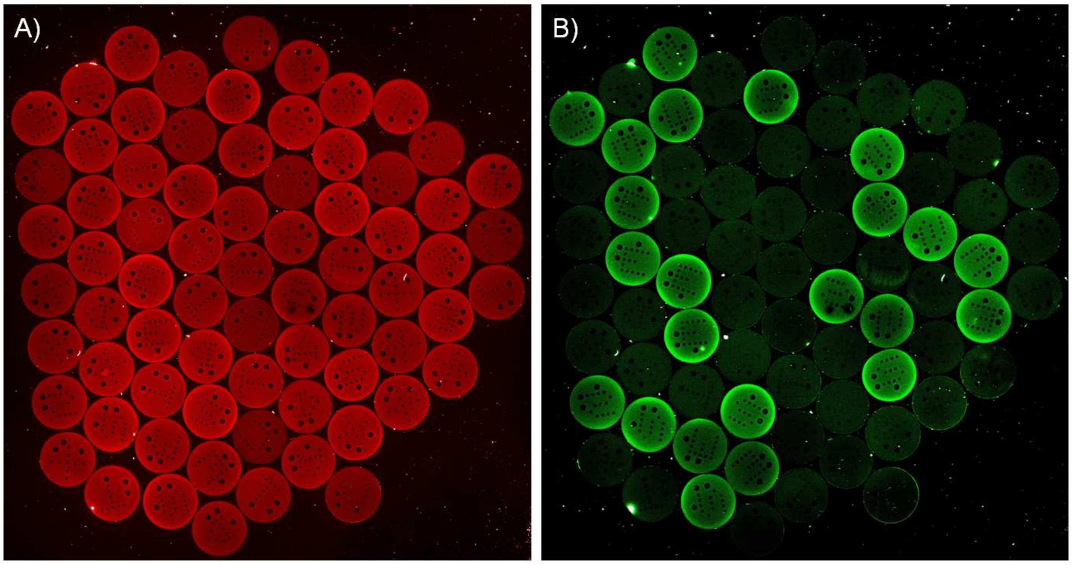

Figure 10.4: Results with the TGT 9 labeled target. A) Bright-field background image showing fluorescence using 635 nm illumination. B) Target image showing fluroescence using 532 nm illumination.

inspection of the target images, fluorescence was only observed in the sensors containing the probe specific to the dye-labeled target. Figure 10.2B shows that fluorescence was only observed in sensors shape-encoded with the “T” pattern. This corresponds to a binary code of 010000 in the multiplexing-encoding scheme. Mapping the code to Table 10.2 reveals that the target sequence was specific to the probe REF. Indeed, TGT REF was used as the target sequence in the hybridization mixture for this assay. Similarly, Figure 10.3B shows the fluorescence of sensors shape-encoded with the “X” pattern which correspond to a binary code of 000100 and specific binding of probe 4 to TGT 4. Figure 10.4B shows the fluorescence of sensors shape-encoded with the “E” and “S” patterns which correspond to a binary code of 001010 and specific binding of probe 9 to TGT 9. Every sensor corresponding to the target in each assay fluoresced as predicted, which suggest that that no false negative results were observed. Conversely, no false positive results were observed, especially in the negative control (sensor shape-encoded with the "U" pattern). These results demonstrate repeated successful sensing experiments using multiplexing and the binary encoding of probes with a single array.

10.3.3 Pattern Recognition Results

The pattern recognition algorithm was applied to the images to identify the shape-encoding on each fluorescing sensor. The results for the background and target images are shown in Figure 10.5 to Figure 10.7 and Figure 10.8 to Figure 10.10, respectively. The order in which the sensors appear in the figures varies slightly due to small discrepancies in rotation which arise from placing the array on the scanner and global minimum threshold levels. However, since the information is associated with the identity of the sensor and not the location, the order of appearance is not critical. Also, slight modifications to the recognition algorithm described previously [52] were required to process the array effectively. For the sake of brevity, the details of the modifications are described in the Appendix C. The modifications were necessary because the signal captured from the array was not as intense and uniformly distributed as the sensors used with the previous work.

The lower observed intensity may be related to the use of the backing and its diffusion properties as mentioned earlier. A combination of larger soak

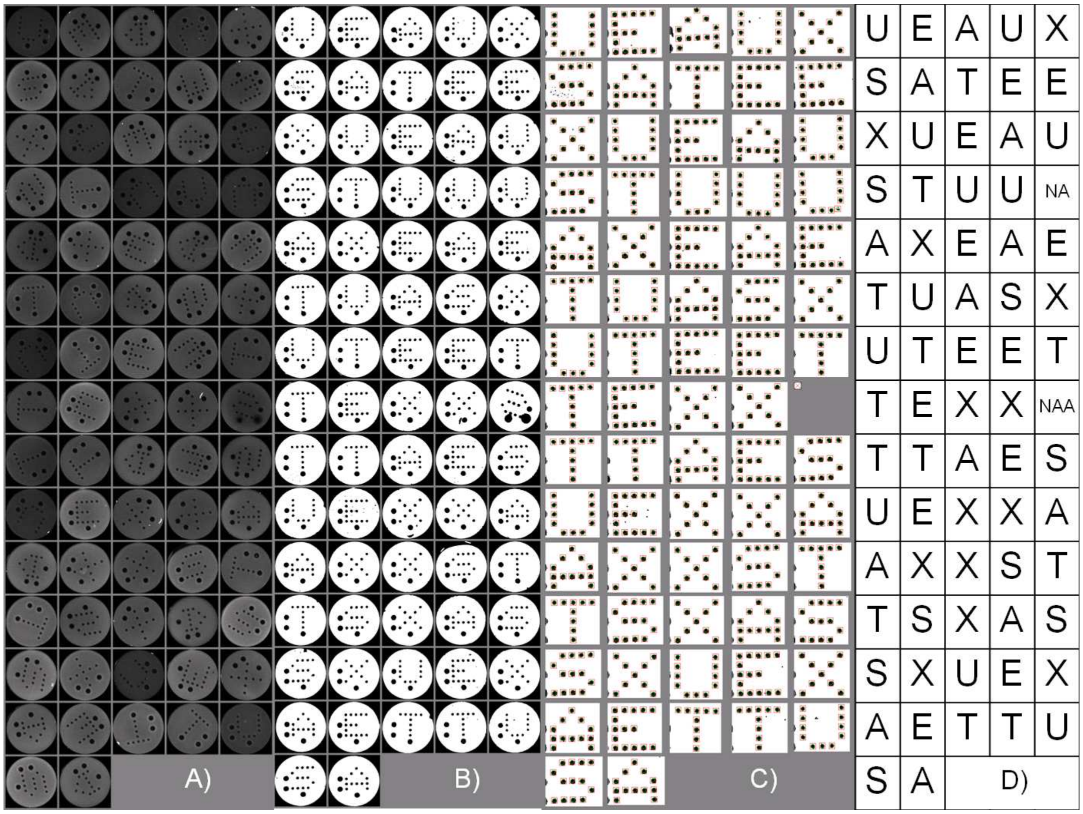

Figure 10.5: Shape recognition results for the TGT REF background image (635 nm illumination). A) Fluorescent micrograph after grayscaling, circle feature recognition, and image extraction. B) Image after local standard deviation thresholding, binarization, and rotation. C) Pattern recognition results, with recognized coding dots in square boxes. D) Report of detected patterns.

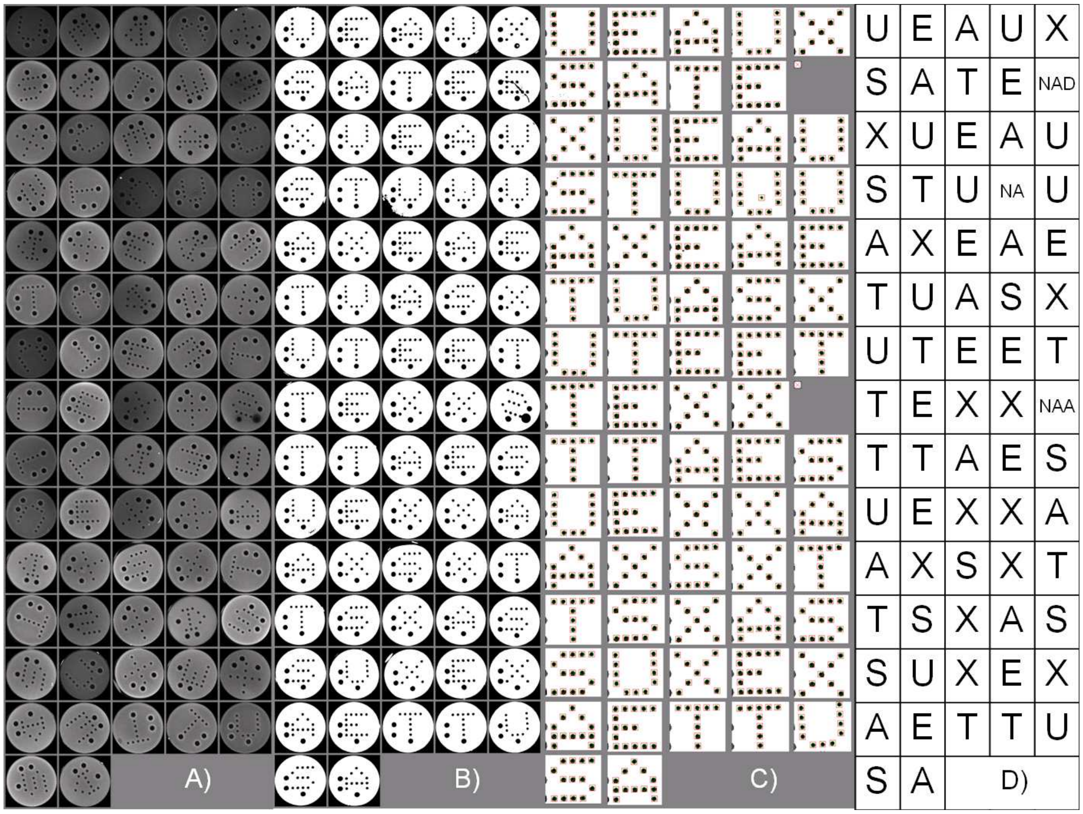

U	E	A	U	X
S	A	T	E	NAD
X	U	E	A	U
S	T	U	NA	U
A	X	E	A	E
T	U	A	S	X
U	T	E	E	T
T	E	X	X	NAA
T	T	A	E	S
U	E	X	X	A
A	X	S	X	T
T	S	X	A	S
S	U	X	E	X
A	E	T	T	U
S	A			

Figure 10.6: Shape recognition results for the TGT 4 background image (635 nm illumination). A) Fluorescent micrograph after grayscaling, circle feature recognition, and image extraction. B) Image after local standard deviation thresholding, binarization, and rotation. C) Pattern recognition results, with recognized coding dots in square boxes. D) Report of detected patterns.

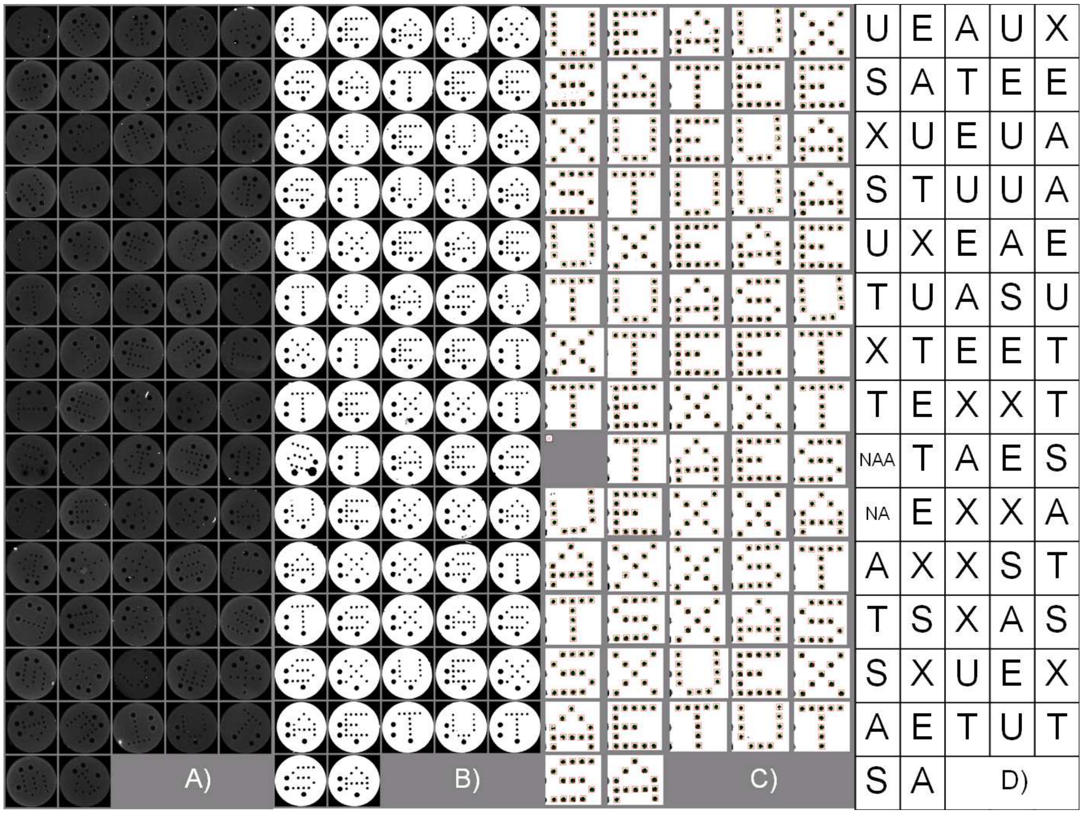

U	E	A	U	X
S	A	T	E	E
X	U	E	U	A
S	T	U	U	A
U	X	E	A	E
T	U	A	S	U
X	T	E	E	T
T	E	X	X	T
NAA	T	A	E	S
NA	E	X	X	A
A	X	X	S	T
T	S	X	A	S
S	X	U	E	X
A	E	T	U	T
S	A			

Figure 10.7: Shape recognition results for the TGT 9 background image (635 nm illumination). A) Fluorescent micrograph after grayscaling, circle feature recognition, and image extraction. B) Image after local standard deviation thresholding, binarization, and rotation. C) Pattern recognition results, with recognized coding dots in square boxes. D) Report of detected patterns.

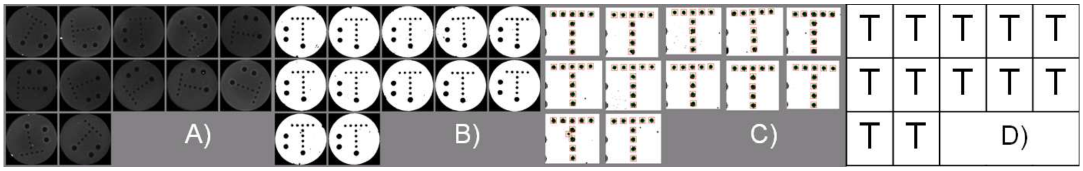

Figure 10.8: Shape recognition results for the TGT REF target image (532 nm illumination): A) Fluorescent micrograph after grayscaling, circle feature recognition, and image extraction. B) Image after local standard deviation thresholding and binarization. C) Pattern recognition results, with recognized coding dots in square boxes. D) Report of detected patterns.

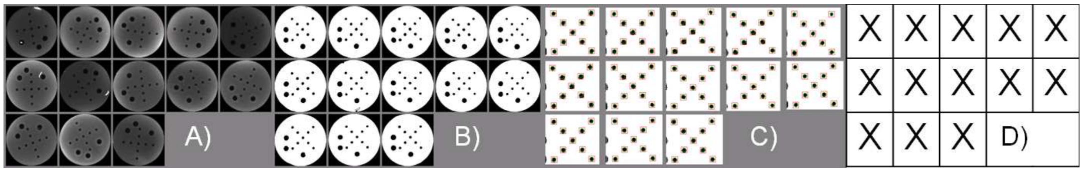

Figure 10.9: Shape recognition results for the TGT 4 target image (532 nm illumination): A) Fluorescent micrograph after grayscaling, circle feature recognition, and image extraction. B) Image after local standard deviation thresholding and binarization. C) Pattern recognition results, with recognized coding dots in square boxes. D) Report of detected patterns.

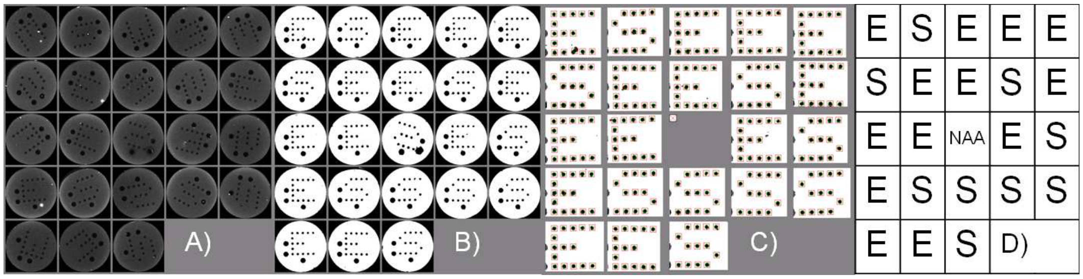

Figure 10.10: Shape recognition results for the TGT 9 target image (532 nm illumination): A) Fluorescent micrograph after grayscaling, circle feature recognition, and image extraction. B) Image after local standard deviation thresholding and binarization. C) Pattern recognition results, with recognized coding dots in square boxes. D) Report of detected patterns.

volumes, frequent washes, and longer soak times were required to rinse out the non-specifically bound target probes in the sensors and the backing material. In the process, more specifically bound target probes were washed out compared to the sensing experiments without the polymer backing. The low intensity issue may be mitigated by further fine-tuning of soaking volumes and buffer compositions to increase the specific binding of target probes. Despite the lowered contrast, the positive signals were readily discernable via visual inspections and the pattern recognition algorithms as described below.

For the background images, Figure 10.5 to Figure 10.7 show that the algorithm was able to distinguish the six different shape-encoded dot matrix patterns representing the letters “U”, “T”, “E”, “X”, “A”, and “S”. The recognition rate for the TGT REF, TGT 4, and TGT 9 trials were 97 %, 96 %, and 97 %, respectively. Figures 10.11 to 10.13 show that a common error (sensor “S”) was observed in all of the background images. The relevant error codes are defined in Table 10.5. Upon examination of the image of the sensor, one of the alignment dots was found to be defective as it is much larger than the nominal size and, therefore, not recognized by the algorithm. Because the algorithm could not find enough alignment dots for the sensor, it was not able

Table 10.5: Definition of error codes generated by the pattern recognition software.

Code	Description
NA	Dot sequence does not match any listing in the key
NAA	Not enough alignment dots found
NAD	No coding dots found

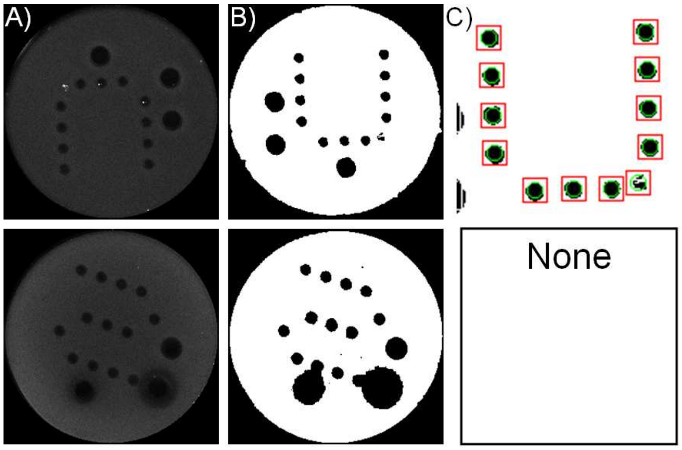

Figure 10.11: Recognition errors for TGT REF background image. A) Original extracted image. B) Thresholded, binarized, and rotated image. C) Recognition result.

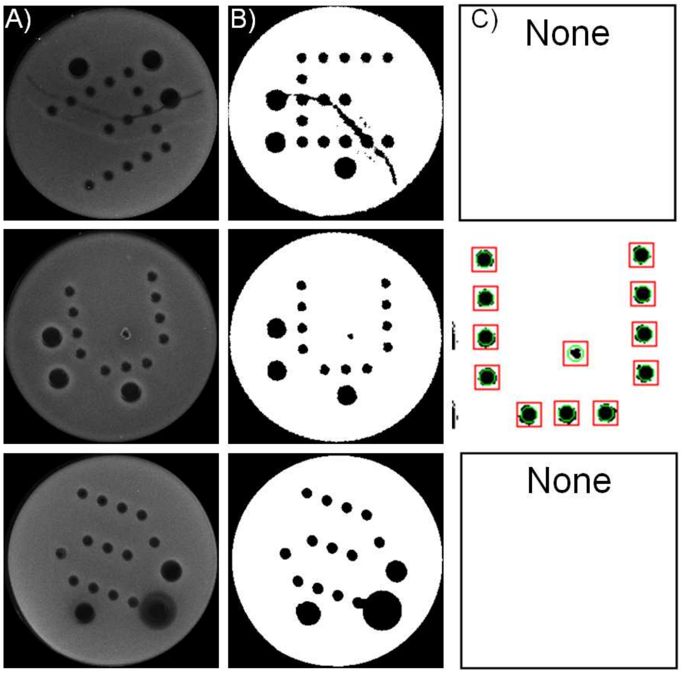

Figure 10.12: Recognition errors for TGT 4 background image. A) Original extracted image. B) Thresholded, binarized, and rotated image. C) Recognition result.

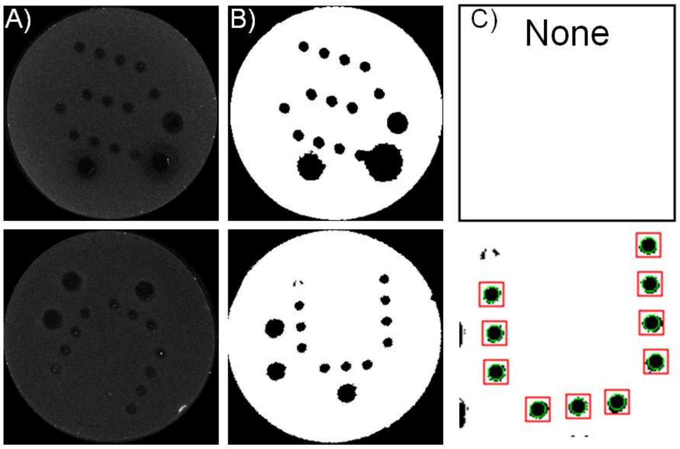

Figure 10.13: Recognition errors for TGT 9 background image. A) Original extracted image. B) Thresholded, binarized, and rotated image. C) Recognition result.

to determine the proper orientation and pattern of the sensor. The origin of this defect is not completely clear; however, it is likely that it occurred during fabrication as it is seen in all trials.

The remaining recognition errors observed were specific to each trial. Figure 10.11 shows that a sensor “U” was not recognized in the TGT REF trial due to the detection of an extra coding dot caused by a false bright spot. Figure 10.12 shows that two other sensors, one each of type “E” and “U”, were not recognized for the TGT 4 trial. A long dark streak was observed in the “E” sensor so that an errant alignment dot was detected. A dark spot was observed in the “U” sensor so that an extra coding dot was detected. Figure 10.13 shows that a sensor “U” was not recognized for the trial with TGT 9 because the center of a coding dot was “gray”. With the exception of sensor “U” in Figure 10.12, the other errors were likely due to particle contamination. Depending on the nature of the particle, the errors can be manifested in different ways. Certain particles are highly reflective and can lead to unwanted scattering as seen in the defects in Figure 10.11 and Figure 10.13 (sensor “U” in both cases). Other particles may cause dark spots by either absorbing any emitted light or scattering light away from the detector as seen in sensor “E” in Figure 10.12. The error observed in sensor “U” (Figure 10.12) is likely due to physical damage to the sensor from handling. This error was not propagated into the other images because the TGT 4 trial was performed after both the TGT REF and TGT 9 trials.

Because these recognition errors were specific to each trial, the particle contamination or damage observed likely occurred during handling of the array. During each sensing trial, physical handling of the array was often required. Because of the small volume of the hybridization fluid, the array was transferred to a small Petri dish to ensure proper coverage. However, to ensure proper rinsing and maximize diffusion, the array was transferred to a 50 mL centrifuge tube during the rinsing and soaking steps. The geometry of the centrifuge tube allows the array to be completely submerged. When changing the solution during the rinsing and soaking steps, the tube had to be repeatedly opened and exposed to particles in the air. Finally, the array was transferred to a glass slide for imaging. While care was taken at each step to minimize particle contamination and physical damage, defect contamination was not completely prevented. The defects could be further reduced by conducting all aspects of the sensing experiment within a cleanroom environment and designing a fluid handling system to reduce the physical manipulation of the array.

Figure 10.8 to Figure 10.10 show the pattern recognition results on the target images from the three different sensing trials. The algorithm reported 100 % recognition rate for the TGT REF and TGT 4 target images. The only recognition error reported, shown in Figure 10.14, from the software was in the TGT 9 target image resulting in a recognition rate of 96 %. Figure 10.14 shows that the observed error occurred in the same sensor "S" that was also erroneous in all of the background images. Even with this recognition error, the array was still able to identify the target probe due to the built-in redundancy; the nine other "S" sensors were correctly recognized. Upon closer visual examination of the pattern recognition output in Figure 10.8C, the algorithm identified an extra coding dot on the sensor located at the bottom left corner (larger image shown in Figure 10.15). Since the erroneous dot was close in proximity to an actual coding dot, the algorithm did not recognize the error. Figure 10.15A shows that the erroneous coding dot was due to a bright

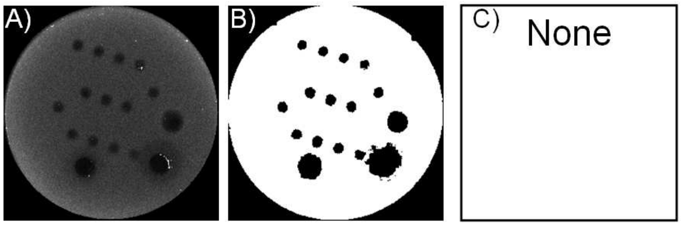

Figure 10.14: Recognition errors for TGT 9 target image. A) Original extracted image. B) Thresholded, binarized, and rotated image. C) Recognition result.

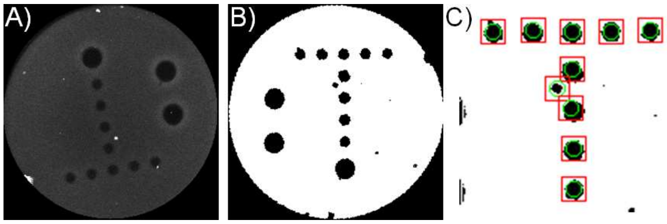

Figure 10.15: Recognition errors for TGT REF target image. A) Original extracted image. B) Thresholded, binarized, and rotated image. C) Recognition result.

spot, most likely caused by dust. Accounting for this error, the TGT REF sensing trial had an adjusted recognition rate of 92 %. This recognition rate is smaller than the background TGT REF sensing trial recognition rate which had two errors because of the smaller sample size of 12 versus 72. Again, the accuracy of identification is ensured by the built-in redundancy from the other 11 correctly identified sensors.

These results demonstrate the viability of the MUFFINS platform as a random biochip array fabrication technique, with the key components – lithographic sensor fabrication, self-assembly, multiplexing, and pattern recognition – all working together. The sensor arraying and fabrication processes must be well controlled such that an optimal set of algorithm parameters will consistently identify the sensors with a high success rate. Defects and debris in all steps of the process must also be reduced to prevent pattern recognition errors. The low contrast should be enhanced with further optimization of the rinsing conditions.

10.4 Conclusions

A successful DNA sensing experiment has been demonstrated using the MUFFINS biochip platform. The key components of the MUFFINS platform, including lithographic sensor fabrication, self-assembly, multiplexing, and pattern recognition, were successfully integrated to facilitate batch photolithographic sensor fabrication, random array formation, bioprobe sensing, and automated pattern recognition, all key requirements for an efficient biochip. The results show that this system is able to perform repeated multiplexed sensing experiments with an 96 % recognition accuracy.

Chapter 11

Conclusions and Recommendations

11.1 Conclusions

11.1.1 Materials Modeling for Double-Exposure Lithography Applications

Double-exposure lithography offers several advantages over double-patterning lithography, but it requires new materials with nonlinear dose response behavior. A custom DEL simulator was developed to study the behavior of potential materials through feasibility studies. The results from the feasibility studies revealed that the ISTP and OTL types of materials showed much more promise than the rCEL and two-photon types of materials. Calculations show that two-photon materials will not be feasible unless achievable laser peak power in exposure tools can be significantly increased. Although rCEL materials demonstrated nonlinear behavior in DEL mode, the image quality and process window improvement was only observed for rCELs with very high Dill A parameters ($> 30\ \mu\text{m}^{-1}$). Even if physical analogs with such high Dill A parameters are obtainable, the improvements are marginal.

To further confirm the results from the feasibility study, several of the imaging conditions were further optimized to evaluate how the materials would perform under more ideal conditions. As expected, optimizing the imaging conditions improved the resulting material performance in all cases with the largest improvements observed in changing the illuminator a dipole. However, the improvements in the ISTP and OTL material were considerably better than the rCEL which reaffirmed the conclusion from the the previous feasibility studies and the decision to pursue development of the ISTP and OTL materials.

With the guidance from the simulation results, work has begun to identify proof-of-concept materials with the prescribed ISTP and OTL behaviors. A potential system was identified for the ISTP type material using electron transfer to a PAG. However, the kinetics of the process still have to be characterized in detail. Some key concepts such as photo-induced phase change and phase-modulated diffusion were demonstrated through experiments for the OTL material and work is ongoing to identify a suitable proof-of-concept system. In both cases, the ultimate goal is to find a truly manufacturable system operating in the 193 nm range.

11.1.2 Development of the MUFFINS Biosensor Platform

The MUFFINS platform was developed in the Willson Research Group as a potential method to achieve a new low-cost biosensor system. The system used arrays of self-assembled, shape-encoded PEG hydrogel sensors with embedded bioprobes that were fabricated using photolithography. The key designs of the system include parallel batch fabrication using photolithography and self-assembly, increased information density using multiplexing, and enhanced shape-encoding with automated pattern recognition. Several of the platform design concepts have been demonstrated by colleagues including photolithographic fabrication, biosensing with different moieties, multiplexing, and shape-encoding design. The thrust of the work described in this dissertation was to complete a demonstration of the fully functional system.

The self-assembly behavior of the sensors was explored through modeling. A system of equations was developed to describe the flotation of objects which are denser than the supporting fluid and form a wetting contact angle with the fluid. The equations revealed that when two objects are in close proximity, the contact line angles change to maintain a smooth curvature which induces a tilt in the particles. The tilting behavior described by the equations was validated through experiment. The equations were also used to approximate the attractive forces between particles during assembly; the forces were used in a rigid body simulation to model the dynamics of assembly. Empirical experimental results showed that an ‘agitation’ force was necessary to permit the assembly to the final hexagonally close-packed conformation. Directed-assembly experiments showed that the concept of direct-assembly was possible with the proper tuning of attractive, repulsive, and binding forces.

The dot-matrix shape-encoding scheme and accompanying pattern recognition algorithm was demonstrated in practice on a large-field image. This demonstration employed a large-field fluorescent array scanner capable of 5 μm resolution. A custom glass sample holder was constructed to enable imaging within the scanner’s focus specifications. A background probe and target sequence pairing was also incorporated to enable "bright-field" like imaging. A pattern recognition algorithm based on a previous work by Meiring was written and implemented that resolves the nonuniform intensity and skewing issues. The results show that this system is quite viable with an 98 % recognition accuracy of the non-defective sensors.

Finally, all of the key designs of the MUFFINS platform were demonstrated in an successful DNA sensing experiment. The key components of the MUFFINS platform, including lithographic sensor fabrication, self-assembly, multiplexing, and pattern recognition, were all successfully integrated to facilitate batch photolithographic sensor fabrication, random array formation, bioprobe sensing with multiplexing, and automated pattern recognition. The results show that this system is able to perform repeated multiplexed sensing experiments with an 96 % recognition accuracy.

11.2 Recommendations for Future Work

11.2.1 Materials Modeling for Double Exposure Lithography Applications

The entire body of the DEL simulation work is meant to be a single component within a larger, more complete effort to develop and bring to fruition these potential materials to manufacturing. As noted, the next phase is to identify the proof-of-concept systems for each material type with the eventual goal of identifying material systems for manufacturing. Many challenges still remain, but the most important of these is finding a set of materials that will function at 193 nm. For the ISTP material, this will mean identifying two-stage sensitizers that will absorb light at 193 nm but not generate acid, and at the same time identifying acid generators that will be transparent in 193 nm and only generate acid upon electron transfer. For the OTL material, a photo-switchable phase change material at 193 nm has to be identified along with the necessary chemistry for patterning. Although these two approaches provide a good starting point, the ultimate goal is to find materials to enable DEL, and as such, the research effort would benefit by remaining attentive to other mechanistic possibilities.

With regard to the custom DEL simulator, it may still be a valuable tool to complement the materials development work. Once model systems have been identified and appropriately characterized, the new parameters and elucidated mechanisms can be examined with the DEL simulator. The current modular implementation allows for rapid prototyping of new material behaviors. This will serve to both aid in the evaluation of the proposed models and provide simulation capabilities for the model systems in production.

11.2.2 Development of the MUFFINS Biosensor Platform

The work described in this dissertation in combination with previous publications demonstrated a proof-of-concept experiment for the MUFFINS platform and showed that it could be a viable biosensor system. At this juncture, the technology is in a developmental state. A possible next step for the technology is to develop the platform into a commercial product. This transition should be accompanied by careful evaluation of the market needs to find the best fit for the technology. The challenges to commercialization will be four-fold. First, having ascertained the market need, the appropriate sensing chemistries will have to be identified and incorporated into the MUFFINS platform. Second, the robustness of the platform will have to be improved on all aspects from fabrication to detection in order to improve repeatability. Third, scale-up strategies will have to be developed to enable large scale manufacturing. This encompasses the tools required for fabrication, handling of the sensors, and encapsulation of the arrays. Lastly, the deployment of the platform should also be considered which includes the necessary supporting technologies such as the imaging tool and analysis interface.

Appendices

Appendix A

Tilt Modeling Derivation

A.1 Introduction

As described in Chapter 8, the assembly of MUFFINS array entailed self-assembling the sensors on the surface of a pre-polymer solution through lateral capillary interactions. Understanding the assembly process required a description of the surfaces surrounding the particles. Some of the equations governing the surface interactions and force balances were presented in Chapter 8. The derivations for those equations are provide in this section and are based on various published [6, 39, 40] and unpublished works [5, 12].

A.2 Describing the Meniscus Shape

Although the MUFFINS are effectively cylindrical discs, the geometry of the system is simplified by assuming 2-D rectangular particles where the particles are infinite bar extending into and out of the plane of the page.

A.2.1 One Particle Solution

Consider the case of one particle floating in liquid as shown in Figure A.1. The horizontal coordinate is defined by the variable x and the vertical

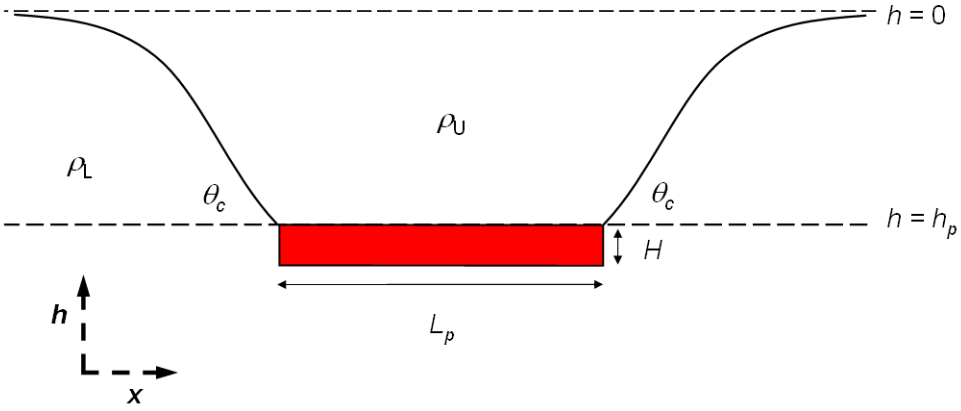

Figure A.1: Schematic of One Floating Particle

coordinate is defined by the variable h (height). The system is defined such that $h = 0$ is the unperturbed surface of the liquid far away from the particle and $h = h_p$ is where the meniscus meets the particle. The coordinate system is also set so that $x = 0$ is where the meniscus meets the particle.

The shape of the meniscus is governed by the Young-Laplace relation between the capillary and hydrostatic pressures in the following

$$\gamma \nabla \cdot \underline{n} = -\rho g h, \tag{A.1}$$

where γ is the surface tension and ρ is the differential density between the lower and upper fluids ($\rho = \rho_L - \rho_U$). The variable $\underline{n}$ is the unit normal to the surface and is expressed as

$$\underline{n} = \frac{\underline{e}_z - \frac{dh}{dx}\underline{e}_x - \frac{dh}{dy}\underline{e}_y}{\left(1 + \frac{dh}{dx}^2 + \frac{dh}{dy}^2\right)^{1/2}}, \tag{A.2}$$

where $\underline{e}_h$, $\underline{e}_x$, and $\underline{e}_y$ represent the unit vectors in the h, x, and y directions, respectively. Equation A.2 can be linearized with the following assumption

$$\frac{dh}{dx}, \frac{dh}{dy} << 1 \tag{A.3}$$

to yield

$$\underline{n} \approx \underline{e}_h - \frac{dh}{dx}\underline{e}_x - \frac{dh}{dy}\underline{e}_y. \tag{A.4}$$

Equation A.1 becomes

$$\gamma \nabla^2 h = \rho g h. \tag{A.5}$$

In rectangular coordinates, the application of the appropriate differential operator yields the following ordinary differential equation (ODE)

$$\gamma \frac{d^2 h}{dx^2} = \rho g h. \tag{A.6}$$

Equation A.6 can be rearranged into the following

$$\frac{d^2 h}{dx^2} - q^2 h = 0 \qquad \text{where } q^2 = \frac{\rho g}{\gamma}. \tag{A.7}$$

The general solution to Equation A.7 is the following

$$h(x) = a e^{qx} + b e^{-qx}. \tag{A.8}$$

The coordinate system assumes that the height of the unperturbed surface as $x \to \infty$ is zero and the height gradient at the interface between the particle and meniscus is determined by the contact line angle, θ_c. The boundary conditions are then as follows

$$\begin{aligned} h(x \to \infty) &= 0 \\ \frac{dh}{dx}(x = 0) &= \tan\theta_c. \end{aligned} \tag{A.9}$$

Applying the boundary conditions gives the resulting equation describing the height of the meniscus

$$h(x) = \frac{-\tan\theta_c e^{-qx}}{q}. \tag{A.10}$$

A.2.2 Two Particles Solution

For the two particles case, the solution can be separated into two regions, *inner* and *outer*, as shown in Figure A.2. The *inner* region (denoted by the subscript i) consists of the area between the two particles while the *outer* region (denoted by the subscript o) is the area from the outer edge of the particle to the unperturbed surface at $x \to \infty$. The coordinate system is set such that $x = 0$ is at the center between the two particles and $x = L_s$ is the half distance between the particles. The boundary conditions for the *inner*

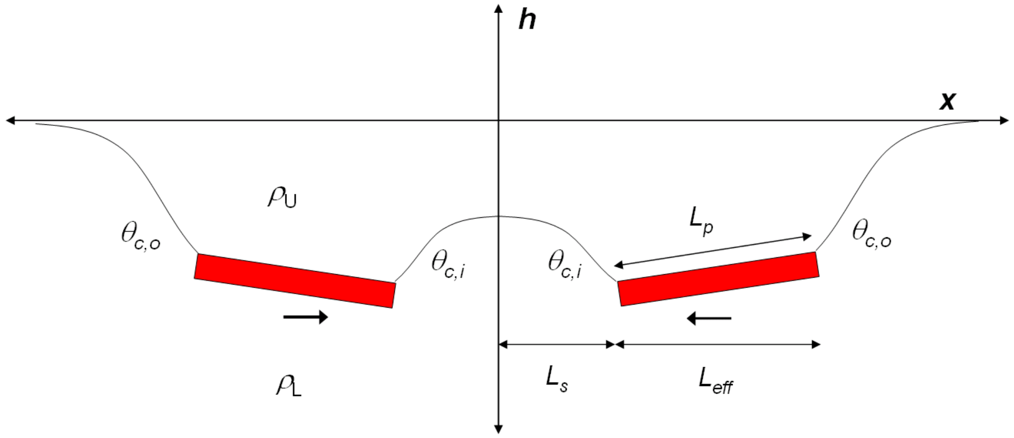

Figure A.2: Schematic of the Two Particles region are as follows

$$
\begin{aligned}
h(x = L_s) &= h_{p,i} \\
\frac{dh}{dx}(x = 0) &= 0.
\end{aligned}
$$

The second boundary condition is obtained assuming the meniscus shape is symmetrical so that the gradient at the midpoint, $x = 0$, is equal to zero. Since boundary conditions utilizes symmetry, it may be more convenient to use the hyperbolic version of the general solution, namely

$$h(x) = asinh(qx) + bcosh(qx). \tag{A.11}$$

Applying the boundary conditions gives the resulting equation describing the height of the meniscus

$$h_i(x) = \frac{h_i cosh(qx)}{cosh(qL_s)}. \tag{A.12}$$

As in the one particle case, the height gradient at the interface between the particle and meniscus is determined by the inner contact line angle, $\theta_{c,i}$ and is expressed as

$$\frac{dh}{dx}(x = L_s) = \frac{h_i q sinh(qx)}{cosh(qL_s)}\bigg|_{x=L_s} = \frac{h_i q sinh(qL_s)}{cosh(qL_s)} = -\tan\theta_{c,i}. \tag{A.13}$$

For the *outer* region, the solution is analgous to that of the one particle case with the exception that the x-coodinate needs to be shifted by $L_s + L_{eff}$ such that

$$h_o(x) = \frac{-\tan\theta_{c,o} e^{-q\left(x-(L_s+L_{eff})\right)}}{q}. \tag{A.14}$$

A.3 Tilt Analysis

Due to the proximity of the second particle in the inner region, the meniscus of the two particles superimpose in the inner region and is not able to form the same shape as for the one particle case. Consequently, the contact line angle in the inner region, $\theta_{c,i}$ must change in order to maintain a smooth meniscus curvature in the inner region. The change in $\theta_{c,i}$ also causes a discrepancy in the vertical contribution of the capillary force between the inner and the outer regions. This discrepancy results in tilting of the particles, please consult Figure A.2. This analysis uses the same geometry as the two particle case with the addition of tilt. Figure A.3 shows a close-up view of particle on the right. The height of the particle h_p is parameterized with the following equation

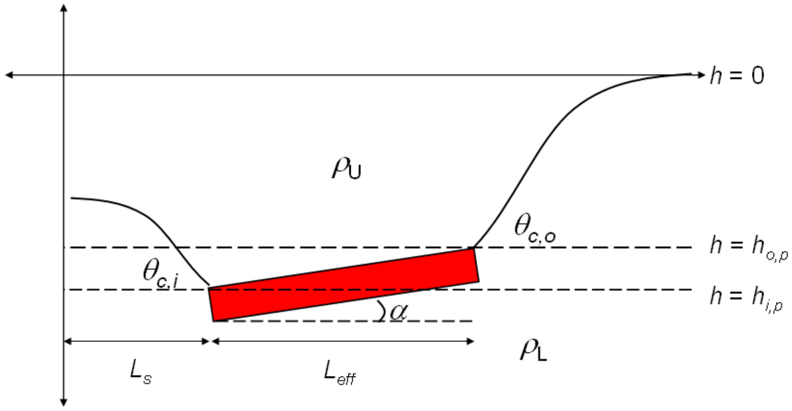

Figure A.3: Close-up Schematic of One Particle

$$h_p = \left(\frac{h_{p,o} - h_{p,i}}{L_{eff}}\right)(x - L_s) + h_{p,i}, \tag{A.15}$$

where L_{eff} is the projection of the original particle length L in the x-coordinate as the particle tilts and is defined as

$$\tan\alpha = \frac{h_o - h_i}{L_{eff}}. \tag{A.16}$$

The variable α represents the angle of tilt and can be obtained through the trignometric relation

$$\sin\alpha = \frac{h_o - h_i}{L_p}. \tag{A.17}$$

A.3.1 Vertical Force Balance

In order for the particles to stay afloat, the interface not only has to balance the hydrostatic forces but also the weight of the particle. For the one particle case, the vertical force balance per unit width for the one particle case is the following

$$F_w = F_b + F_m + F_{cap}, \tag{A.18}$$

where

$$\begin{aligned} F_w &= Mg/width \\ F_b &= \rho g L_p H \\ F_m &= -\rho g L_p h_p \\ F_{cap} &= \gamma sin\theta_c \quad . \end{aligned} \tag{A.19}$$

The pinned contact line angle θ_c changes to accomodate the weight of the particle. However, as θ_c changes, h_p also changes to satisfy the meniscus pressure balance. To solve for the equilibrium position height requires the simultaneous solution of Equations A.10 and A.18.

The complexity increases for the two particle case where the tilt has to be considered. Because of the tilt, the upward force per unit width due to the sunken height becomes

$$F_m = \rho g \int_{L_s}^{L_s+L_{eff}} \left(\frac{h_o - h_i}{L_{eff}}\right)(x - L_s) + h_i \, dx \tag{A.20}$$

$$\begin{aligned} = -\rho g \Bigg[(L_s + L_{eff}) \left[\left(\frac{h_o - h_i}{L_{eff}}\right) \left(\frac{L_s + L_{eff}}{2} - Ls\right) + h_i \right] \\ -L_s \left[\left(\frac{h_o - h_i}{L_{eff}}\right) \left(\frac{L_s}{2} - Ls\right) + h_i \right] \Bigg] . \end{aligned} \tag{A.21}$$

The negative sign is included to correct for the negative height values so that the resulting pressure will have the proper sign. The capillary contribution is divided into the inner and outer regions

$$\begin{aligned} F_{cap,i} &= \gamma sin\theta_{c,i} \\ F_{cap,o} &= \gamma sin\theta_{c,o}, \end{aligned} \tag{A.22}$$

combining Equations A.18-A.22 results in the following

$$F_w = \gamma \left(sin\theta_{c,i} + sin\theta_{c,o} \right) + \rho g L_p H$$

$$\begin{aligned} -\rho g \Bigg[(L_s + L_{eff}) \left[\left(\frac{h_o - h_i}{L_{eff}}\right) \left(\frac{L_s + L_{eff}}{2} - Ls\right) + h_i \right] \\ -L_s \left[\left(\frac{h_o - h_i}{L_{eff}}\right) \left(\frac{L_s}{2} - Ls\right) + h_i \right] \Bigg] . \end{aligned} \tag{A.23}$$

A.3.2 Torque Balance

The torsional forces on the particles is also balanced at any give L_s. Assuming the particle is free to rotate at its center of mass $x = L_s + L_{eff}/2$ (constant particle density) or L_c, the torque balance is

$$\begin{aligned}
&(L_p/2)\,\gamma\sin(\theta_{c,i}+\alpha) \\
&\quad -\rho g \textstyle\int_{L_s}^{Lc} sign(x-L_c)\,\left[\left(\frac{h_o-h_i}{L_{eff}}\right)(x-L_s)(x-L_c)\right. \\
&\qquad\qquad \left. +h_i(x-L_c)\right]\,dx \\
&= (L_p/2)\,\gamma\sin(\theta_{c,o}-\alpha) \\
&\quad -\rho g \textstyle\int_{L_c}^{L_s+L_{eff}} sign(x-L_c)\,\left[\left(\frac{h_o-h_i}{L_{eff}}\right)(x-L_s)(x-L_c)\right. \\
&\qquad\qquad \left. +h_i(x-Lc)\right]\,dx.
\end{aligned} \tag{A.24}$$

The $sign(x - L_c)$ function makes sure that the moment arm has the correct and has the following values

$$sign(x-L_c) = \left[\begin{array}{ll} -1 & x < L_c \\ 1 & x > L_c \end{array}\right. . \tag{A.25}$$

Substituting the $sign(x - L_c)$ function into Equation A.24 yields

$$\begin{aligned}
&0 = (L_p/2)\,\gamma\,(\sin(\theta_{c,i}+\alpha) - \sin(\theta_{c,o}-\alpha)) \\
&+\rho g \textstyle\int_{L_s}^{Lc} \left(\frac{h_o-h_i}{L_{eff}}\right)(x-L_s)(x-L_c) + h_i(x-L_c)\,dx \\
&+\rho g \textstyle\int_{L_c}^{L_s+L_{eff}} \left(\frac{h_o-h_i}{L_{eff}}\right)(x-L_s)(x-L_c) + h_i(x-Lc)\,dx.
\end{aligned} \tag{A.26}$$

Finally, evaluating the integrals leads to this expression

$$\begin{aligned}
0 &= (L_p/2)\,\gamma\left(\sin(\theta_{c,i}+\alpha)-\sin(\theta_{c,o}-\alpha)\right) \\
&+\rho g\left[L_c\left[\left(\tfrac{h_o-h_i}{L_{eff}}\right)\left(\tfrac{L_c^2}{3}-\tfrac{(L_c+L_s)L_c}{2}+L_sL_c\right)+h_i\left(\tfrac{L_c}{2}-L_c\right)\right]\right. \\
&\quad\left.-\,L_s\left[\left(\tfrac{h_o-h_i}{L_{eff}}\right)\left(\tfrac{L_s^2}{3}-\tfrac{(L_c+L_s)L_s}{2}+L_sL_c\right)+h_i\left(\tfrac{L_s}{2}-L_c\right)\right]\right] \\
&+\rho g\left[(L_s+L_{eff})\left[\left(\tfrac{h_o-h_i}{L_{eff}}\right)\left(\tfrac{(L_s+L_{eff})^2}{3}-\tfrac{(L_c+L_s)(L_s+L_{eff})}{2}+L_sL_c\right)\right.\right. \\
&\quad\left.+h_i\left(\tfrac{(L_s+L_{eff})}{2}-L_c\right)\right] \\
&\quad\left.-\,L_c\left[\left(\tfrac{h_o-h_i}{L_{eff}}\right)\left(\tfrac{L_c^2}{3}-\tfrac{(L_c+L_s)L_c}{2}+L_sL_c\right)+h_i\left(\tfrac{L_c}{2}-L_c\right)\right]\right].
\end{aligned} \tag{A.27}$$

A.3.3 Solving for the Tilt and Position of the Particle

In the previous analysis, the unknown variables of interest are $h_{p,o}$, $h_{p,i}$, $\theta_{c,o}$, $\theta_{c,i}$, L_{eff}, and α. The solutions to the variables are obtained by specifying L_s and then simultaneously solving the vertical force balance, the torque balance, the meniscus shape equation of both the inner and outer regions, and the trignometric relations defining L_{eff} and α. The system of equations is summarized in Table A.1. The system of equations was solved using the *fsolve* function in Matlab at specified L_s values.

Eqn A.13	$\frac{h_i q \sinh(qL_s)}{\cosh(qL_s)} = -\tan\theta_{c,i}$
Eqn A.14	$h_o = \frac{-\tan\theta_{c,o} e^{-q\left(x-(L_s+L_p)\right)}}{q}$
Eqn A.16	$\tan\alpha = \frac{h_o-h_i}{L_{eff}}$
Eqn A.17	$\sin\alpha = \frac{h_o-h_i}{L_p}$
Eqn A.23	$F_w = \quad \gamma\,(sin\theta_{c,i} + sin\theta_{c,o}) + \rho g L_p H$ $-\rho g \Big[(L_s + L_{eff}) \Big[\Big(\frac{h_o-h_i}{L_{eff}}\Big)\Big(\frac{L_s+L_{eff}}{2} - Ls\Big) + h_i\Big]$ $-L_s \Big[\Big(\frac{h_o-h_i}{L_{eff}}\Big)\big(\frac{L_s}{2} - Ls\big) + h_i\Big]\Big]$
Eqn A.27	$0 = (L_p/2)\,\gamma\,(\sin(\theta_{c,i}+\alpha) - \sin(\theta_{c,o}-\alpha))$ $+\rho g \Big[L_c \Big[\Big(\frac{h_o-h_i}{L_{eff}}\Big)\Big(\frac{L_c^2}{3} - \frac{(L_c+L_s)L_c}{2} + L_s L_c\Big) + h_i\big(\frac{L_c}{2} - L_c\big)\Big]$ $-L_s \Big[\Big(\frac{h_o-h_i}{L_{eff}}\Big)\Big(\frac{L_s^2}{3} - \frac{(L_c+L_s)L_s}{2} + L_s L_c\Big) + h_i\big(\frac{L_s}{2} - L_c\big)\Big]\Big]$ $+\rho g \Big[(L_s + L_{eff}) \Big[\Big(\frac{h_o-h_i}{L_{eff}}\Big)\Big(\frac{(L_s+L_{eff})^2}{3} - \frac{(L_c+L_s)(L_s+L_{eff})}{2}$ $+L_s L_c) + h_i\Big(\frac{(L_s+L_{eff})}{2} - L_c\Big)\Big]$ $- L_c \Big[\Big(\frac{h_o-h_i}{L_{eff}}\Big)\Big(\frac{L_c^2}{3} - \frac{(L_c+L_s)L_c}{2} + L_s L_c\Big) + h_i\big(\frac{L_c}{2} - L_c\big)\Big]\Big]$

Table A.1: System of equations used to solve for the tilt of two particles self-assembling in close proximity

Appendix B

Supplemental Information for the Demonstration the Pattern Recognition Algorithm

B.1 Relevant Parameters Used in the Pattern Recognition Algorithm

Table B.1: Parameters for the pattern recognition of the background image.

Parameter	Value	Description
T_{MIN}	0.23	Global minimum intensity threshold
R_{guess} (px)	[104.5, 105, 105.5, 109, 113, 114, 115, 128]	Range of radius guesses used in the Hough circle detection algorithm
T_σ	4.1	Local standard deviation threshold used for binarization
w (px)	3	Local thresholding window size
w_r (px)	[4, 7]	Ring removal window size
$d_{o,coding}$ (px)	[8, 5]	Coding dot circle removal outer region radius
$d_{i,coding}$ (px)	[5, 3]	Coding dot circle removal inner region radius
$d_{o,alignment}$ (px)	14	Alignment dot circle removal outer region radius
$d_{i,alignment}$ (px)	10	Alignment dot circle removal inner region radius
d_a (px)	25	Distance between center of alignment dot 1 to the left edge of the array
n_R	5	Number of coding dot rows in the array
n_C	5	Number of coding dot columns in the array
$paddingX$ (px)	15	Padding between the alignment dot and coding array in X direction
$paddingY$ (px)	15	Padding between the alignment dot and coding array in Y direction
skewtol(°)	2	Coding array skew correction tolerance

Table B.2: Parameters for the pattern recognition of the target image.

Parameter	Value	Description
T_{MIN}	0.307	Global minimum intensity threshold
R_{guess} (px)	[90, 91, 92, 93, 94, 95, 96, 97, 104, 105, 106, 107, 110, 111,] 112, 125]	Range of radius guesses used in the Hough circle detection algorithm
T_{Hist}	13	Histogram count threshold before a location is recognized as a center
T_{σ}	4.65	Local standard deviation threshold used for binarization
w (px)	3	Local thresholding window size
w_r (px)	5	Ring removal window size
$d_{o,coding}$ (px)	[8, 5]	Coding dot circle removal outer region radius
$d_{i,coding}$ (px)	[5, 2]	Coding dot circle removal inner region radius
$d_{o,alignment}$ (px)	13	Alignment dot circle removal outer region radius
$d_{i,alignment}$ (px)	11	Alignment dot circle removal inner region radius
d_a (px)	25	Distance between center of alignment dot 1 to the left edge of the array
n_R	5	Number of coding dot rows in the array
n_C	5	Number of coding dot columns in the array
$paddingX$ (px)	15	Padding between the alignment dot and coding array in X direction
$paddingY$ (px)	15	Padding between the alignment dot and coding array in Y direction
skewtol(°)	2	Coding array skew correction tolerance

B.2 Reports Generated from the Pattern Recognition Runs

The reports generated from the pattern recognition runs of the background and target images are summarized in the following tables.

Table B.3: Output report from the pattern recognition of the background image.

Obj.	Sensor Inver-ted	Rot. Ang. (°)	Skew Ang. (°)	Coding Dot Code	Pattern	Correct ID
1	Yes	231	-2.0	1000111011101011010110001	M	Yes
2	Yes	91	-2.0	1000110001100010101000100	V	Yes
3	No	-141	-2.0	1000101010001000101010001	X	Yes
4	No	169	-0.6	1000111011101011010110001	M	Yes
5	Yes	308	-2.0	1111100010001000100011111	Z	Yes
6	No	31	1.3	1111010001111101000010000	P	Yes
7	No	15	-2.0	1000110001010100010001000	NA	Yes
8	Yes	46	1.1	1111010001111101001010001	R	Yes
9	Yes	162	-0.6	1111010001111101000010000	P	Yes
10	No	-104	-1.1	1111100100001000010011111	I	Yes
11	Yes	48	1.1	1000110101101011101110001	W	Yes
12	No	97	-2.0	1000110010111001001010001	K	Yes
13	Yes	56	-2.0	1000110001100011000101110	U	Yes
14	Yes	142	-2.0	1111100100101000010011111	NA	No
15	Yes	149	-1.2	1000110001100011000101110	U	Yes
16	Yes	138	-2.0	1111100100001000010011111	I	Yes
17	Yes	138	0.0	0000000000000000000000000	NAD	No
18	Yes	253	-0.6	1000110101101011101110001	W	Yes
19	No	124	-2.0	1000110001100010101000100	V	Yes
20	Yes	92	1.4	1000111001101011001110001	N	Yes
21	No	148	-2.0	1000010000100001000011111	L	Yes
22	Yes	215	-1.3	1000101010001000101010001	X	Yes
23	No	84	-2.0	1000111011101011010110001	M	Yes
24	Yes	118	-1.2	1000110001100010101000100	V	Yes

Continued on next page

Obj.	Sensor Inverted	Rot. Ang. $(^{o})$	Skew Ang. $(^{o})$	Coding Dot Code	Pattern	Correct ID
25	Yes	305	-2.0	1000110001100011000101110	U	Yes
26	Yes	310	1.6	1000010000100001000011111	L	Yes
27	Yes	45	-1.4	1000110001100010101000100	V	Yes
28	Yes	132	1.2	1111010001111101001010001	R	Yes
29	Yes	139	1.8	1111010001111101000010000	P	Yes
30	No	-6	-1.7	1000110001111111000110001	H	Yes
31	Yes	197	-0.6	1111100010001000100011111	Z	Yes
32	No	-123	-1.1	1000110001010100010000100	Y	Yes
33	Yes	92	-1.9	1000010000100001000011111	L	Yes
34	No	48	-1.9	1000010000100001000011111	L	Yes
35	No	21	1.1	1111010001111101001010001	R	Yes
36	No	-90	-1.1	1000110001010100010000100	Y	Yes
37	No	-164	-0.6	1000110001111111000110001	H	Yes
38	No	-110	-0.6	1111100010001000100011111	Z	Yes
39	Yes	223	-1.2	1000110001100011000101110	U	Yes
40	Yes	209	-0.6	1111100010001000100011111	Z	Yes
41	No	-115	-0.6	1111100100001000010011111	I	Yes
42	No	146	-2.0	1000110001100010101000100	V	Yes
43	No	-62	-2.0	1000111011101011010110001	M	Yes
44	No	150	-0.6	1000110001111111000110001	H	Yes
45	No	92	-0.6	1000111011101011010110001	M	Yes
46	No	166	-2.0	1000110001100011000101110	U	Yes
47	No	0	0.0	0000000000000000000000000	NAA	No
48	Yes	36	1.1	1000110001111111000110001	H	Yes
49	No	-160	-1.9	1000111001101011001110001	N	Yes
50	Yes	298	-2.0	1000101010001000101010001	X	Yes
51	Yes	350	0.7	1000111001101011001110001	N	Yes
52	Yes	210	-0.7	1000110010111001001010001	K	Yes
53	No	30	-2.0	1111010001111101001010001	R	Yes
54	No	-1	0.7	1000110010111001001010001	K	Yes
55	Yes	263	-2.0	1000110001010100010000100	Y	Yes
56	Yes	120	-1.3	1111100100001000010011111	I	Yes
57	Yes	20	0.6	1000110001111111000110001	H	Yes

Table B.4: Output report from the pattern recognition of the target image.

Obj.	Sensor Inverted	Rot. Ang. $(^o)$	Skew Ang. $(^o)$	Coding Dot Code	Pattern	Correct ID
1	No	32	-1.1	1111010001111101000010000	P	Yes
2	Yes	160	-2.0	1111010001111101000010000	P	Yes
3	No	148	-2.0	1000010000100001000011111	L	Yes
4	Yes	312	-0.6	1000010000100001000011111	L	Yes
5	Yes	140	-1.3	1111010001111101000010000	P	Yes
6	No	-10	1.8	1000110001111111000110001	H	Yes
7	Yes	94	-2.0	1000010000100001000011111	L	Yes
8	No	48	-2.0	1000010000100001000011111	L	Yes
9	No	-164	-0.6	1000110001111111000110001	H	Yes
10	No	150	-1.2	1000110001111111000110001	H	Yes
11	Yes	38	-0.6	1001111001111111000110001	NA	No
12	Yes	16	0.7	1000110001111111000110001	H	Yes

Error codes:

‘NA’ - dot sequence does not match any listing in the key

‘NAD’ - no coding dots found

‘NAA’ - not enough alignment dots found

Appendix C

Supplemental Information for the Complete MUFFINS Platform Demonstration

C.1 Relevant Parameters Used in the Pattern Recognition Algorithm for the Complete MUFFINS Platform Demonstration

The relevant parameters used in the pattern recognition of the background and target images are listed in the following table.

Table C.1: Parameters for the pattern recognition of the background and target image (please consult Section 9.4 or Reference [52] for descriptions of each parameter).

Parameter	Background Image			Target Image		
	TGT REF	TGT 4	TGT 9	TGT REF	TGT 4	TGT 9
T_{MIN}	0.10	0.13	0.09	0.12	0.14	0.18
R_{guess} (px)	[130, 131, 132, 133]	[132, 133, 134, 135]	[133]	[129, 130]	[130, 131]	[130, 131, 132]
T_{Hist}	8	6	3	5	5	8
T_{fill}	0.89	0.89	0.89	0.85	0.80	0.75
T_σ	25	75	75	25	75	75
w (px)	3	3	3	3	3	3
w_r (px)	[4, 7]	[4, 7]	[4, 7]	[4, 7]	[4, 7]	[4, 7]
$d_{o,coding}$ (px)	[8, 5]	[8, 5]	[8, 5]	[8, 5]	[8, 5]	[8, 5]
$d_{i,coding}$ (px)	[5, 3]	[5, 3]	[5, 3]	[5, 3]	[5, 3]	[5, 3]
$d_{o,alignment}$ (px)	12	12	12	12	12	12
$d_{i,alignment}$ (px)	9	9	9	9	9	9
d_a (px)	25	25	25	25	25	25
n_R	5	5	5	5	5	5
n_C	5	5	5	5	5	5
$paddingX$ (px)	15	15	15	15	15	15
$paddingY$ (px)	15	15	15	15	15	15
skewtol(°)	2	2	2	2	2	2

C.2 Modifications to the pattern recognition algorithm

Please refer to previous work by Meiring et al [52] for complete description of the pattern recognition algorithm. This section is intended to describe only the modifications made to the recognition algorithm. Specifically, the global minimum thresholding step, which was used in the preprocessing step and prior to the standard deviation filtering step, was switched off prior to the standard deviation filtering and a “fill percent threshold” (T_{fill}) check was added to the circle detection module. This modification was necessary because the signal captured from the array was not as intense and uniformly distributed as the sensors used with the previous work. The use of the global minimum thresholding would often incorrectly remove pixels within the ‘bright’ portions of the sensor. However, the global minimum thresholding was still used in the preprocessing step prior to the circle detection. The fill percent threshold check aided in the detection of individual circular sensors in the circle detection step. The algorithm compared the ‘filling’ of a potential circle candidate, defined as the ratio of the number of pixels in the circle with nonzero intensity to the total number of pixels in the circle, to a preset threshold. If the fill ratio is less than the threshold, the point is excluded from consideration as a possible center point.

Bibliography

[1] A. Akkoyun and U. Bilitewski. Optimisation of glass surfaces for optical immunosensors. *Biosensors and Bioelectronics*, 17(8):655–664, 2002.

[2] D. H. Ballard. Generalizing the hough transform to detect arbitrary shapes. *Pattern Recognition*, 13(2):111–122, 1981.

[3] Ralph Sherman Becker and Josef Michl. Photochromism of synthetic and naturally occurring 2H-chromenes and 2H-pyrans. *Journal of the American Chemical Society*, 88(24):5931–3, 1966.

[4] Adam J. Berro, Xinyu Gu, Naphtali O'Connor, Steffen Jockusch, Tomoki Nagai, Toshiyuki Ogata, Paul Zimmerman, Bryan J. Rice, Elizabeth Adolph, Travis Byargeon, Jose Gonzalez, Nicholas J. Turro, and C. Grant Willson. Optical threshold layer and intermediate state two-photon pag approaches to double exposure lithography. In *Advances in Resist Materials and Processing Technology XXVI*, volume 7273, pages 72731B–10, San Jose, CA, USA, 2009. SPIE.

[5] Roger T. Bonnecaze. Lecture notes from CHE 385M Surface Phenomena. Unpublished lecture notes, 2005.

[6] Ned Bowden, Insung S. Choi, Bartosz A. Grzybowski, and George M. Whitesides. Mesoscale self-assembly of hexagonal plates using lateral

capillary forces: Synthesis using the “capillary bond”. *Journal of the American Chemical Society*, 121(23):5373–5391, 1999.

[7] John H. Bruning. Optical lithography: 40 years and holding. In *Optical Microlithography XX*, volume 6520, pages 652004–13, San Jose, CA, USA, 2007. SPIE.

[8] Jeffrey Byers, Saul Lee, Kane Jen, Paul Zimmerman, Nicholas J. Turro, and C. Grant Willson. Double exposure materials: Simulation study of feasibility. *Journal of Photopolymer Science and Technology*, 20(5):707–717, 2007.

[9] Andrew Carmen and Gary Hardiman, editors. *Biochips as pathways to drug discovery.* CRC Press, Boca Raton, 2007.

[10] Glenn H. Chapman, Yuqiang Tu, and Jun Peng. Wavelength invariant Bi/In thermal resist as a Si anisotropic etch masking layer and direct-write photomask material. In *Advances in Resist Technology and Processing XX*, volume 5039, pages 472–483, Santa Clara, CA, USA, 2003. SPIE.

[11] Steven C. Chapra and Raymond P. Canale. *Numerical Methods For Engineers: With Software and Programming.* McGraw-Hill, New York, 4th edition, 2002.

[12] Michael Dickey. Graduate research work on self-assembly of muffins. Unpublished research work, 2003.

[13] Thomas Edison. Electrical indicator. US Patent 307031, 1884.

[14] Jason R. Epstein, Amy P. K. Leung, Kyong-Hoon Lee, and David R. Walt. High-density, microsphere-based fiber optic DNA microarrays. *Biosensors and Bioelectronics*, 18(5-6):541–546, 2003.

[15] Erin F. Fleet, Serpil Gonen, Gregory D. Cooper, and Zhiyun Chen. Programmable photolithographic mask and reversible photo-bleachable materials based on nano-sized semiconductor particles and their applications. *PCT Int Appl. WO2004053938.*, 2004.

[16] Stephen P. A. Fodor, J. Leighton Read, Michael C. Pirrung, Lubert Stryer, Amy Tsai Lu, and Dennis Solas. Light-directed, spatially addressable parallel chemical synthesis. *Science*, 251(4995):767–773, 1991.

[17] International Technology Roadmap for Semiconductors. ITRS report, 2007 edition, lithography module. Website, Accessed 01/07/2009. `http://www.itrs.net/Links/2007ITRS/2007_Chapters/2007_Lithography.pdf`.

[18] Jean M. J. Frechet, Hiroshi Ito, and C. Grant Willson. Sensitive Deep UV resist incorporating chemical amplification. In *Proceedings of Microcircuit Engineering*, page 260, Grenoble, 1982.

[19] Andrew Gehring, David Albin, Sue Reed, Shu-I. Tu, and Jeffrey Brewster. An antibody microarray, in multiwell plate format, for multiplex screening of foodborne pathogenic bacteria and biomolecules. *Analytical and Bioanalytical Chemistry*, 391(2):497–506, 2008.

[20] Dan Gelbart and Valentin A. Karasyuk. UV thermoresists: sub-100-nm imaging without proximity effects. *Proceedings of SPIE-The International Society for Optical Engineering*, 3676(Pt. 2, Emerging Lithographic Technologies III):786–793, 1999.

[21] B. D. Grant, N. J. Clecak, R. J. Twieg, and C. G. Willson. Deep UV photoresists I. Meldrum's diazo sensitizer. *Electron Devices, IEEE Transactions on*, 28(11):1300–1305, 1981.

[22] Scott M. Grayson, Matthew J. Schmid, Jason E. Meiring, Vijay Desai, Daniel U, Kalpana Manthiram, Andrew D. Ellington, and C. Grant Willson. The self-assembly of hydrogel sensors into a functional array. *Polym. Prepr. (Am. Chem. Soc., Div. Polym. Chem.)*, 45(2):432–433, 2004.

[23] Bruce F. Griffing and Paul R. West. Contrast enhanced lithography. *Solid State Technology*, 28(5):152–7, 1985.

[24] Xinyu Gu, Adam J. Berro, Younjin Cho, Kane Jen, Saul Lee, Tomoki Ngai, Toshiyuki Ogata, William J. Durand, Arunkumar Sundaresan, Jeffrey R. Lancaster, Steffen Jockusch, Paul Zimmerman, Nicholas J. Turro, and C. G. Willson. Fundamental study of optical threshold layer approach towards double exposure lithography. In *Advances in Resist Materials and Processing Technology XXVI*, volume 7273, pages 72731C–11, San Jose, CA, USA, 2009. SPIE.

[25] J. Milton Harris, editor. *Poly(ethylene glycol) chemistry: biotechnical*

and biomedical applications. Topics in applied chemistry. Plenum Press, New York, 1992.

[26] J. Milton Harris and Samuel Zalipsky, editors. *Poly(ethylene glycol) chemistry and biological applications*, volume 680 of *ACS symposium series*. American Chemical Society, Washington, DC, 1997.

[27] P. J. Hergenrother, K. M. Depew, and S. L. Schreiber. Small-molecule microarrays: Covalent attachment and screening of alcohol-containing small molecules on glass slides. *J. Am. Chem. Soc.*, 122(32):7849–7850, 2000.

[28] Kevin A. Heyries, Michael G. Loughran, Daniel Hoffmann, Alexandra Homsy, Loc J. Blum, and Christophe A. Marquette. Microfluidic biochip for chemiluminescent detection of allergen-specific antibodies. *Biosensors and Bioelectronics*, 23(12):1812–1818, 2008.

[29] Cheng-En Ho, Ching-Chang Chieng, Ming-Hung Chen, and Fan-Gang Tseng. Rapid microarray system for passive batch-filling and in-parallel-printing protein solutions. *J. Microelectromech. Syst.*, 17(2):309–317, 2008.

[30] Ku-Lung Hsu, Jeffrey C. Gildersleeve, and Lara K. Mahal. A simple strategy for the creation of a recombinant lectin microarray. *Molecular BioSystems*, 4(6):654–662, 2008.

[31] Illumina.com. technology: beadarray techonology. Website, Accessed 08/04/2009. `http://www.illumina.com/pages.ilmn?ID=5`.

[32] Intel.com. Moores law backgrounder. Website, Accessed 06/02/2009. `http://download.intel.com/museum/Moores_Law/Printed_Materials/Moores_Law_Backgrounder.pdf`.

[33] Hiroshi Ito. Chemical amplification resists for microlithography. In *Microlithography*, pages 37–245. 2005. 10.1007/b97574.

[34] Hiroshi Ito and C. Grant Willson. Chemical amplification in the design of dry developing resist materials. *Polymer Engineering and Science*, 23(18):1012–1018, 1983.

[35] Hiroshi Ito, C. Grant Willson, and Jean M. J. Frechet. New UV resists with negative or positive tone. In *VLSI Technology, 1982. Digest of Technical Papers. Symposium on*, pages 86–87, 1982.

[36] Takanori Kawakami, Tomoki Nagai, Yukio Nishimura, Motoyuki Shima, Shiro Kusumoto, and Tsutomu Shimokawa. Various factors of the image blur in chemically amplified resist. In *Advances in Resist Materials and Processing Technology XXIV*, volume 6519, pages 65193K–9, San Jose, CA, USA, 2007. SPIE.

[37] Jack Kilby. Miniaturized electronic circuits. *Texas Instruments*, US Patent 3,138,743, 1964.

[38] Won-Gun Koh, Laura J. Itle, and Michael V. Pishko. Molding of hydrogel microstructures to create multiphenotype cell microarrays. *Analytical Chemistry*, 75(21):5783–5789, 2003.

[39] P. A. Kralchevsky, V. N. Paunov, N. D. Denkov, I. B. Ivanov, and K. Nagayama. Energetical and force approaches to the capillary interactions between particles attached to a liquid-fluid interface. *Journal of Colloid and Interface Science*, 155(2):420–37, 1993.

[40] Peter A. Kralchevsky and Kuniaki Nagayama. Capillary forces between colloidal particles. *Langmuir*, 10(1):23–36, 1994.

[41] M. M. Krayushkin, B. M. Uzhinov, A. Yu Martynkin, D. L. Dzhavadov, M. A. Kalik, V. L. Ivanov, F. M. Stoyanovich, L. D. Uzhinova, and O. Yu Zolotarskaya. Thermally irreversible photochromic dithienylethenes. *International Journal of Photoenergy*, 1(3):183–190, 1999.

[42] Stephen M. Kuebler, Kevin L. Braun, Wenhui Zhou, J. Kevin Cammack, Tianyue Yu, Christopher K. Ober, Seth R. Marder, and Joseph W. Perry. Design and application of high-sensitivity two-photon initiators for three-dimensional microfabrication. *Journal of Photochemistry and Photobiology A: Chemistry*, 158(2-3):163–170, 2003.

[43] C. N. LaFratta and D. R. Walt. Very high density sensing arrays. *Chem. Rev.*, 108(2):614–637, 2008.

[44] Banafshe Larijani, Rudiger Woscholski, and Colin A. Rosser. *Chemical biology : applications and techniques*. John Wiley & Sons, Chichester, England, 2006.

[45] Saul Lee, Peter Carmichael, Jason Meiring, Michael Dickey, Scott Grayson, Roger T. Bonnecaze, and C. Grant Willson. Modeling of self-assembly dynamics of photolithographically patterned muffins biosensor arrays, in printing methods for electronics, photonics, and biomaterials, edited by jay guo. In *Mater. Res. Soc. Symp. Proc.*, volume 1002E, 2007.

[46] Saul Lee, Kane Jen, C. Grant Willson, Jeffrey Byers, Paul Zimmerman, and Nicholas J. Turro. Materials modeling and development for use in double-exposure lithography applications. *Journal of Micro/Nanolithography, MEMS and MOEMS*, 8(1):011011–11, 2009.

[47] Biaoyang Lin, Jun Wang, and Yin Cheng. Recent patents and advances in the next-generation sequencing technologies. *Recent Pat. Biomed. Eng.*, 1(1):60–67, 2008.

[48] G. MacBeath, A. N. Koehler, and S. L. Schreiber. Printing small molecules as microarrays and detecting protein-ligand interactions en masse. *J. Am. Chem. Soc.*, 121(34):7967–7968, 1999.

[49] Gavin MacBeath and Stuart L. Schreiber. Printing proteins as microarrays for high-throughput function determination. *Science*, 289(5485):1760, 2000.

[50] David Manners and Tsugio Makimoto. *Living with the Chip.* Chapman and Hall, London, 1st edition, 1995.

[51] Jason E. Meiring. *Mesoscale Simulation of the Photoresist Process and Hydrogel Biosensor Array Platform Indexed by Shape.* PhD thesis, The University of Texas at Austin, 2005.

[52] Jason E. Meiring, Saul Lee, Elizabeth A. Costner, Matthew J. Schmid, Timothy B. Michaelson, C. Grant Willson, and Scott M. Grayson. Pattern recognition of shape-encoded hydrogel biosensor arrays. *Optical Engineering*, 48(3):037201–14, 2009.

[53] Jason E. Meiring, Matthew J. Schmid, Scott M. Grayson, Benjamen M. Rathsack, David M. Johnson, Romy Kirby, Ramakrishnan Kannappan, Kalpana Manthiram, Jennifer Stotts, Zachary L. Hogan, Ryan J. Russel, Michael V. Pishko, Andrew D. Ellington, and C. Grant Willson. Hydrogel biosensor arrays indexed through shape recognition. *PMSE Preprints*, 89:217–218, 2003.

[54] Jason E. Meiring, Matthew J. Schmid, Scott M. Grayson, Benjamin M. Rathsack, David M. Johnson, Romy Kirby, Ramakrishnan Kannappan, Kalpana Manthiram, Benjamin Hsia, Zachary L. Hogan, Andrew D. Ellington, Michael V. Pishko, and C. Grant Willson. Hydrogel biosensor array platform indexed by shape. *Chemistry of Materials*, 16(26):5574–5580, 2004.

[55] G. E. Moore. Progress in digital integrated electronics. In *Electron Devices Meeting, 1975 International*, volume 21, pages 11–13, 1975.

[56] Gordon Moore. Cramming more components onto integrated circuits. *Electronics*, 38(8), 1965.

[57] Robert Noyce. Semiconductor device-and-lead structure. *Fairchild Semiconductor Corporation*, US Patent 2,981,877, 1961.

[58] Naphtali A. O'Connor, Adam J. Berro, Jeffrey R. Lancaster, Xinyu Gu, Steffen Jockusch, Tomoki Nagai, Toshiyuki Ogata, Saul Lee, Paul Zimmerman, C. Grant Willson, and Nicholas J. Turro. Toward the design of a sequential two photon photoacid generator for double exposure photolithography. *Chemistry of Materials*, 20(24):7374–7376, 2008.

[59] K. A. O'Leary and D. R. Paul. Physical properties of poly(n-alkyl acrylate) copolymers. part 1. crystalline/crystalline combinations. *Polymer*, 47(4):1226–1244, 2006.

[60] K. A. O'Leary and D. R. Paul. Physical properties of poly(n-alkyl acrylate) copolymers. part 2. crystalline/non-crystalline combinations. *Polymer*, 47(4):1245–1258, 2006.

[61] James R. Parker. *Algorithms for image processing and computer vision.* John Wiley & Sons, Inc., 1997.

[62] Adam R. Pawloski, Glenn McGall, Robert G. Kuimelis, Dale Barone, Andrea Cuppoletti, Paul Ciccolella, Eric Spence, Farhana Afroz, Paul Bury, Christy Chen, Chuan Chen, Dexter Pao, Mary Le, Becky McGee, Elizabeth Harkins, Michael Savage, Sim Narasimhan, Martin Goldberg,

Richard Rava, and Stephen P. A. Fodor. Photolithographic synthesis of high-density DNA probe arrays: Challenges and opportunities. volume 25, pages 2537–2546. AVS, 2007.

[63] A. C. Pease, D. Solas, E. J. Sullivan, M. T. Cronin, C. P. Holmes, and S. P. Fodor. Light-generated oligonucleotide arrays for rapid DNA sequence analysis. *Proc. Natl. Acad. Sci.*, 91:5022–5026, 1994.

[64] Daniel C. Pregibon, Mehmet Toner, and Patrick S. Doyle. Multifunctional encoded particles for high-throughput biomolecule analysis. *Science*, 315(5817):1393–1396, 2007.

[65] Benjamin M. Rathsack. *Photoresist modeling for 365 nm and 257 nm laser photomask lithography and multi-analyte biosensors indexed through shape recognition.* PhD thesis, The University of Texas at Austin, 2001.

[66] J. Sauvola and M. Pietikainen. Adaptive document image binarization. *Pattern Recognition*, 33(2):225–236, 2000.

[67] M. Schena, D. Shalon, R. W. Davis, and P. O. Brown. Quantitative monitoring of gene expression patterns with a complementary DNA microarray. *Science*, 270(5235):467–470, 1995.

[68] Mark Schena, editor. *Microarray Biochip Technology.* Eaton Publishing, Natick, 2000.

[69] Mark Schena, editor. *DNA Microarrays.* The Methods Express. Scion Publishing, Bloxham, 2008.

[70] Matthew J. Schmid. *Multi-Analyte Biosensing The Integration of Sensing Elements into a Photolithographically Constructed Hydrogel Based Biosensor Platform.* PhD thesis, The University of Texas at Austin, 2005.

[71] Matthew J. Schmid, Kalpana Manthiram, Scott M. Grayson, James C. Willson, Jason E. Meiring, Kathryn M. Bell, Andrew D. Ellington, and C. Grant Willson. Feature multiplexing-improving the efficiency of microarray devices. *Angewandte Chemie, International Edition*, 45(20):3338–3341, 2006.

[72] Matthew J. Schmid, Jason E. Meiring, Romy Kirby, Kalpana Manthiram, Scott Grayson, Andrew D. Ellington, and C. Grant Willson. Functionalizing hydrogel based biosensors with DNA oligomers for single nucleotide polymorphism detection. *PMSE Preprints*, 89:215–216, 2003.

[73] William Shockley. Circuit element utilizing semiconductor materials. *Bell Telephone Laboratories*, US Patent 2,569,347, 1951.

[74] Ronald G Sosnowski, Eugene Tu, William F Butler, James P O'Connell, and Michael J Heller. Rapid determination of single base mismatch mutations in DNA hybrids by direct electric field control. *Proc. Natl. Acad. Sci.*, 94(4):1119–1123, 1997.

[75] Ed M. Southern. Blotting at 25. *Trends in Biochemical Sciences*, 25(12):585–588, 2000.

[76] Frank J. Steemers, Jane A. Ferguson, and David R. Walt. Screening unlabeled DNA targets with randomly ordered fiber-optic gene arrays. *Nat Biotech*, 18(1):91–94, 2000.

[77] Larry F. Thompson, C. Grant Willson, and Murrae J. Bowden. *Introduction to microlithography*. American Chemical Society, Washington, DC, 2nd edition, 1994.

[78] Dominic Vella and L. Mahadevan. The "cheerios effect". *American Journal of Physics*, 73(9):817–825, 2005.

[79] Texas Instruments Website. The chip that jack built. *http://www.ti.com/corp/docs/kilbyctr/jackbuilt.shtml*, Accessed February 01, 2009.

[80] Paul R. West, Gary C. Davis, and Bruce F. Griffing. Contrast enhanced photolithography: application of photobleaching processes in microlithography. *Journal of Imaging Science*, 30(2):65–8, 1986.

[81] C. Grant Willson, Ralph R. Dammel, and Arnost Reiser. Photoresist materials: a historical perspective. In *Optical Microlithography X*, volume 3051, pages 28–41, Santa Clara, CA, USA, 1997. SPIE.

[82] Alfred Kwok-Kit Wong. *Resolution enhancement techniques in optical lithography*. The Tutorial Texts. SPIE Press, Bellingham, Washington, 2001.

[83] Vamsi K. Yadavalli, Won-Gun Koh, George J. Lazur, and Michael V. Pishko. Microfabricated protein-containing poly(ethylene glycol) hydro-

gel arrays for biosensing. *Sensors and Actuators B: Chemical*, 97(2-3):290–297, 2004.

[84] S. Zheng, A. Leclercq, J. Fu, L. Beverina, L. A. Padilha, E. Zojer, K. Schmidt, S. Barlow, J. Luo, S. H. Jiang, A. K. Y. Jen, Y. Yi, Z. Shuai, E. W. VanStryland, D. J. Hagan, J. L. Bredas, and S. R. Marder. Two-photon absorption in quadrupolar bis(acceptor)-terminated chromophores with electron-rich bis(heterocycle)vinylene bridges. *Chem. Mater.*, 19(3):432–442, 2007.

Index

Vita

Shao-Chien (Saul) Lee was born in Taipei, Taiwan to Jan and Oliver Lee. His upbringing was a combination of the East, the West, and the Mid-East, spending time in Taiwan, southwest Georgia, and Saudi Arabia. Saul graduated from Americus High School in Americus, Georgia in 1999. He enrolled at the Georgia Institute of Technology and received a Bachelor of Science degree in Chemical Engineering with Highest Honors in Spring 2004. In the fall of 2004, Saul began graduate studies in the Department of Chemical Engineering at The University of Texas at Austin under the supervision of Professor C. Grant Willson. While at UT, Saul was a recipient of the Engineering Doctoral Fellowship. After the completion of his doctorate in the Summer 2009, Saul will be employed by Molecular Imprints, Inc. in Austin, Texas.

Permanent address: 203 E 31ST ST APT. 102
Austin, Texas 78705

This dissertation was typeset with LaTeX[†] by the author.

[†] LaTeX is a document preparation system developed by Leslie Lamport as a special version of Donald Knuth's TeX Program.